POLITECNICO DI MILANO

Scuola di Ingegneria dei Processi Industriali

Corso di Laurea Magistrale in Ingegneria Chimica

Dipartimento di Chimica, Materiali e Ingegneria Chimica “G. Natta”

EXPERIMENTAL AND MODELING STUDY OF SOOT FORMATION IN LAMINAR PREMIXED FLAMES

Relatore: Prof. Tiziano Faravelli

Correlatori: Prof. Alessandro Gomez (Yale University)
Chiara Saggese
Prof. Alessio Frassoldati
Prof. Alberto Cuoci

Tesi di Laurea Magistrale in Ingegneria Chimica di:

Sara FERRARIO matr. 783294

A.A. 2013-2014

Index

List of figures

List of tables

Abstract

Gli idrocarburi policiclici aromatici e il particolato carbonioso sono emessi nell'ambiente primariamente da processi di combustione e contribuiscono significativamente all'inquinamento atmosferico causando problemi di salute. Inoltre riducono l'efficienza di combustione in molti dispositivi.

Una conoscenza più approfondita dei meccanismi alla base della loro formazione permetterebbe miglioramenti nel design dei sistemi di combustione, incrementando l'efficienza energetica e diminuendo le emissioni di particolato.

L'obiettivo di questo lavoro è di contribuire ad un miglioramento nella comprensione della formazione del soot attraverso un ulteriore sviluppo del modello cinetico nato nel dipartimento CMIC del Politecnico di Milano e un'attività sperimentale svolta nel centro di combustione dell'università di Yale per validare una tecnica di campionamento del soot per sistemi ad alta pressione su una fiamma premiscelata laminare atmosferica.

L'attività di modellazione è principalmente focalizzata su fiamme laminari premiscelate ad etilene e in particolare sulla fiamma con piano di ristagno stabilizzata su bruciatore proposta da Wang e collaboratori.

Innanzitutto, si definisce un metodo monodimensionale appropriato per descrivere la configurazione con piano di ristagno tramite un set di equazioni e condizioni al contorno. L'approccio consiste nel simularla come una fiamma a controdiffusione con velocità nulla dal lato ossidante. È molto importante definire correttamente le condizioni al contorno, specialmente quelle riguardanti le specie. In particolare, per le specie gassose, la somma dei termini convettivi e diffusivi è zero dal lato ossidante, mentre per le particelle è uguale al flusso termoforetico. Questo permette di tener conto del flusso di particelle che si depositano sulla superficie raffreddata ad acqua. Delle simulazioni bidimensionali sono svolte per validare l'approccio monodimensionale e i risultati trovati sono totalmente consistenti.

In seguito, la capacità del modello di predire la formazione di soot in condizioni differenti è testata tramite delle simulazioni di un reattore plug flow e il confronto con dati sperimentali da fiamme laminari premiscelate a differenti pressioni, rapporti di equivalenza e composizione. Infine, la fiamma con piano di ristagno è simulata e il modello è in buon accordo con i dati sperimentali.

L'obiettivo dell'attività sperimentale è la convalida dell'utilizzo della tecnica di campionamento termoforetica per fiamme ad alta pressione allo scopo di raccogliere informazioni sul soot. La fiamma diviene sempre più sottile al crescere della pressione, perciò il substrato su cui si effettua il campionamento dev'essere sufficientemente sottile in modo da non causare eccessive perturbazioni e da avere un'alta risoluzione spaziale: dei fili sono scelti a tale scopo.

Tuttavia, le particelle potrebbero continuare a crescere una volta raccolte a causa di interazioni con l'ambiente della fiamma.

Per tale motivo l'intera attività sperimentale è volta alla ricerca di un substrato appropriato su cui la distribuzione di particelle osservata dopo il campionamento non sia affetta da fenomeni di ulteriore crescita sul filo.

Substrati di differenti temperature sono testati e i risultati, sebbene preliminari, sembrano mostrare che in entrambi i casi la crescita sia effettivamente presente.

Abstract

Polycyclic aromatic hydrocarbons and soot particles are primarily emitted in the environment from combustion sources and are responsible for environmental pollution, reduction of combustion efficiency in many devices and health issues. A deeper knowledge of the mechanisms underlying their formation would allow for a better design of combustion systems with improved energy efficiency and a simultaneous reduction of particulate emissions.

The objective of this work is to contribute to a better understanding of soot formation through a further development of the kinetic model developed in the CMIC department of Politecnico di Milano and an experimental activity carried out in the combustion center of Yale University to validate a soot sampling technique for high pressure on atmospheric laminar premixed flames.

The modeling activity is mainly focused on ethylene premixed laminar flames, in particular on the simulation of the Burner-Stabilized Stagnation (BSS) flame proposed by Wang and coworkers.

First, a proper one-dimensional method to describe the stagnation-surface configuration is defined through a set of conservation equations and boundary conditions. The approach consists in simulating it as a counterflow flame with zero velocity on the oxidizer side. It is very important to define correctly the boundary conditions, especially those for the species. In particular, for gaseous species, the sum of the convective and diffusive terms is zero on the air side, while for particles it is equal to the thermophoretic flux. This allows to take into account the flux of soot particles depositing on the water-cooled surface. Two-dimensional simulations are carried out to validate the one-dimensional approach and the results are totally consistent.

Afterwards, the model capability to predict soot formation under different conditions is tested with plug flow reactor simulations and comparisons with experimental data from laminar premixed flames at different pressures, equivalence ratios and composition. Finally, the BSS flame is simulated and a good agreement between experimental data and the model is found.

The goal of the experimental activity is to validate the use of the thermophoretic sampling technique for high pressure to collect information on soot. As the flame gets thinner with increasing pressure, the collecting substrate must be thin enough not to bring excessive perturbations and to have high spatial resolution; therefore thin wires are chosen for this purpose.

However, particles might continue their growth once collected by means of interactions with the flame environment. Therefore, the whole activity aims to find a proper substrate where the particle size distribution that can be observed after collection is not affected by further growth on the wire. Colder and hotter substrates are tested and the results, although preliminary, seem to show that in both cases the growth is actually present.

1 Introduction

Combustion is present in many large-scale processes, including combustion engines, power stations, waste incineration and residential burning of wood and coal.
These, with field burning of agricultural wastes and forest and vegetation fires, are the main sources of airborne species, such as soot and polycyclic aromatic hydrocarbons (PAH), which are not only pollutant, but also of significant health concerns.

Diesel combustion accounts for over one quarter of the total hazardous pollution in air in North America and Europe and 66 percent of particulate pollution is from on-road mobile sources[1].

In this chapter soot effects on environment and health are framed within the more general problems arising from atmospheric pollution. In paragraph 1.1 and 1.2 an overview on the main atmospheric pollutants and aerosols is given to contextualize the study on soot formation in the wider field of aerosols and substances of environmental concern.

Paragraph 1.3 presents a first description of soot morphology in order to understand better what it is and how it can interact with the surroundings, causing health and environmental issues, that are presented in paragraphs 1.4 and 1.5.

1.1 ATMOSPHERIC POLLUTANTS

Generally, all substances changing the natural composition of air from natural or anthropogenic sources are considered pollutants, although not all of them are noxious. One can distinguish between primary and secondary air pollutants. Primary air pollutants are emitted directly into the air from sources, while secondary air pollutants are formed through chemical or physical processes in the atmosphere. Examples of primary pollutants are products of incomplete combustion like carbon monoxide, hydrocarbons, PAHs or soot, (CO_2 is pollutant even if it comes from a complete combustion process) sulfur compounds or nitrogen oxides.

Fossil fuels contain sulfur compounds coming from amino acids that were present when they formed. In general, they accumulate in the heavier fractions during oil refinement because they have substantially higher boiling points than their corresponding pure hydrocarbons and in case of coal their amount increases with the content of volatile components.

When these fossil fuels are burned sulfur oxides (SO_2, SO_3) and hydrogen sulfides (H_2S) are formed. The former products can oxidize to form sulfuric acid (secondary pollutant) and cause acid rains, while the main problem associated to hydrogen sulfides is that they can lead to annoying odors even in the smallest amount[2].

Nitrogen monoxide is formed during combustion processes at high temperature through three mechanisms, depending on the conditions of temperature and concentration, on the residence time and the type of fuel: thermal NO, prompt NO and fuel NO.

In the first two mechanisms the nitrogen is taken from combustion air, while in the third one it comes from the fuel itself.

NO_2 is formed in the exhaust gases and finally in the atmosphere, where there is an adequate oxygen content. Considerable NO_2 emissions must be expected in combustion processes involving high air excess.

In the atmosphere NO_x reacts with volatile organic compounds and carbon monoxide to produce ozone, another noxious secondary air pollutant, through a complicated chain reaction mechanism and it can also be oxidized to nitric acid, which contributes to acid rains[3].

1.2 AEROSOLS

Aerosols are small particles capable of suspending in the atmosphere, produced both by natural processes and human activities. Natural aerosols originate from the condensation of gases, from the action of the wind on the Earth's surface and from volcanic eruptions[4]. Sulfuric acid is an outstanding example of the first mechanism. It is produced by SO_2 (both from volcanoes and fossil fuel combustion) as previously mentioned and it condenses to form aqueous sulfate particles whose composition can be modified by condensation of other gases with low vapor pressure including NH_3, HNO_3 and organic compounds like PAHs and soot, which contribute the most to the creation of these fine particles. Wind can transport desert dust, soil dust or sea salt. An example of how dust is transported all over the globe can be seen in figure 1.1.

Anthropogenic emissions from all the large-scale processes using combustion and mobile sources are the dominant contributors to aerosols near urban and industrial locations.

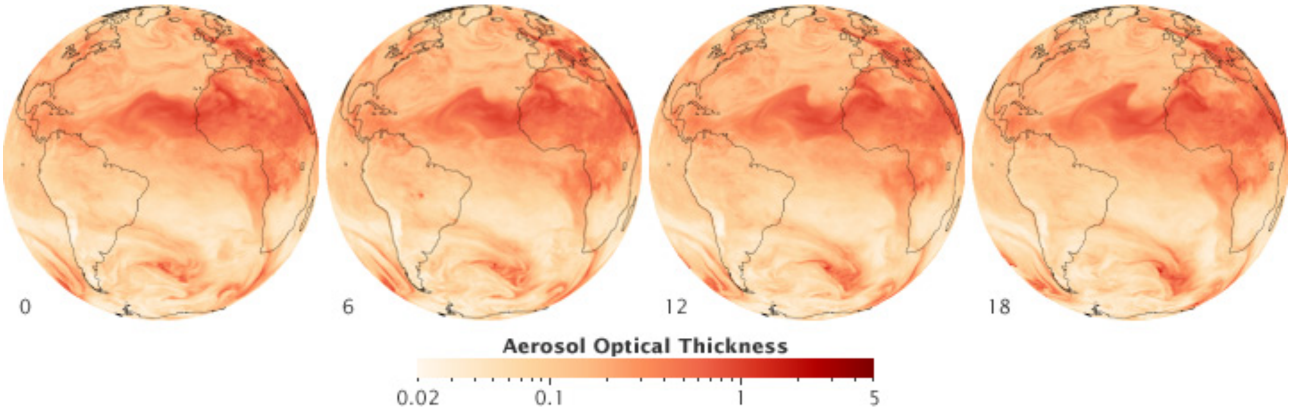

Figure 1.1: Transport of dust from North Africa over the Atlantic Ocean on July 1st, 2009 (from 00.00 to 18.00 Universal Time)[5].

The properties characterizing an aerosol, like mass concentration, number density, composition and dimensions are important to evaluate environmental impact.

Generally the distribution function of atmospheric aerosol dimensions is divided into four ranges that account for different formation mechanisms, as shown below.

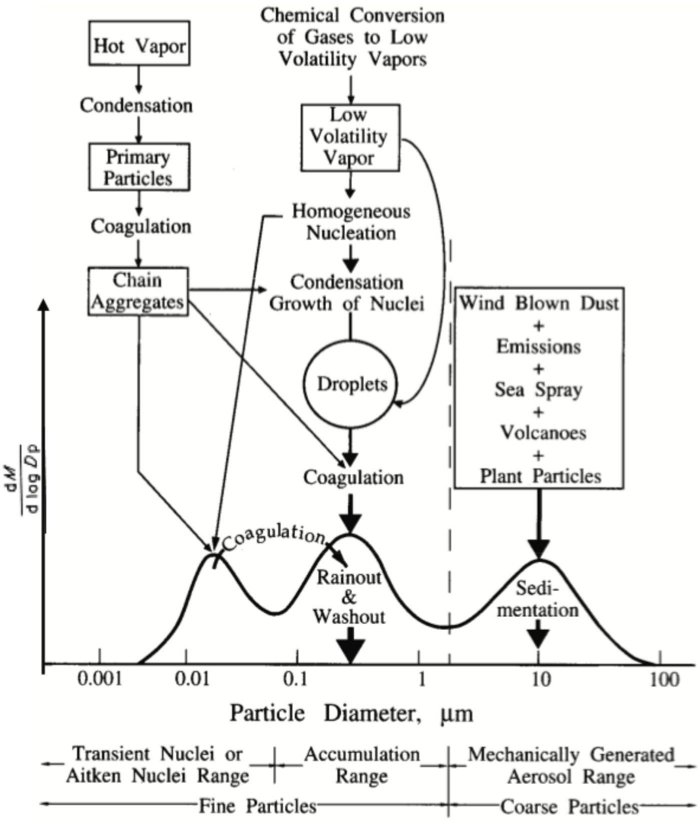

Figure 1.2: Size distribution expressed as mass per increment in log particle diameter and formation mechanisms for atmospheric aerosols[6].

The first range includes diameters between 2 and 100 μm, characteristic of coarse particles from mechanical processes, erosion, sea spray and desert dust. These dimensions facilitate the gravity deposition process and their mobility is due to convective phenomena.

Particles in the second range, defined as the accumulation range, have dimensions between 0.08 and 2 μm. They are originated from coagulation of smaller particles and condensation of volatile compounds that deposit on preexisting particles and they are mainly constituted of organic matter. Their residence time in atmosphere is higher due to lower settling velocities, but they can be washed away by the rain.

Ultrafine particulate (10-80 nm) is in the third range. It comes from nucleation phenomena of supersaturated vapors at low temperature or from combustion processes. Particles in this range are called Aitken nuclei because they act like condensation nuclei, promoting the formation of bigger particles.

The last range includes particles made of organic carbon with diameters below 10 nm. They are also typical of nucleation phenomena.

The convention for dust sampling is to distinguish two main classes: inhalable and respirable particulate. Inhalable particulate is the fraction of a dust cloud that can be breathed into the nose or mouth (PM10, particles with dimensions less than 10 μm), while respirable particulate is the fraction of inhaled airborne particles that can penetrate beyond the terminal bronchioles into the gas-exchange region of the lungs (PM2.5, particles with dimensions less than 2.5 μm)[7].

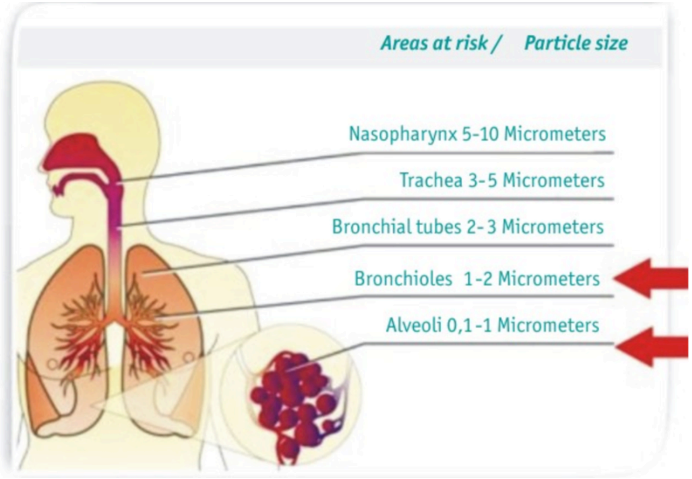

Figure 1.3: Penetration of particles in respiratory system depending on particles' size[8].

1.3 SOOT MORPHOLOGY

The term soot refers to the black particulate formed from the incomplete combustion of organic matter.

In fact, an ideal combustion (perfect mixing of the reactants and stoichiometric composition) produces only CO_2 and H_2O according to the following stoichiometry:

$$C_xH_y + \left(x + \frac{y}{4}\right) O_2 \rightarrow x\,CO_2 + \frac{y}{2}\,H_2O$$

In real devices the burning conditions are often locally non-ideal, because of inadequate mixing of fuel and combustion air, insufficient pulverizing of solid fuels or atomizing of liquid fuels, residence time at high temperatures too short, sudden cooling of the flame gases through combustion chamber walls…

In these portions of the system there is not enough oxygen to transform the fuel in carbon dioxide and water and this results in an incomplete combustion that produces carbon monoxide, hydrogen, PAHs and soot.

Their formation and depletion are kinetically controlled and they cannot be completely oxidized in the lean parts of the system.

Soot formation in industrial systems affects the efficiency of the devices, for example worsening the heat exchange and increasing pressure drops in case of tubular reactors and maintenance is required to prevent its accumulation in the system.

In order to understand better how it affects health and climate it is necessary to consider its morphology, which explains how it can interact with the surrounding environment.

Instead, a review of the possible mechanisms that lead to its formation and that account for this particular morphology will be given later.

Soot is made of roughly spherical particles (called primary particles) with dimensions about 20 nm that afterwards coagulate into fractal aggregates that have a chain-like structure as the one seen in figure 1.4.

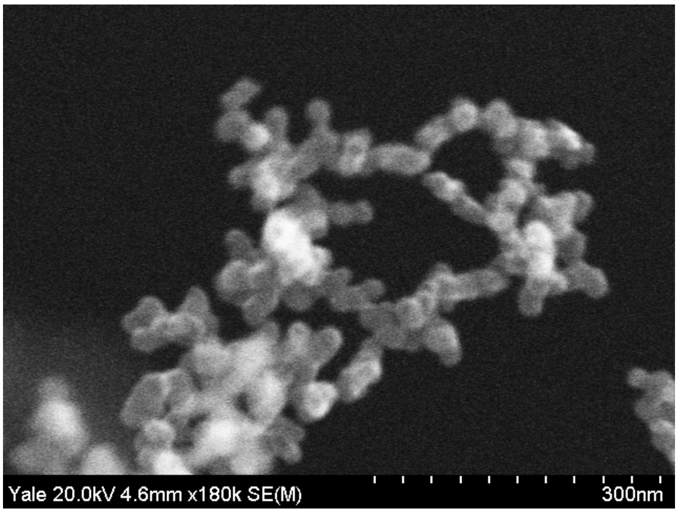

Figure 1.4: SEM picture of aggregated soot particles formed in a premixed ethylene flame.

These primary particles have a soluble fraction constituted mainly of PAHs and their H/C ratio in mature aggregates is about 0.1 or less.

Transmission electron microscope pictures show that they can be amorphous or have a shell-core structure, meaning that is no identifiable long-range order like in graphite but there are graphene layers parallel to the surface in the outer shell and disordered in the core[9,10].

Vander Wal and Tomasek[10] studying soot structure in pyrolysis conditions of different fuels found that at low temperatures (around 1250°C, left panel in figure 1.5) the particles have an amorphous structure, regardless of the fuel, while at high temperatures (around 1650°C, right panel in figure 1.5) a shell-core structure appears and it depends upon the fuel and the flow rate.

High flow rates favor the formation of PAHs with five-membered rings, thus the soot particles have a highly curved nanostructure, while slow flow rates lead to graphitic soot.

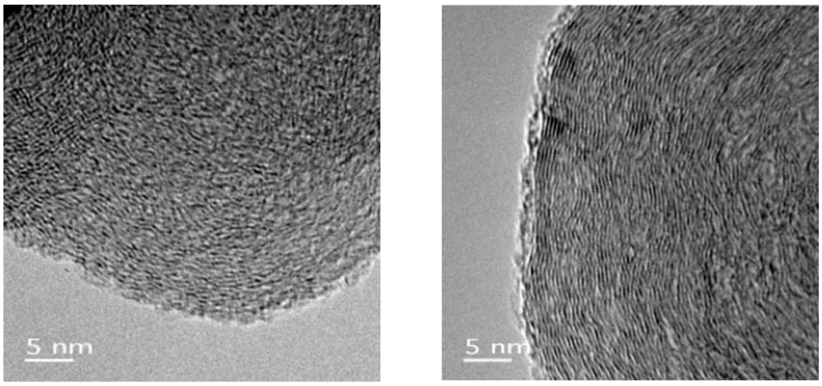

Figure 1.5: Soot formed in low (left) and high (right) temperature pyrolysis of acetylene[10]

Also Alfè et al.[9] confirmed that soot structure is dependent on the fuel and the aging. For example, in benzene flames even in young particles the onion structures are evident (left panel, image g in figure 1.6) whereas in ethylene there is a more amorphous structure. The onion-like structures indicated by the arrow in image g, figure 1.6 for the benzene flame can be interpreted as two smaller particles that coalesced together and that afterwards, due to surface growth, were incorporated into a single spherical particle.

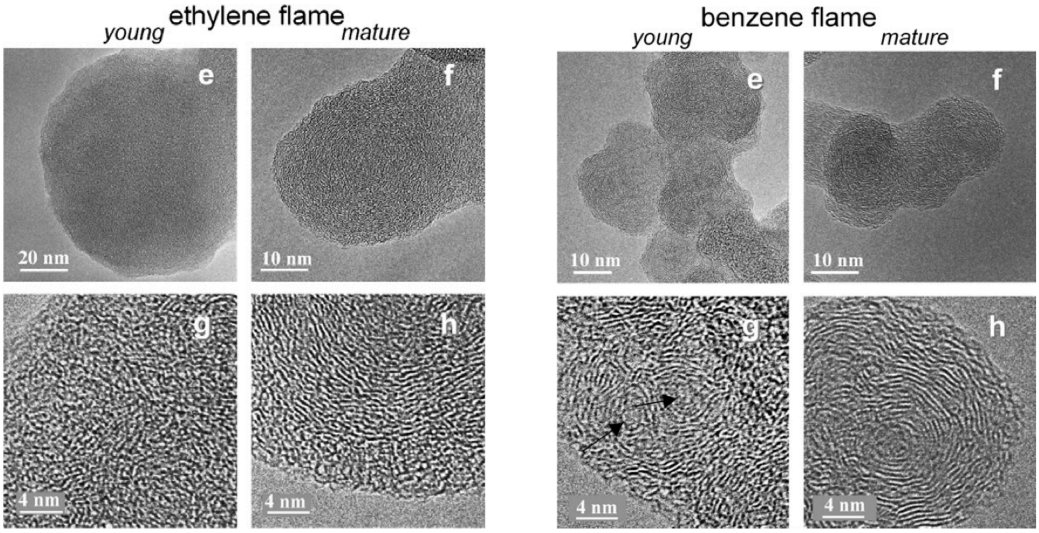

Figure 1.6: Structure of young and mature soot in ethylene and benzene flames[9].

Different structures imply different behaviors toward oxidation, hence different interactions with the surrounding environment.

1.4 HEALTH EFFECTS

Soot carcinogenicity is well known; in fact, in 1775 Percival Pott identified the “Chimney sweep’s cancer”, called “Soot wart”, a squamous cell carcinoma, the first reported form of occupational cancer[11].

Also a new report from the WHO’s (World Health Organization) cancer research agency[12] announced the classification of outdoor air pollution and particulate matter as known human carcinogens, proving the connection between their levels in the air and cancer risks after the International Agency for Research on Cancer (IARC) independently reviewed over 1000 of the latest scientific studies on air pollution.

Lung cancer and cardiopulmonary diseases are long-term effects, but there are also short-term effects including cardiovascular and respiratory diseases.

In fact, soot particles can be as small as 1 nm, hence they can enter the human body and gain access to the blood stream via inhalation or ingestion more easily than larger sized particles and could overload the body's phagocytes, cells that ingest and destroy foreign matter, triggering stress reactions that lead to inflammation.

Once in the blood stream nanoparticles can also be transported around the body and be taken up by organs and tissues where they cumulate in time causing serious damages.

This also shows the importance of regulating not only the ponderal quantity of emitted particles, but also their number since the smaller particles have negligible mass with respect to the bigger ones, but are more toxic by far.

1.5 CLIMATE EFFECTS

As for the pollution, a recent paper published in the Journal of Geophysical Research-Atmospheres[13] classifies black carbon "as the second most important individual climate-warming agent after carbon dioxide, with a total climate forcing of +1.1 W m^{-2} (+0.17 to +2.1 W m^{-2} range)".

It has multiple effects on the environment, as it can be seen in figure 1.7:

- Direct absorption of incoming solar radiation, which causes warming and alters properties of ice clouds and liquid clouds and their distribution
- Deposition on snow and ice increases the light and heat absorption, therefore glacial retreat is enhanced with respect to what it would be considering the mere global warming.

This can lead also to local climate changes and precipitations variations, affecting the delicate biosphere equilibrium and contributing to all the bad effects of global warming.

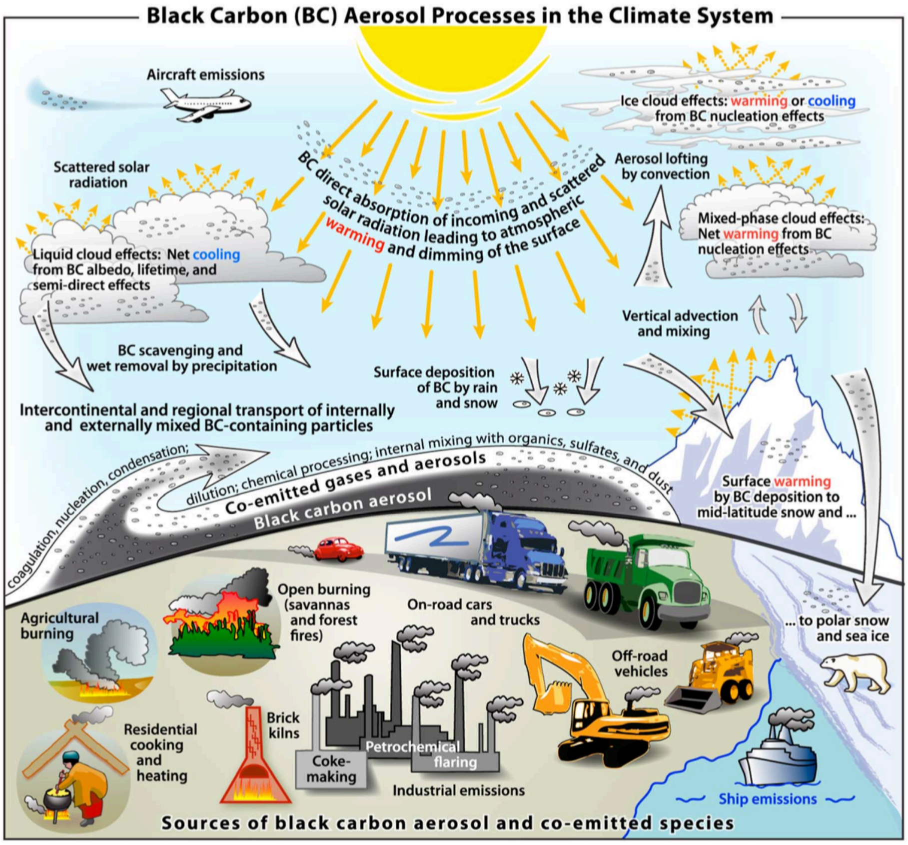

Figure 1.7: Black Carbon aerosol processes in the climate system[13].

From this overview it appears clearly the necessity of controlling soot formation through the understanding of the underlying phenomena. Of course the exhausts from industrial activities are treated before being emitted into the atmosphere, but it is not possible to depurate them completely or to retain even the smallest particles (which are the most dangerous in terms of health as seen before). Furthermore, depuration devices are very expensive and the cost increases with the depuration efficiency.

Hence, a better control on the combustion processes would lead to significant savings, both because it would improve energetic efficiency reducing fuel losses and because the costs for depuration devices would be reduced.

2 Detailed kinetic schemes

Chemical kinetics is the study of rates of chemical processes and it allows to determine the evolution of a system in time.

The kinetic model describing soot formation is associated to a detailed gas-phase kinetic model; hence, before analyzing in detail the kinetic pathways it is necessary to clarify the concept of kinetic model and how it can be developed for the gas phase. Not all the models are detailed: according to the accuracy needed in the kinetics description it can be chosen to use an empirical or a mechanistic model, as explained in paragraph 2.1.
Most of the times the kinetic rate can be expressed as a function of temperature and species' concentrations, as illustrated in paragraph 2.2; sometimes, however, reactions enter a particular regime, the fall-off regime, where the dependence from pressure is not neglectable anymore; on the contrary, it becomes essential to follow the evolution of the species. In paragraph 2.3 the main classes of reactions that might be pressure-dependent are presented, together with the possible ways to express this dependence. Among all the reactions involved in soot formation, metathesis reactions play a fundamental role in promoting the system's reactivity by means of formation of radical species. Paragraph 2.4 is dedicated to the description of the particular approach proposed by Ranzi and coworkers[14] to determine the kinetic parameters for this reaction class. Finally, the peculiar features of the detailed kinetic mechanism of combustion of several hydrocarbons developed in Politecnico di Milano are presented in paragraph 2.5, together with the program used for the simulations in paragraph 2.6.

2.1 GENERAL ASPECTS OF KINETIC MODELS

Kinetic schemes try to represent the dynamics of a system by means of an elevated number of chemical reactions that should describe all the possible pathways that lead from reactants to products.

As the number of species involved grows, the computational cost to model the system increases and it might become too time consuming or unpractical with respect to the initial goal, if a detailed description is not needed.

For this reason, there are two different approaches to model the chemical evolution of a system: the empirical and the mechanistic models.

Empirical models describe the global reactions, include only molecular species and do not consider elementary step. They are "data based", meaning that the parameters in the model are just numbers that encase combined effects, they are not representative of the real physics or chemistry of the system[15]. They are derived from a fitting of the available data, hence they cannot be used to predict the behavior of the system in different conditions.

Nonetheless, they become essential when there is the need of reducing the computational cost like in computational fluid dynamics (CFD) simulations, where the whole flow field has to be described.

Mechanistic models like the one developed in the CMIC department in Politecnico di Milano, instead, are based on the underlying physics and chemistry governing the system. They "should have as many features of the primary system built into it as observations or data will allow[16]", meaning that they try to include all the species involved, both molecular and radical, and most of the reactions are elementary steps. Obviously they have a higher computational cost, but they can be used to predict the behavior of the system outside from the range of collected data or to test the sensitivity of the system.

In this approach there is no mere fitting for the kinetic constants of experimental data, but rather a tuning that might be associated to *ab initio* calculations too.

In fact, kinetic parameters might be determined with quantomechanical *ab initio* calculations, but high level calculations require high computational power, therefore they are possible only for small species. Lower level methods used for larger species have a higher uncertainty. For this reason it is necessary to tune the kinetic parameters and verify the results with experimental data,

but it is deeply different from a simple fitting, because the parameter itself represents a real feature of the system and comes from the joint use of theoretical and experimental information.
It appears clearly that the development of such a model requires an iterative procedure:

- Hypothesis of a mechanism based on current knowledge;
- Simulation and comparison with a wide-range of experimental data;
- Sensitivity and reaction rate analysis to identify the reactions that have a higher impact on the results and the most important pathways that lead to a product;
- Tuning of the kinetic parameters by comparison with experimental data available in literature and analogy with similar reactions.
- New simulation, possibly with new species and new reactions too.

The wide-range validation allows to use a single model for simulations of very different conditions.
Another feature of the mechanistic models is that they apply a lumping to species and reactions.
In fact, for example, long hydrocarbon chains have a high number of isomers that cannot be included in the model without increasing the computational load too much. Furthermore, the additional information that they would bring is not essential to describe the system.
Thus, the lumping procedure allows to account for the behavior of groups of isomers with only one pseudo-species, real or fictitious, and to reduce the number of chemical species and kinetic parameters. Kinetic and thermodynamic properties are obtained from an average of the isomers constituting the lumped compound, thus reducing the computational cost.

2.2 CHEMICAL REACTION RATE

The reaction rate is the rate of creation or depletion of chemical species inside a reacting system.
It is an intensive property, defined locally as a function of temperature, pressure and concentration of the species in the system.
Its dependence from concentration is often non linear and can be very complex, but in case of elementary reaction steps, defined as those reactions where the number and nature of chemical species involved is coincident with the stoichiometry, the reaction rate can be expressed as:

$$r_{fi} = k_i(T,P) \prod_{j=1}^{Reactants\ N°} C_j^{|\nu_{ij}|}$$

Where r_{fi} is the reaction rate of the forward elementary step, k_i is called kinetic constant and contains the dependence from temperature and pressure, C_j the concentration of reacting chemical species and v_{ij} the corresponding stoichiometric coefficients.

Usually the kinetic constant is expressed in the modified Arrhenius form:

$$k_i = A\, T^{\alpha}\, exp\left(-\frac{E_a}{RT}\right)$$

Where A is the pre-exponential factor, T is the absolute temperature, E_a is the activation energy and R is the universal gas constant.

The backward reaction rate can be related to the forward one through the equilibrium constant thanks to the microscopic reversibility.

This equation is called thermodynamic consistency:

$$r_b = f(r_f, K_{eq})$$

$$K_{eq} = {C_{rif}}^{\Delta n}\, exp\left(\frac{\Delta S^0}{R} - \frac{\Delta H^0}{RT}\right)$$

C_{rif} is the reference concentration and Δn the change in number of moles during the reaction.

Thus:

$$k_b = \frac{k_f}{K_{eq}}$$

2.3 PRESSURE-DEPENDENT REACTIONS

The modified Arrhenius expresses the reaction rate dependence from temperature, but there are some classes of reactions like three-body reactions for which it cannot be used, since they have a marked dependence on pressure.

In unimolecular reactions molecules need to acquire sufficient energy to overcome the activation energy and this might happen through collision with a third body that might be every molecule present in the system. Similarly, radical recombination to form one single molecule might need a third body to stabilize the excited product.

Thus reaction rate depends on the total concentration in the system that is, in turn, proportional to the pressure. Above a threshold pressure, however, the reaction rate does not depend anymore on the third body concentration; therefore two asymptotic regions can be defined: in the first one the reaction rate (k_0) depends on the pressure as a third body reaction, in the second (k_∞), above a limit pressure (P_∞), no pressure dependence is considered.

Various expressions are available that blend smoothly between high- and low-pressure limiting rate expressions.

The region where the kinetic constant starts to be affected by pressure is called fall-off regime.

$$k_0 = A_0\, T^{n_0}\, exp\left(-\frac{E_{a0}}{RT}\right)$$

$$k_\infty = A_\infty\, T^{n_\infty}\, exp\left(-\frac{E_{a\infty}}{RT}\right)$$

The rate constant at any pressure is taken to be:

$$k = k_\infty\left(\frac{P_r}{1 + P_r}\right)F$$

Where the reduced pressure P_r is given by:

$$P_r = \frac{k_0[M]}{k_\infty}$$

[M] is the mixture concentration (it might include enhanced third-body efficiencies).

Different forms have been proposed for F, based on different descriptions of the activated complex:

- Lindemann form (1922)[17]

$$F=1$$

- Troe form (1983)

$$logF = \left[1 + \left(\frac{logP_r + c}{m - d(logP_r + c)}\right)^2\right]^{-1} logF_{cent}$$

With

$$c = -0.4 - 0.67\ logF_{cent}$$

$$m = 0.75 - 1.27\ logF_{cent}$$

$$F_{cent} = (1-\alpha)\ exp\left(-\frac{T}{T^{***}}\right) + \alpha\ exp\left(-\frac{T}{T^{*}}\right) + exp\left(-\frac{T^{**}}{T}\right)$$

The parameters α, T^{***}, T^{*} and T^{**} are specific for each reaction.

- SRI form (1989)[18]

$$F = \left[a\ exp\left(-\frac{b}{T}\right) + exp\left(-\frac{T}{c}\right)\right]^X$$

$$X = \frac{1}{1 + log^2 P_r}$$

The parameters a, b and c are specific for each reaction.

2.4 METATHESIS REACTIONS

The H-abstraction reactions play a significant role in gas-phase combustion and accordingly soot formation, hence it is worth to analyze in greater detail how they have been treated in the model. The general form to define metathesis reactions is:

$$R\bullet + R'H \leftrightarrow R'\bullet + RH$$

Where R is a generic hydrocarbon chain and R• is the corresponding radical.

In this approach, it is assumed that the rate constant for the forward reaction (k_f) is only a function of the abstracting radical and of the molecule from which the H-atom is removed (in particular, of the type of hydrogen to be abstracted) and that it can be decomposed into the product of two terms:

$$k_f \approx k^0_{ref,R}\, C_{R'H}$$

$k^0_{ref,R}$ represents the intrinsic reactivity of the R• radical and $C_{R'H}$ is the relative reactivity of the removed H-atom. This is partially justified considering the assumption that the forces between atoms are very short range, meaning that each atom contributes constant amounts to the molecule's properties[19].

The two kinetic constants are expressed in the Arrhenius form:

$$k_f = \left[A^0_{ref,R} \exp\left(-\frac{E^0_{a\,ref,R}}{RT}\right)\right]\left[A_{C_{R'H}} \exp\left(-\frac{E_{a\,C_{R'H}}}{RT}\right)\right]$$

$$k_b = \left[A^0_{ref,R'} \exp\left(-\frac{E^0_{a\,ref,R'}}{RT}\right)\right]\left[A_{C_{RH}} \exp\left(-\frac{E_{a\,C_{RH}}}{RT}\right)\right]$$

The thermodynamic consistency still holds:

$$K_{eq} = \frac{k_f}{k_b} = \frac{k^0_{ref,R}\, C_{R'H}}{k^0_{ref,R'}\, C_{RH}} = 10^{\frac{\Delta S^0}{R}} \exp\left(-\frac{\Delta H^0}{RT}\right)$$

Where ΔS^0 and ΔH^0 are the entropy and enthalpy change in the reaction.

The reference rate constants of the R• radical are estimated from the single primary H-atom abstraction from a methyl group or paraffin from literature data, when available.

The remaining kinetic parameters, that are the relative reactivities of different H-atoms, are derived either from thermodynamic consistency or deduced from the relative importance of different reaction channels.

However, radicals requiring lower activation energies for the H-abstraction (like OH• and Cl•) are less selective with respect to the different H-types. On the contrary, more stable radicals like HO_2• and aC_3H_5• enhance this selectivity. This suggests that a correction has to be applied to the reference activation energies and this correction should be a weak function of the energy itself.

Taking as a reference $E_{a,C}$ for primary alkyl radicals ($E^0_{a\,ref,C_2H_5} = 13500\ kcal/kmol$) it is possible to propose the following empirical relationships for the activation energies of forward (E_f) and backward (E_b) reaction:

$$E_f = E^0_{ref,R} + E_{C_{R'H}}\left(\frac{E^0_{ref,R}}{13500}\right)^{\alpha}$$

$$E_b = E^0_{ref,R'} + E_{C_{RH}}\left(\frac{E^0_{ref,R'}}{13500}\right)^{\alpha}$$

When imposing thermodynamic consistency these expressions have to be slightly corrected and they become:

$$E_f = E^0_{ref,R} + E_{C_{R'H}}\left(\frac{E^0_{ref,R}}{13500}\right)^{\alpha} - \left[1-\left(\frac{E^0_{ref,R'}}{13500}\right)^{\alpha}\right]E_{C_{RH}}$$

$$E_f = E^0_{ref,R'} + E_{C_{RH}}\left(\frac{E^0_{ref,R'}}{13500}\right)^{\alpha} - \left[1-\left(\frac{E^0_{ref,R}}{13500}\right)^{\alpha}\right]E_{C_{R'H}}$$

α is the only fitting parameter in these expressions; on the basis of the whole set of analyzed data, a convenient value of α is about 0.333. In this way it becomes possible to avoid the prediction of negative activation energies and also to reach a better agreement between experimental and calculated k values.

(Adapted from Ranzi, Dente, Faravelli, Pennati, 1994[14]*)*

2.5 MODULARITY, HIERARCHY AND GENERALITY

As the carbon number of the hydrocarbon fuels rises, the detailed reaction schemes become very complex, hence three major features of the Politecnico di Milano model are particularly important: modularity, hierarchy and generality.

The gas-phase kinetic scheme used for simulations, in fact, is divided in subsystems, or modules, each containing a set of reactions related to a species' family. These modules can be added or removed depending on the system and the operative conditions under analysis: if a family of species is not involved, or its reactions are of negligible importance, than the relative module can be removed to lighten the computational burden without changing the simulation results[20,21].

Sensitivity analysis shows that modules do not have the same importance; for example the reaction between radical hydrogen and molecular oxygen contributes in a significant way to the overall reaction rate in practically all combustion systems and therefore the H_2/O_2 module is hierarchically the most important one.

In a hydrocarbon system, the hierarchical order decreases with increasing number of carbon atoms, in fact the species with lower number of carbon atoms are always present in the set of reactions for larger species, while an analysis for combustion of smaller species can be limited to the first products, without going to the heavier ones.

The hierarchy defines also the order for parameters' tuning, because fundamental modules must be tuned first, then the others following the hierarchical order.

The third important feature for a model is generality: it must be able to describe the evolution of different systems operating in a wide range of conditions, from pyrolysis to oxidation, from low to high temperature and pressure etc. In fact, the kinetic model developed in the Department of Chemistry, Materials and Chemical engineering "G. Natta" has been tested with a high number of experimental data in different reactor types, with very different operating conditions in terms of temperatures, pressures and fuels. Image 2.1 schematizes the modularity and hierarchy of the model.

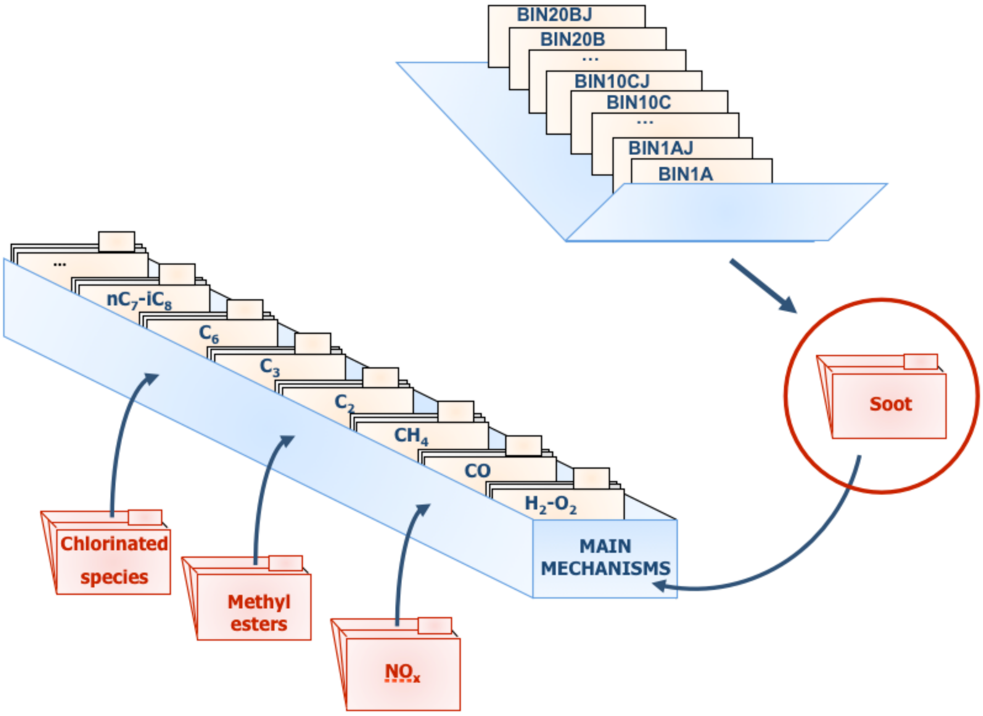

Figure 2.1: Schematic representation of the modularity and hierarchy of the model.

2.6 MODELING AND SIMULATION (OpenSMOKE)

The simulations have been carried out using the software OpenSMOKE, developed by professor Cuoci et al.[22] in the CMIC department in Politecnico di Milano.

Besides the kinetic scheme thermodynamic properties for the species have to be defined. For small molecules properties contained in the CHEMKIN thermodynamic database are used[23].

This database in turn refers to JANAF tables[24], Burcat[25] and quantomechanical calculations.

Also other methods to calculate the properties are applied. For example, Benson's group contributions theory[19] was applied in an approximate way to estimate thermodynamic properties of all the BIN's pseudo-species.

The kinetic scheme and the thermodynamic database are inputs to an interpreter, INTERP, which creates a kinetic model in binary format. This, together with operating conditions and transport properties is the final input to simulate the system in OpenSMOKE. Figure 2.2 shows a scheme on the functioning of the simulation program.

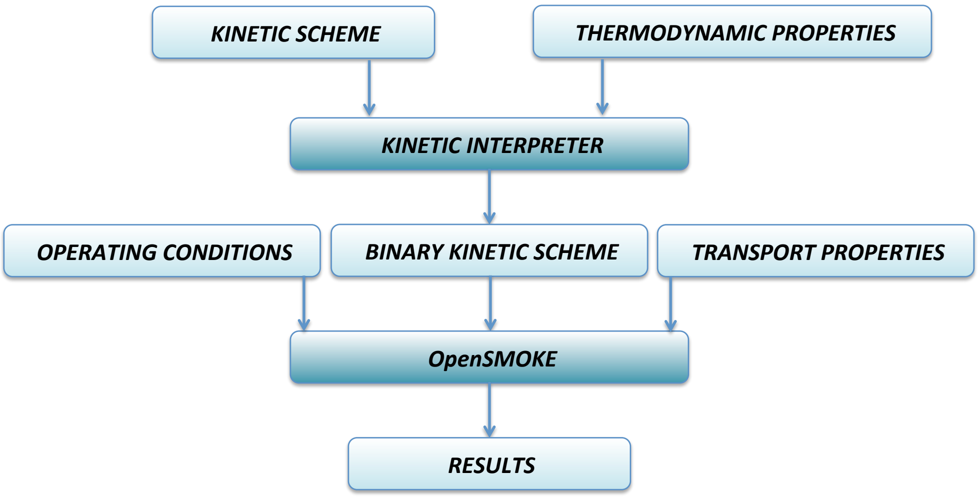

Figure 2.2: Schematic representation of simulation software functioning.

The kinetic scheme used in this work is HT1306s, containing 16558 reactions and 298 species, consisting in coupled gas and solid phase kinetics. The detailed kinetic mechanism for the gas phase describes the pyrolysis and oxidation of a large quantity of fuels at high temperatures and it has been tested following the hierarchical approach referred to the fundamental species C_0-C_4.
The soot scheme is described in detail in chapter 4 and it is built on analogy rules starting from gas phase.

3 Physics of the problem

For a complete description of the system, the kinetic scheme of course must be coupled with a fluid dynamic model able to follow its physical evolution by means of transport equations.

In particular, most of the modeling of soot formation was focused on the analysis of the burner-stabilized stagnation flame described in the work from Hai Wang and coworkers[26] that is a well-defined system in which it is possible to validate and refine the model.

In this configuration, the sampling probe is embedded in a water-cooled circular plate positioned above the flame that acts as a flow stagnation surface (Figure 3.1). This technique allows for a rigorous definition of the flame's boundary conditions taking into account the probe intrusion.

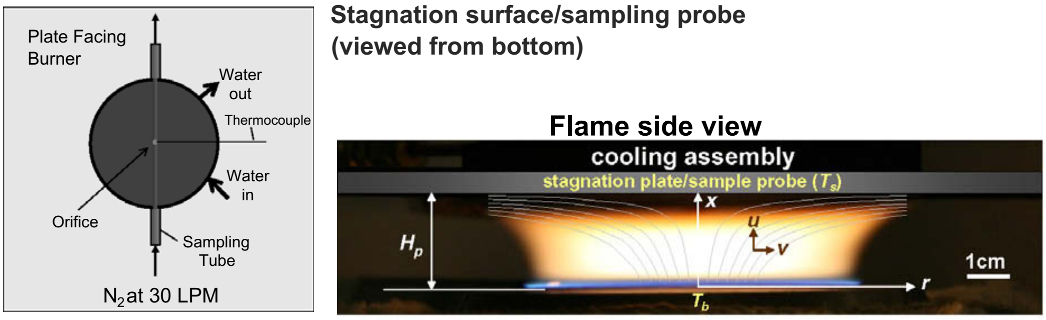

Figure 3.1: Schematic representation of the burner-stabilized stagnation flame configuration. Left panel: water-cooled stagnation surface with the embedded sampling probe as seen from the bottom up of the burner exit. Right panel: flame image and illustration of the coordinate system and flow field[26].

The best way to describe such a configuration is to simulate it as a counterflow flame (Figure 3.2) with zero velocity and diffusivity (except for soot, as explained in paragraph 3.5) on the oxidizer side.

The counterflow configuration consists in two nozzles directed toward each other. In non-premixed flames the fuel stream, made up of fuel and nitrogen, flows from one nozzle, while the oxidizer flows from the opposite nozzle. The stagnation plane formed by the two streams is situated at different positions along the axis depending on the streams' velocities. If, as in our case, the velocity on the oxidizer side is zero, then the stagnation plane coincides with the physical surface of the oxidizer nozzle. The temperature on the stagnation surface is fixed, since in the real setup the plate is water-cooled.

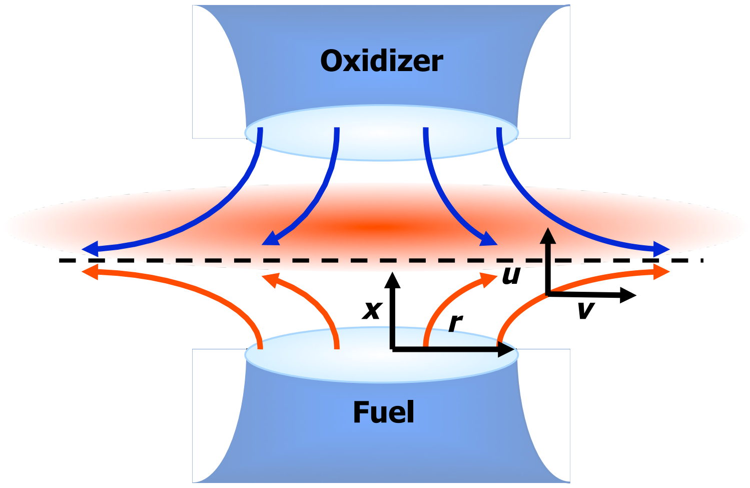

Figure 3.2: Illustration of a counterflow configuration. x and r are the axial and radial coordinates, respectively. u is the axial velocity and v radial one.

The geometry is axisymmetric, thus the governing equations should depend on time, the axial and the radial position.

However, even exploiting the symmetry of the system around the axis, a two-dimensional model would be computationally very demanding, because it would require the solution of the governing equations' system for every point of the grid.

Since the spacing between the nozzles is far smaller than their diameter, we can work under the assumption that the axial velocity (u) and the density (ρ) near the axis are only dependent on the axial coordinate.

Since the evolution of the system along the axis (where the sampling is made) is what we want to describe it becomes possible to model it as one-dimensional.

In paragraph 3.1, the conservation equations used are presented. The mass conservation equation involves a diffusive term, analyzed in detail in paragraph 3.2 through a study focused in particular on the Soret and the thermophoretic effects. A brief overview of the radiative heat losses and their effect on temperature calculation is given in paragraph 3.3. After the governing equations and the boundary conditions for the specific configuration are presented, the effect of thermophoresis near to the stagnation plane is studied through comparison between a one-dimensional and a two-dimensional simulation.

3.1 CONSERVATION EQUATIONS

Global conservation equations express the existing relation between incoming and outcoming fluxes of a given physical quantity, its generated and depleted amount and the cumulated one; they are written for a generic volume unit of the system.

The primitive and general form of these equations, referred to the time unit, is the following:

$$\begin{pmatrix} Cumulated\ amount \\ in\ the\ volume \\ in\ the\ time\ unit \end{pmatrix} = \begin{pmatrix} Resulting\ fluxes\ in\ the\ domain \\ through\ the\ boundary\ surface \\ by\ convection\ and\ diffusion \end{pmatrix} + \begin{pmatrix} total\ generated\ amount \\ inside\ the\ volume\ in\ the \\ time\ unit \end{pmatrix}$$

That, translated in a mathematical form becomes:

$$\frac{d}{dt}\int_V \phi\, dV = -\int_S \boldsymbol{Fl}\, d\boldsymbol{S} - \int_S \phi\boldsymbol{V}\, d\boldsymbol{S} + \int_V R\, dV$$

Where d**S** is the vector normal to a small patch on the surface S and points outwards by convention, ϕ is a generic quantity (units of the quantity per unit volume) that can change within this volume.

Fl is the flux of ϕ in the absence of fluid transport, ϕ**V** is the transport flux (quantity per unit volume per unit time) and R is a source or sink of ϕ.

The negative signs in front of the surface integrals are present because a positive outward flux corresponds to a negative rate of change of the integral on the left[27].

Applying Gauss' theorem the surface integrals in the previous equation can be replaced:

$$-\int_S Fl\, d\boldsymbol{S} - \int_S \phi\boldsymbol{V}\, d\boldsymbol{S} = \int_V \nabla\,(\boldsymbol{Fl} + \phi\boldsymbol{V})dV$$

Because V is of arbitrary shape and size and the surface and volume are fixed in an inertial frame then the above equation becomes:

$$\frac{\partial\phi}{\partial t} + \nabla\,(\boldsymbol{Fl} + \phi\boldsymbol{V}) - R = 0$$

The general concept can be applied to the fundamental balances, referring to the specific quantities for each balance.

Due to the axisymmetric geometry it is more convenient to write the conservation equations of mass, momentum, species and energy in cylindrical coordinates.

3.1.1 Conservation of mass

The principle of mass conservation states that the quantity of mass is conserved over time.

To derive conservation of mass we just substitute ϕ = ρ (density), **Fl** = 0 (mass flux can only change due to transport) and R = 0 (mass cannot be created or destroyed) in the generic equation and the resulting equation is:

$$\frac{\partial \rho}{\partial x} + \nabla(\rho \boldsymbol{V}) = 0$$

This equation is often referred to as “the continuity equation”.

In cylindrical coordinates:

$$\frac{\partial \rho}{\partial t} + \frac{\partial}{\partial x}(\rho u) + \frac{1}{r}\frac{\partial}{\partial r}(r\ \rho v) = 0$$

Where r is the radial coordinate and v is the radial velocity (Figure 3.2).

From the hypotheses that u and ρ depend on x only, it is possible to obtain:

$$\frac{1}{r}\frac{\partial}{\partial r}(r\ v) = 2f(x)$$

Integrating:

$$v = f(x)\, r$$

$$\frac{\partial v}{\partial r} = f(x) = \frac{v}{r}$$

Thus the radial velocity is a linear function of the radius with a coefficient that depends on the axial coordinate (x). Substituting in the continuity equation:

$$\frac{\partial \rho}{\partial t} + \frac{\partial}{\partial x}(\rho u) + 2\rho \frac{v}{r} = 0$$

Two functions are defined for convenience:

$$F(x) = \frac{\rho u}{2}$$

$$G(x) = -\frac{\rho v}{r}$$

So that the continuity equation becomes:

$$\frac{\partial \rho}{\partial t} = 2\left(G - \frac{\partial F}{\partial x}\right)$$

3.1.2 Conservation of momentum

Momentum is a vector field. In general momentum is m**V**, therefore the amount of momentum per unit volume is ϕ = ρ**V**. There are two kind of forces that can change the momentum: the stress that acts on the surface of the volume with local force **f** = **σ** d**S** that can also be thought as a flux of force **Fl** = -**σ** (the negative sign ensures that if the net force on the volume points in, the momentum increases) and the body forces such as gravity, which act like a source of momentum; thus R = ρ**g**, where **g** is the net acceleration.

The equation for the momentum conservation becomes then:

$$\frac{\partial \rho \boldsymbol{V}}{\partial t} + \nabla\,(\rho \boldsymbol{V}\boldsymbol{V}) = -\nabla\, P + \rho \boldsymbol{g}$$

In the axial direction, as derived in “Transport phenomena[28]”, the equation can be written as:

$$\rho \frac{Du}{Dt} = -\frac{\partial P}{\partial x} - \left(\frac{1}{r}\frac{\partial}{\partial r}(r\,\tau_{rx}) + \frac{\partial \tau_{xx}}{\partial x}\right)$$

Where Du/Dt is the substantive derivative and the stress tensors are defined as:

$$\tau_{rx} = -\mu\left(\frac{\partial u}{\partial r} + \frac{\partial v}{\partial x}\right)$$

$$\tau_{xx} = -\mu\left(2\frac{\partial u}{\partial x} - \frac{2}{3}\nabla\vec{u}\right)$$

If we substitute these expressions and the functions above defined in the momentum equation in the axial direction we obtain:

$$\frac{\partial P}{\partial x} = -4F\frac{\partial}{\partial x}\left(\frac{F}{\rho}\right) - 2\mu\frac{\partial}{\partial x}\left(\frac{1}{\rho}\frac{\partial F}{\partial x}\right) + \frac{4}{3}\frac{\partial}{\partial x}\left[2\mu\frac{\partial}{\partial x}\left(\frac{F}{\rho}\right) + \nu\frac{\partial F}{\partial x}\right]$$

Similarly, in the radial direction:

$$\rho \frac{Dv}{Dt} = -\frac{\partial P}{\partial r} - \left(\frac{1}{r}\frac{\partial}{\partial r}(r\,\tau_{rr}) - \frac{\tau_{\theta\theta}}{r} + \frac{\partial \tau_{rx}}{\partial x}\right)$$

Where the stress tensor components have the following expressions:

$$\tau_{rr} = -\mu\left(2\frac{\partial v}{\partial r} - \frac{2}{3}\nabla\vec{u}\right)$$

$$\tau_{\theta\theta} = -\mu\left(2\frac{v}{r} - \frac{2}{3}\nabla\vec{u}\right)$$

$$\tau_{rx} = -\mu\left(\frac{\partial u}{\partial r} - \frac{\partial v}{\partial x}\right)$$

The final form becomes:

$$\frac{1}{r}\frac{\partial P}{\partial r} = \frac{\partial}{\partial x}\left(\frac{2F}{\rho}\frac{\partial F}{\partial x}\right) - \frac{3}{\rho}\left(\frac{\partial F}{\partial x}\right)^2 - \frac{\partial}{\partial x}\left[\mu\frac{\partial}{\partial x}\left(\frac{1}{\rho}\frac{\partial F}{\partial x}\right)\right]$$

From the final forms of the conservation equations in the two directions it is evident that $\frac{\partial P}{\partial x}$ and $\frac{1}{r}\frac{\partial P}{\partial r}$ depend on the coordinate x only. This means that the only possibility is:

$$\frac{1}{r}\frac{\partial P}{\partial r} = H = const$$

H is an eigenvalue of the resulting system. After some rearrangements, the equation of conservation of momentum in the radial direction becomes:

$$\frac{\partial}{\partial x}\left[\mu\frac{\partial}{\partial x}\left(\frac{G}{\rho}\right)\right] - 2\frac{\partial}{\partial x}\left(\frac{FG}{\rho}\right) + \frac{3}{\rho}G^2 + H = 0$$

3.1.3 Conservation of species

For the species, the quantity ϕ is the mass of the species k ($\rho_k = \rho\,\omega_k$, where ω_k is the mass fraction). The flux **Fl** = 0 and the transport flux is due to convection and diffusion, hence $m\boldsymbol{V} = \rho_k\vec{u} + \overrightarrow{J_k}$, with $\overrightarrow{J_k}$ being the molecular diffusive flux of the k species. The source term $R = \dot{\Omega}_k$, where $\dot{\Omega}_k$ is the mass reaction rate per unit volume.

The mass conservation equation can be thus written as:

$$\frac{\partial}{\partial t}(\rho\omega_k) + \nabla(\rho\vec{u}\omega_k) = -\nabla\overrightarrow{J_k} + \dot{\Omega}_k \qquad\qquad k = 1 \dots N_s$$

Where N_S is the number of species.

The molecular diffusive flux is usually written in terms of a diffusion velocity $\vec{V}_k$:

$$\overrightarrow{J_k} = \rho\omega_k\vec{V}_k$$

This diffusion velocity is the sum of three contributions that will be analyzed in detail later in the chapter.

The final form of the equation can be found by using the last expression and the definition of the variable F:

$$\rho\left[\frac{\partial \omega_k}{\partial t}+\frac{2F}{\rho}\frac{\partial \omega_k}{\partial x}\right]=-\frac{\partial}{\partial x}(\rho\omega_k V_k)+\dot{\Omega}_k \qquad\qquad k=1\dots N_s$$

3.1.4 Conservation of energy

For a single phase material, the amount of heat per unit volume is $\phi = \rho C_P T$ where C_P is the specific heat at constant pressure and T is the temperature. The heat flux in the absence of transport is $\boldsymbol{Fl}=-\lambda\nabla T$, where λ is the thermal conductivity. The transport flux is $\rho C_P T\mathbf{V}$. Since the Mach number in the counterflow diffusion flames is very small, we neglect the terms associated to the viscous dissipation and to the pressure. Also the kinetic and potential energy can be neglected.

The source term is therefore the radiative heat flux $R=\dot{Q}$.

The simplest conservation of heat equation is:

$$\frac{\partial \rho C_P T}{\partial t}+\nabla\,(\rho C_P T\boldsymbol{V})=\nabla\,\lambda\nabla T+\dot{Q}$$

Manipulating the equation considering also the mass conservation and the definition of variable F we obtain:

$$\rho\hat{C}_P\left[\frac{\partial T}{\partial t}+\frac{2F}{\rho}\frac{\partial T}{\partial x}\right]=\frac{\partial}{\partial x}\left[\lambda\frac{\partial T}{\partial x}\right]-\rho\sum_{k=1}^{N_S}\hat{C}_{P,k}\omega_k V_k\frac{\partial T}{\partial x}+\dot{Q}-\sum_{k=1}^{N_S}\widehat{H}_k\dot{\Omega}_k$$

$\widehat{H}_k$ is the specific enthalpy for the species k, so the term $R=\sum_{k=1}^{N_S}\widehat{H}_k\,\dot{\Omega}_k$ represents the heat released by combustion.

(Adapted from *Cuoci A., Pollutant formation in turbulent reactive flows: interactions between chemistry and turbulence, Ph.D. Thesis in Chemical Engineering, Politecnico di Milano (2008)*)

3.2 DIFFUSIVITY

As mentioned earlier, the molecular diffusion flux is usually expressed in terms of a diffusive velocity V_k, which is the sum of three contributions: Fick's, Soret's and thermophoretic's diffusion. It is interesting to analyze them to understand how differently they contribute to the species' transport.

3.2.1 Fick diffusivity

The first driving force for species diffusion is a concentration gradient. This is the dominant mode of transport. The diffusion velocities should be obtained by solving the system[29]:

$$\nabla X_P = \sum_{k=1}^{N_S} \frac{X_p X_k}{\Gamma_{pk}^{(m)}} \left(V_k - V_p\right) + \left(Y_p - X_p\right) \frac{\nabla P}{P} + \frac{\rho}{p} \sum_{k=1}^{N_S} Y_p Y_k \left(f_p - f_k\right) \qquad for\ p = 1 \ldots N_S$$

Where $\Gamma_{pk}^{(m)}$ is the binary mass diffusion coefficient of the species *k* in species *p* and X_k is the mole fraction of species *k*.

This is a linear system of size N_S^2 which must be solved in each direction at each point and at each instant for unsteady flows. This is computationally very costly, but usually a simplified approach based on Fick's law is acceptable. According to Fick's law the diffusion velocity can be written as:

$$\omega_k \vec{V}_k^{(m)} = -\Gamma_{k,mix}^{(\mathrm{m})} \nabla \omega_k$$

With $\Gamma_{k,mix}^{(\mathrm{m})}$ mass diffusion coefficient of the species k in the mixture.

From this definition, it derives that the diffusive molecular flux is:

$$\overrightarrow{J_k}^{(m)} = -\rho \Gamma_{k,mix}^{(\mathrm{m})} \nabla \omega_k$$

As it can be noticed, Fick's diffusion depends on the species' mass fractions, since it is related to a composition gradient.

3.2.2 Soret diffusivity

The Soret effect is a phenomenon of mass diffusion in the presence of a temperature gradient, it acts sensibly only on species with a very small molecular mass (for example hydrogen), but it is very important to follow the evolution of the system, because, especially in the configuration under consideration, there is a strong temperature gradient near the stagnation surface, hence it strongly modifies the hydrogen profile.

As explained in the following chapter, the hydrogen plays a fundamental role in the reactivity of the system, hence, if the hydrogen profile is modified, by consequence also the heavier species' profiles are modified and the soot production cannot be described properly.

The diffusive flux due to the Soret effect is defined analogously to the Fick one:

$$\overrightarrow{J_k}^{(T)} = -\rho \Gamma_{k,mix}^{(\mathrm{T})} \nabla lnT$$

Where $\Gamma_{k,mix}^{(\mathrm{T})}$ is the thermal diffusion coefficient of the species k into the mixture.

A simulation of a burner-stabilized stagnation flame was carried out including and excluding the Soret effect from the model. The flame chosen is the one from Wang and coworkers previously mentioned[26] with the stagnation plane positioned 1 cm above the burner surface.

The flame is an ethylene premixed laminar flame (16.3% ethylene, 23.7% oxygen, 60% argon flame) with an equivalence ratio of 2.07.

As shown in figure 3.3, the Soret effect strongly affects the hydrogen structure, by direct effect, especially in the stagnation plane proximity, where there is a marked temperature gradient.

As stated before, it can be clearly observed that as a consequence also the PAHs profiles along the flame axis are modified and soot evolution cannot be predicted properly (Figure 3.4).

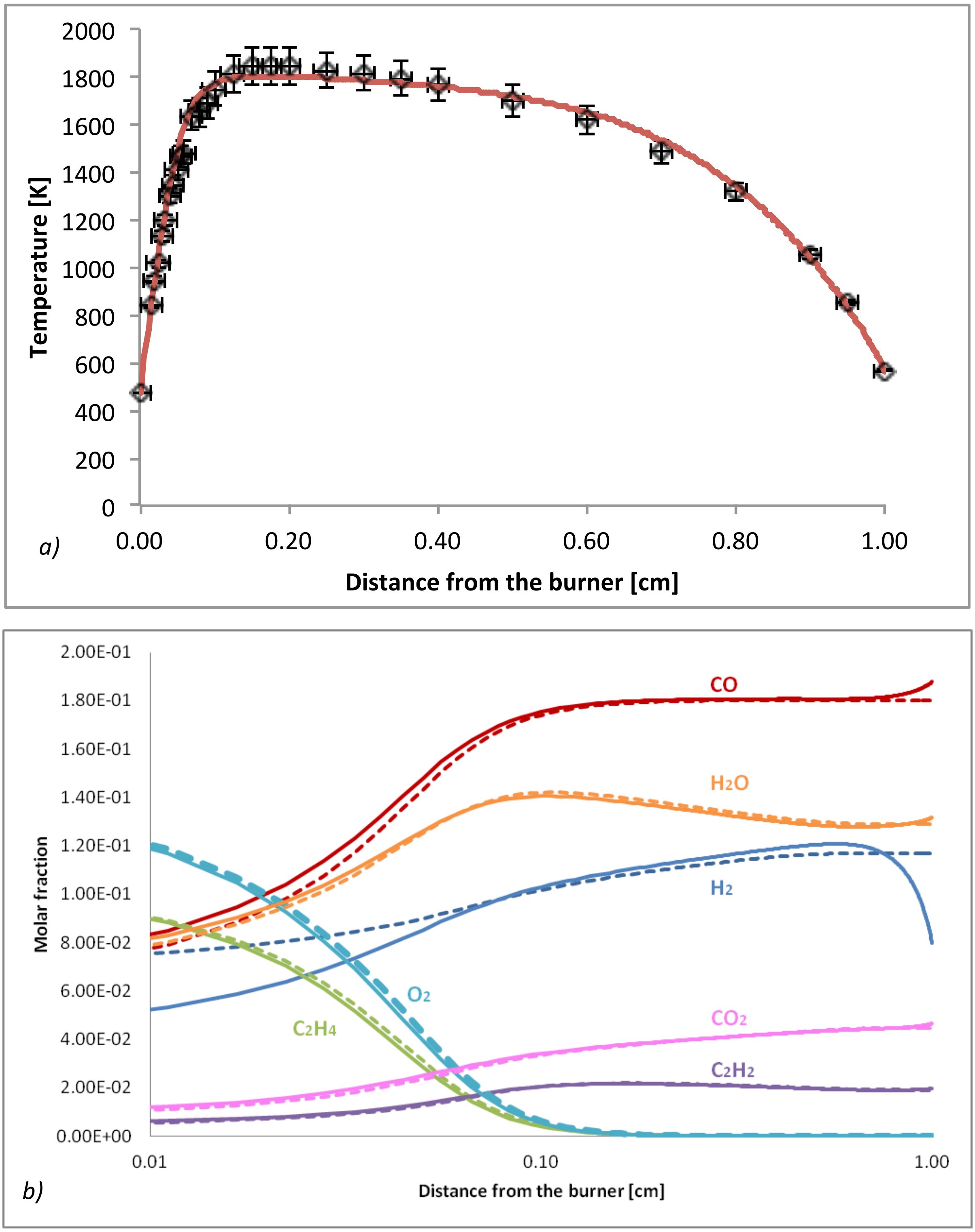

Figure 3.3: Simulation results of the burner-stabilized stagnation flame: Temperature (calculated vs experimental, figure *a*), and flame structure (figure *b*). Solid lines: results from the simulation including the Soret effect. Dashed lines: results from the simulation without the Soret effect implemented.

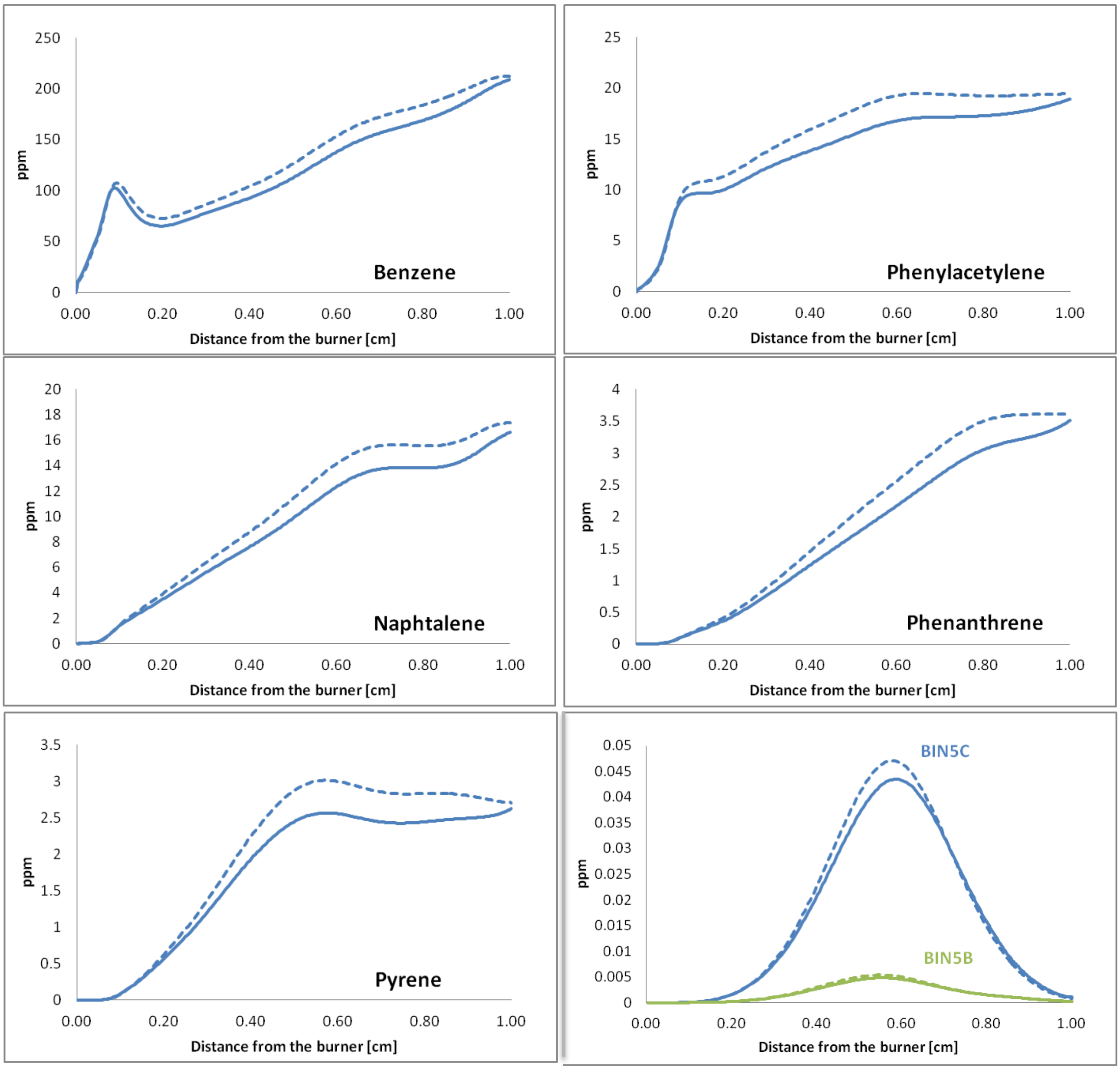

Figure 3.4: Simulation results of the burner-stabilized stagnation flame: PAHs profiles. Solid lines: results from the simulation including the Soret effect. Dashed lines: results from the simulation without the Soret effect implemented.

The flame is lightly sooty, PAHs and soot concentrations are not very high, therefore the modifications of the heavy species' profiles because of the Soret effect are about 10%.

In more sooty flames the Soret effect is still very important on hydrogen, but the relative weight on the heavier species' profiles changes is very low. In fact, for example, if we look at the benzene profile, the shift is always about 10 ppm, as in the case illustrated above, but the total benzene concentration is as high as 1500 ppm, therefore the relative weight is less than 1%.

3.2.3 Thermophoretic diffusion

Thermophoresis is the term describing the phenomenon wherein small particles, such as soot particles, suspended in a gas characterized by a temperature gradient ∇T, drift in the direction opposite to that of ∇T. It can be seen as a particular case of the Soret effect acting on aerosols.
Therefore, also the expression of the thermophoretic diffusive flux reflects this similarity and it is defined as:

$$\overrightarrow{J_k}^{(Th)} = -\rho\Gamma_{k,mix}^{(\mathrm{Th})}\nabla lnT$$

The only difference with respect to the Soret flux lies in the definition of the thermophoretic diffusion coefficient of the species k into the mixture, $\Gamma_{k,mix}^{(\mathrm{Th})}$.
Assuming spherical particles in free molecular regime (Kn_p>>1), which is the case of soot particles, the thermophoretic diffusivity (D_T) can be expressed as[30,31]:

$$D_T = \left(\frac{3}{4}\right)\left[1 + \left(\frac{\pi}{8}\alpha\right)\right]^{-1} \nu$$

Where:

- α, the momentum accommodation coefficient, can be set equal to unity[31];
- ν is the momentum diffusivity (kinematic viscosity) of the prevailing gas mixture.

The thermophoretic velocity becomes then:

$$\vec{V}_k^{(Th)} = -0.538\, \nu \frac{\nabla T}{T}$$

As shown by the formulas, the thermophoretic velocity (for the considered case) does not depend on particles size.
Some simulations to point out the role of thermophoresis near to the stagnation plane will be shown later after a brief explanation on the boundary conditions.

3.3 RADIATIVE HEAT LOSSES

In the energy conservation equation the term $\dot{Q}$ represents the radiative heat loss from the flame to the environment and it can be seen as the gradient of a heat flux vector:

$$\dot{Q} = -\nabla \mathbf{q}^{\mathbf{rad}}$$

An optically thin radiation model is used to represent the gas phase. For the mixtures here considered, it is assumed that the only significant radiating species are H_2O, CO, CO_2 and CH_4. In the optically thin model the self-absorption is neglected, hence the divergence of the net radiative flux can be written as:

$$\nabla \boldsymbol{q}^{\boldsymbol{rad}} = -4\sigma a_g (T^4 - T_{env}^4)$$

Where σ is the Stefan-Boltzmann constant and T_{env} the environment temperature. The Planck mean absorption coefficient a_P is evaluated according to the following expression:

$$a_g = p_{H_2O} a_{P,H_2O} + p_{CO_2} a_{P,CO_2} + p_{CO} a_{P,CO} + p_{CH_4} a_{P,CH_4}$$

Where p_k is the partial pressure of species *k*. The extinction coefficient $a_{P,k}$ of species *k* is derived from calculations performed by the RADCAL software[32,33].

In sooty flames, the radiation absorption coefficient has to include the effect of soot concentration. The absorption coefficient of a mixture of soot and an absorbing gas is calculated as the sum of the absorption coefficients of pure gas and pure soot:

$$a_{s+g} = a_g + a_s$$

Where a_g is the absorption coefficient of gas without soot calculated as explained above and the absorption coefficient of pure soot is:

$$a_s = b_1 \rho_m [1 + b_T (T - 2000)]$$

with $b_1 = 1232.4\ \mathrm{m}^2/\mathrm{kg}$ and $b_T \approx 4.8\ 10^{-4}\ \mathrm{K}^{-1}$. ρ_m is the soot density.

The coefficients b_1 and b_T result from a fitting[34] of the soot absorption coefficient to data based on the Taylor-Foster approximation[35] and data based on the Smith et al. approximation[36]. This model is similar to the one implemented in FLUENT.

For the flame described earlier, the temperature profile (already shown in Paragraph 3.2.2) was computed with and without radiative heat losses to show the effect of the different contributions. The flame, as already mentioned, is lightly sooty, therefore the contribution of soot radiation is negligible, whereas the gas radiation is essential to describe properly the temperature profile.

In fact, as shown in figure 3.5, only by considering the radiation the measured profile can be matched within the experimental error.

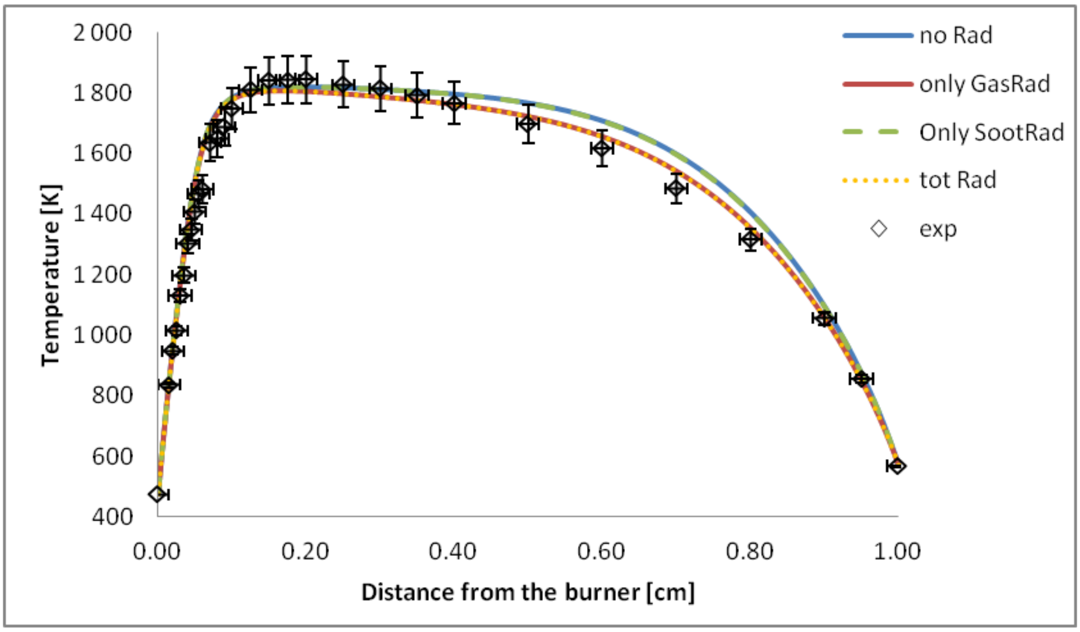

Figure 3.5: Experimental (exp) and computed temperature profiles for the burner-stabilized stagnation flame from Wang and coworkers (equivalence ratio 2.07) with a distance stagnation plane-burner of 1 cm. Solid blue line: computation result without radiative heat losses; solid red line: computation result considering only gas radiation; dashed green line: only soot radiation considered in the simulation; dotted yellow line: all the radiative terms are considered.

Of course, the more sooty the flame is and the more important the soot radiation term becomes.

3.4 GOVERNING EQUATIONS FOR COUNTERFLOW DIFFUSION FLAMES

The system to be solved consists of the conservation equations summarized below and the boundary conditions for the dependent variables (G, F, H, ω_k, T).

$$\frac{\partial \rho}{\partial t} = 2\left(G - \frac{\partial F}{\partial x}\right)$$

$$\frac{\partial}{\partial x}\left[\mu \frac{\partial}{\partial x}\left(\frac{G}{\rho}\right)\right] - 2\frac{\partial}{\partial x}\left(\frac{FG}{\rho}\right) + \frac{3}{\rho}G^2 + H = 0$$

$$\frac{1}{r}\frac{\partial P}{\partial r} = H = const$$

$$\rho\left[\frac{\partial \omega_k}{\partial t} + \frac{2F}{\rho}\frac{\partial \omega_k}{\partial x}\right] = -\frac{\partial}{\partial x}(\rho \omega_k V_k) + \dot{\Omega}_k \qquad k = 1 \dots N_s$$

$$\rho \hat{C}_P\left[\frac{\partial T}{\partial t} + \frac{2F}{\rho}\frac{\partial T}{\partial x}\right] = \frac{\partial}{\partial x}\left[\lambda \frac{\partial T}{\partial x}\right] - \rho \sum_{k=1}^{N_S} \hat{C}_{P,k}\omega_k V_k \frac{\partial T}{\partial x} + \dot{Q} - \sum_{k=1}^{N_S} \widehat{H}_k \dot{\Omega}_k$$

The boundary conditions deserve a special mention, since they are critical to describe the system near to the stagnation plane surface, where the sampling is made.

3.4.1 Boundary conditions

For a normal counterflow flame the boundary conditions for the fuel (*F*) and oxidizer (*O*) at the nozzles would be:

$$Fuel\ side\ (x = 0)\begin{cases} F = \dfrac{\rho_F u_F}{2} \\ G = 0 \\ T = T_F \\ \rho u \omega_k + \rho \omega_k V_k = (\rho u \omega_k)_F \end{cases}$$

$$Air\ side\ (x = L)\begin{cases} F = \dfrac{\rho_O u_O}{2} \\ G = 0 \\ T = T_O \\ \rho u \omega_k + \rho \omega_k V_k = (\rho u \omega_k)_O \end{cases}$$

It is worth noticing that normally the nominal flux at the nozzles is equal to the sum of the convective and the diffusive fluxes, so that if gradients exist at the boundary, these conditions allow diffusion into the nozzle, resulting in a more accurate description.

In the specific case under analysis, the nominal flux on the air side is zero, so for the gaseous species the sum of the convective and the diffusive terms is zero too.

For the soot particles, instead, the total flux at the oxidizer boundary is not zero, because soot, due to the thermophoretic force, deposits on the stagnation wall. Hence, the boundary condition for the species on the air side becomes:

$$\rho u \omega_k + \rho \omega_k V_k = 0 \qquad for\ the\ gaseous\ species$$

$$\rho u \omega_k + \rho \omega_k V_k = \rho \omega_k V_k^{(Th)} \qquad for\ the\ particles$$

3.5 THERMOPHORETIC EFFECT AT THE STAGNATION PLANE: SIMULATIONS IN NON-REACTIVE FLOW

To understand better the thermophoretic effect in the system under analysis, a study was carried out on a non-reactive flow in a stagnation-plane configuration, both in one and two dimensions. The stream is fed through the burner nozzle and has the characteristics illustrated in Table 3.1.

Composition (Mass fraction)		Inlet Temperature [K]	Gas velocity [cm/s]	Distance between the nozzles [cm]
N_2	**99.996%**	700	13	1
BIN5A	**0.001%**			
BIN11A	**0.001%**			
BIN15A	**0.001%**			
BIN19A	**0.001%**			

Table 3.1: Characteristics of the non-reactive flow fed through the fuel nozzle.

The oxidizer side acts as a stagnation plane. In the one-dimensional simulation the wall is set at different temperatures (T_W) to follow the changes in the soot mass fraction profile due to the thermophoretic effect, while the inlet temperature (T_g) is always 700 K (Figure 3.6). It appears clearly that when the wall temperature is lower than the gas temperature soot deposits on the wall and its mass fraction drops. The lower the wall temperature is, the more pronounced the flux becomes. Of course if the wall temperature is the same as the gas one, the soot mass fraction is constant along the axis and the thermophoretic velocity is zero. On the contrary, if the wall temperature is higher, the thermophoretic velocity is negative, directed toward the fuel nozzle and the particles are rejected from the stagnation surface. Once again, the higher is the wall temperature over the gas temperature ratio and the bigger is the absolute value of the thermophoretic velocity.

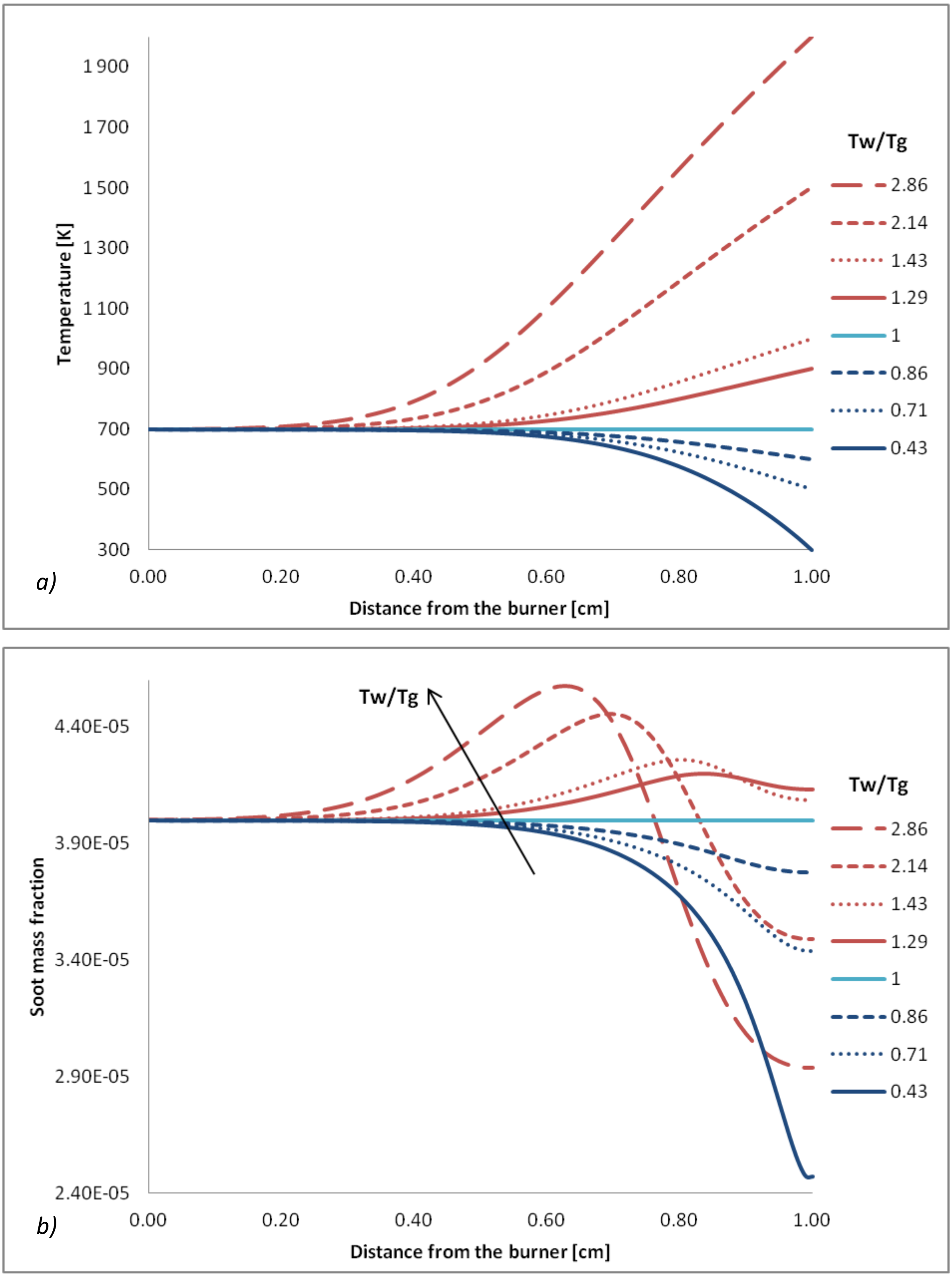

Figure 3.6: One-dimensional simulation of the effect of the wall temperature (T_W) on the soot mass fraction in the non-reactive flow described above. The inlet temperature (T_g) is 700 K for all the cases. Figure *a*: Red: wall temperature higher than the gas temperature. Blue: wall temperature colder than the gas one.

In order to validate the method used, a CFD (computational fluid dynamics) simulation of the same configuration was carried out using laminarSMOKE, a open-source OpenFOAM® code[33] developed inside the CMIC department of Politecnico di Milano by professor Cuoci and coworkers. Due to the symmetry with respect to the burner axis, in the simulation only half of the diameter was considered. In figure 3.7 the 3D device schematization is shown and the dashed lines define the simulated field.

The stream enters through the inlet (light blue circle on the burner) and is deviated by the stagnation plane at 1 cm on the z axis. On the x axis, the inlet is only 2.5 cm wide because the real diameter would be 5 cm, but again, only half of the real geometry is considered. The stream exits the boundaries from the outlet, located on the left.

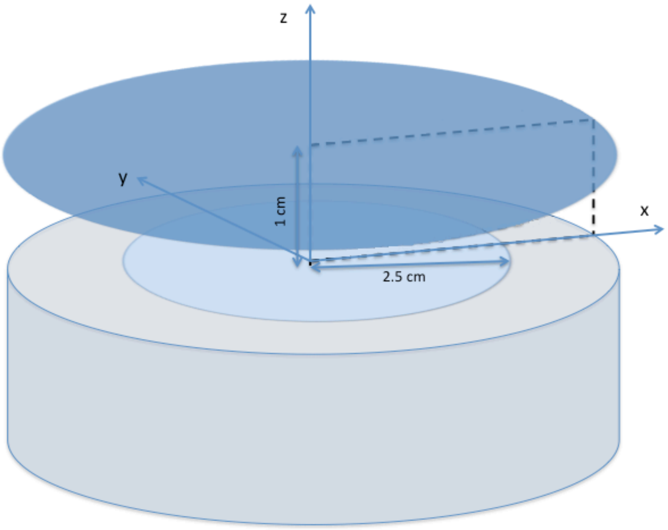

Figure 3.7: Schematization of the stagnation plane configuration. The cylinder represents the burner, the inlet is the light blue circle and the stagnation surface is the darker blue circle at 1 cm above the burner. The feed exits the system from the side. The dashed lines define the simulated field.

Only the two extreme cases were simulated, with the wall temperature at 300 K and 1500 K.

In all the images the inlet is on the bottom right and the outlet is on the left.

The streamlines, illustrated in figure 3.8, clearly show how the stagnation plane modifies the fluid dynamics of the system.

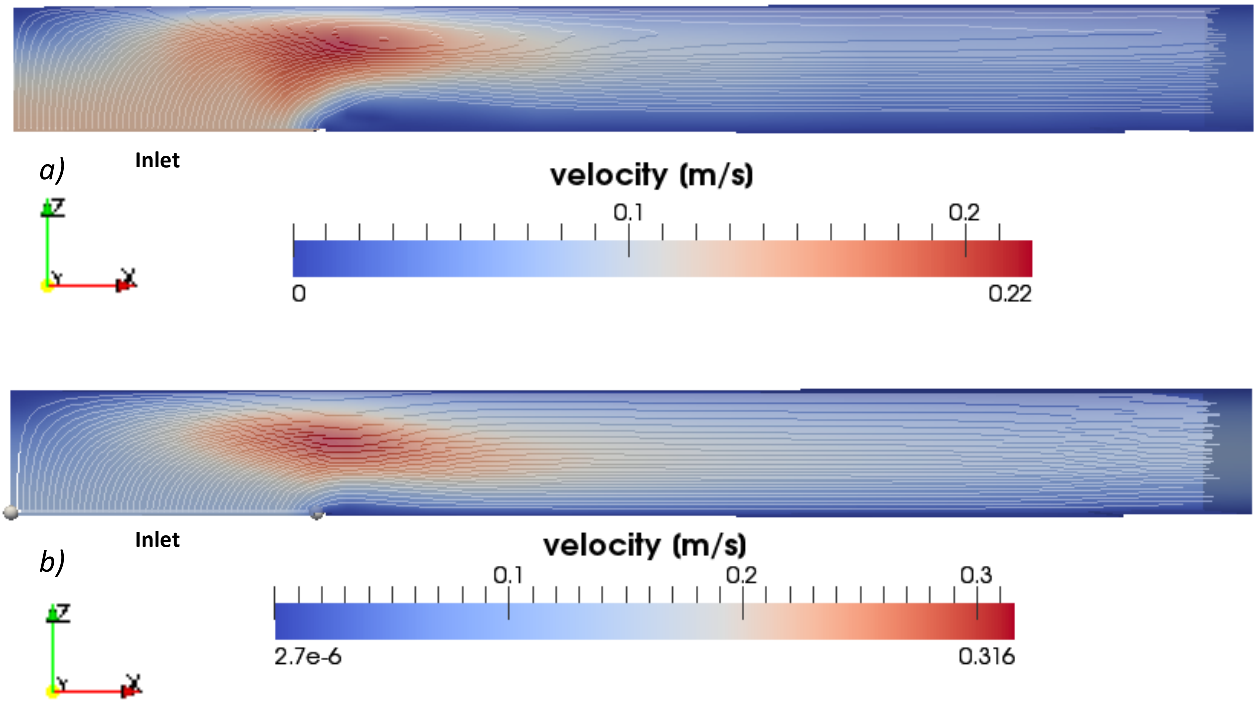

Figure 3.8: Streamlines and velocity field if the wall temperature is *a)* 300 K, *b)* 1500 K from the two-dimensional simulation.

It is interesting to compare the temperature fields with the thermophoretic velocity in the two cases (Figure 3.9).

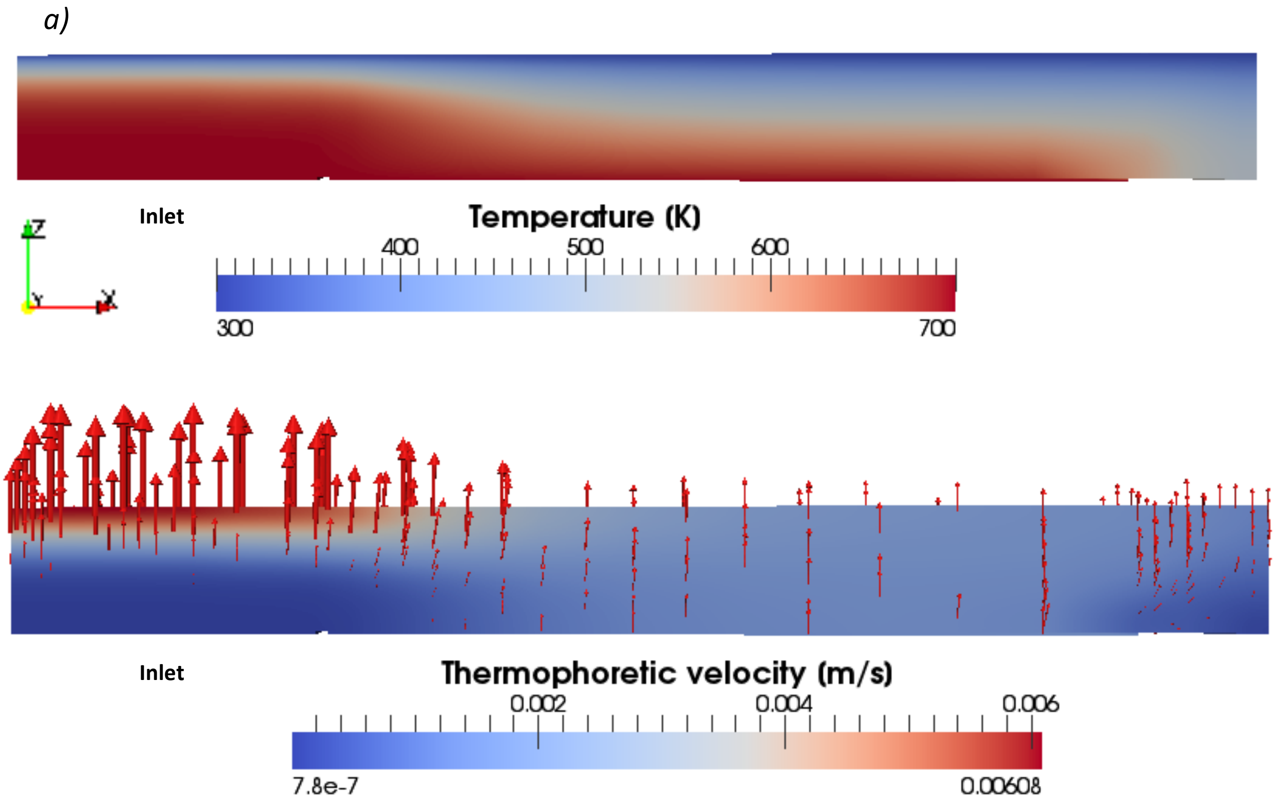

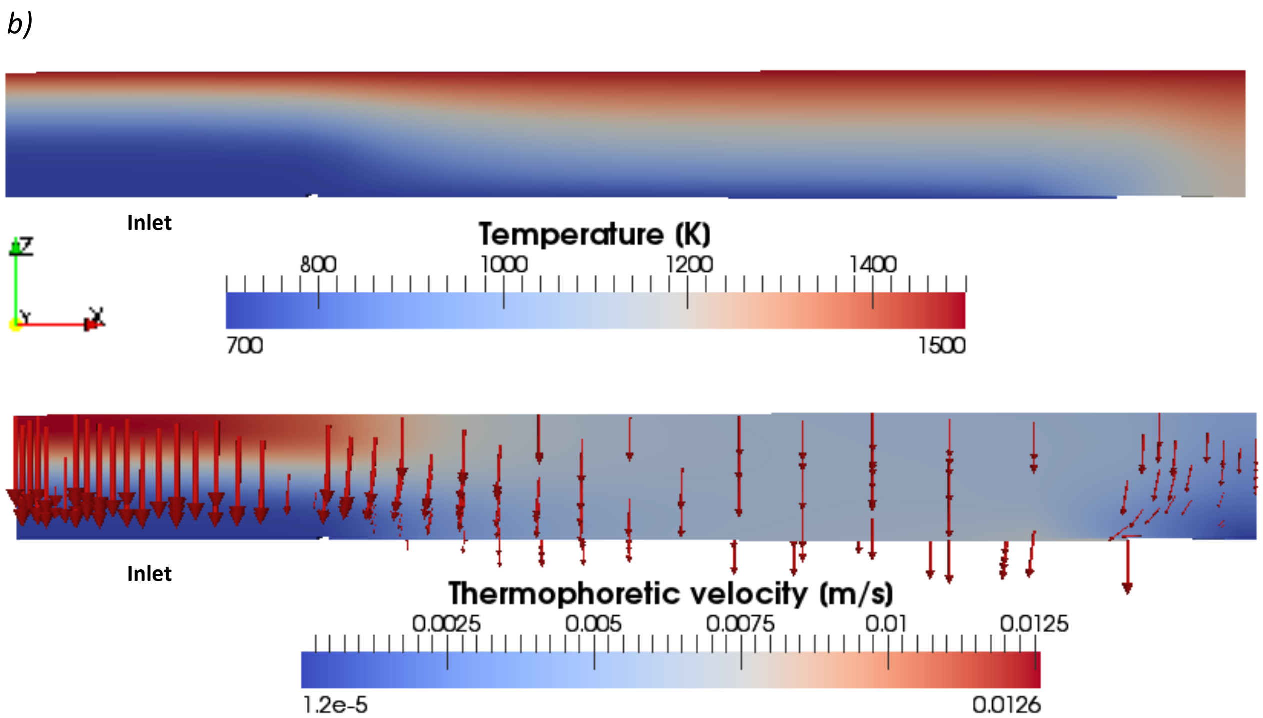

Figure 3.9: Temperature and thermophoretic velocity fields if the wall temperature is *a)* 300 K, *b)* 1500 K from the two-dimensional simulation.

It provides a clear view of how the thermophoretic force acts depending on the temperature gradient. If the wall temperature is 300 K the thermophoretic velocity is directed upwards, thus the particles are attracted to the wall. On the contrary, if the wall temperature is 1500 K the thermophoretic velocity is directed downwards and particles move away from it.

Moving along the x axis, away from the symmetry axis, the temperature gradient near to the wall decreases and the thermophoretic velocity too by consequence.

The soot mass fraction profiles reflect the thermophoretic velocity field. In the images from Figure 3.10 it is plotted as a function of the distance from the burner at various distances from the symmetry axis (hence at different positions on the x axis).

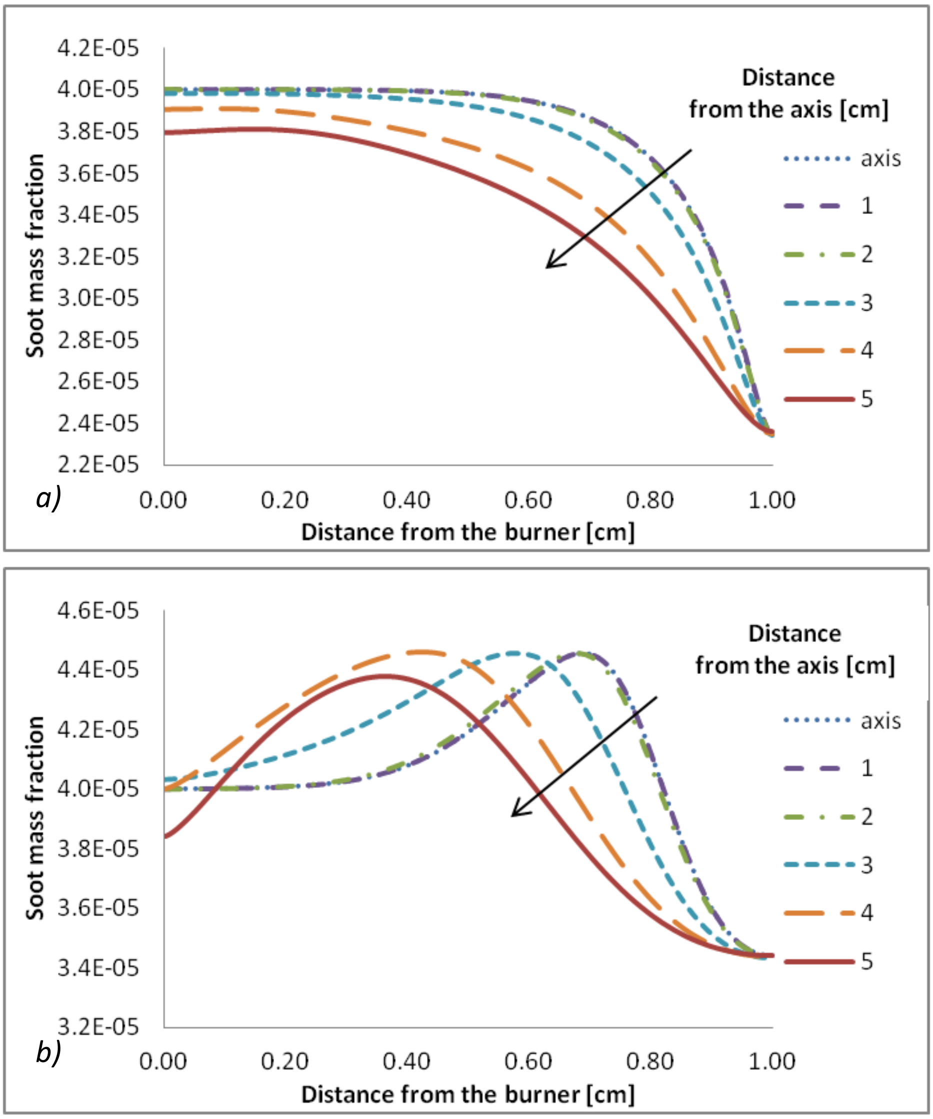

Figure 3.10: Soot mass fraction profiles as a function of the distance from the burner (z coordinate) at different distances from the symmetry axis (different x coordinates) if the wall temperature is *a)* 300 K, *b)* 1500 K from the two-dimensional simulation.

If we compare the results of the one- and two-dimensional simulations along the axis it can be observed how they are almost identical, apart from a very small deviation of the soot mass fraction next to the stagnation plane (Figure 3.11).

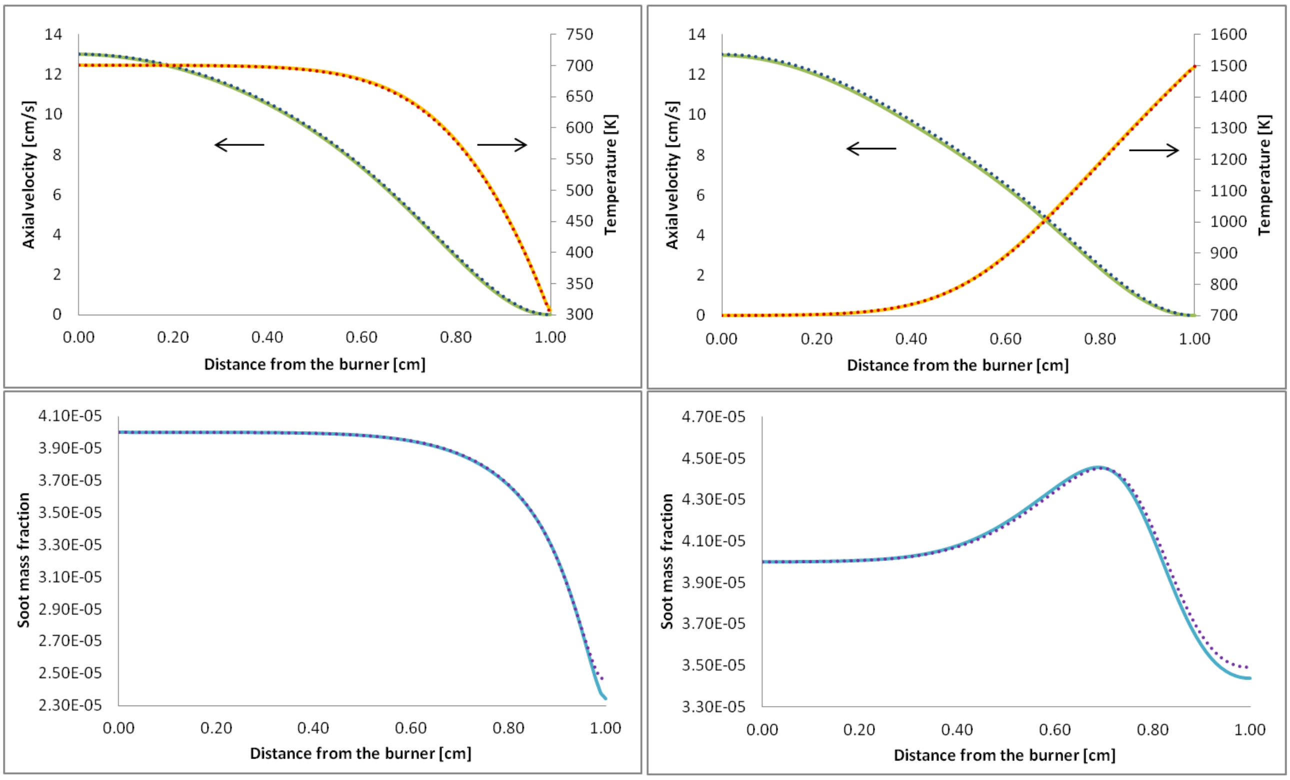

a) *b)*

Figure 3.11: Comparison of the results obtained with OpenSMOKE (one-dimensional, dotted lines) and laminarSMOKE (two-dimensional, solid lines) when the wall temperature is 300 K (case *a*, left panels) and 1500 K (case *b*, right panels).

Therefore the one-dimensional approach is fully justified, also considering the remarkable savings in terms of computational costs.

4 Kinetic pathways for soot formation

Soot formation is a complex process involving many chemical and physical steps.

Several theories have been proposed to explain it; each one hypothesizing different pathways, but there are some milestones on which all of them agree.

In fact, it is widely accepted that soot formation consists in the following partially parallel processes:

- *Particles nucleation*. PAHs in gas phase, molecules or radicals, at some size interact with each other while individual PAHs keep growing: particle inception occurs.
- *Surface growth*. Soot particles grow in mass through surface reactions.
- *Particles coagulation and aggregation*. Particles size increases further by collision of growing soot particles. Initially, colliding entities coalesce completely yielding new spherical structures while later they agglomerate into fractal units.
- *Oxidation*. Molecular oxygen and OH radical react with the particles that therefore lose mass.

The different models differ on *how* these processes happen, by means of which reactions or which physical processes.

In this chapter a brief overview of the different possible kinetic pathways and approaches to modeling is given, with a particular focus on the discrete sectional model developed from the CRECKmodeling group in “Politecnico di Milano” and the one used from D’Anna and coworkers in “Università degli Studi Federico II di Napoli”.

4.1 THERMODYNAMIC ASPECTS

The formation of the first aromatic ring is the first step in soot nucleation, but it is not the only bottleneck of the process. On the contrary, there are several rate limiting steps[37] that must be analyzed taking into account also the thermodynamics of the problem.

The driving force for soot formation is either a decrease in the enthalpy due to chemical bond formation or an increase in entropy because of gas-phase species released during particles' formation.

The sooting process is entropy-driven, as shown in figure 4.1.

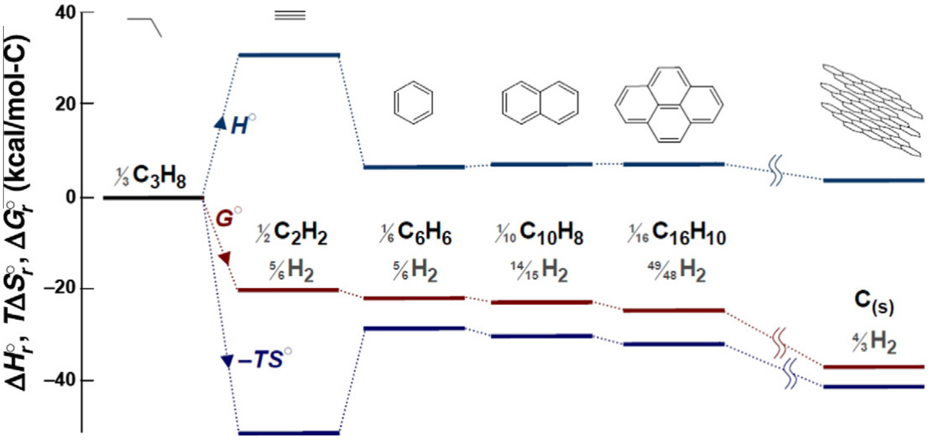

Figure 4.1: Enthalpy and entropy contributions to Gibbs free energy at 1600 K for the formation of solid carbon from propane[38].

The overall process is slightly endothermic and the increase in entropy is not very strong, hence not only it is kinetically controlled, but the kinetics is also highly reversible[38].

4.2 POLYCYCLIC AROMATIC HYDROCARBONS FORMATION AND GROWTH

The formation and growth of PAHs is the first step in the pathway that leads to soot. The primary focus is on the formation of the first aromatic ring from small aliphatics.

Frenklach and coworkers proposed and developed a mechanism based on the role of acetylene as growth species[39-43]. This mechanism is known as HACA (Hydrogen-abstraction, C_2H_2 addition) and involves an even-carbon-atom pathway for benzene ring formation:

$$n\text{-}C_4H_3 + C_2H_2 \rightarrow \text{phenyl}$$
$$n\text{-}C_4H_5 + C_2H_2 \rightarrow \text{benzene} + H$$

The reaction of the n-C_4H_5 is similar to the one who had been proposed also by Cole et al.[44] for aliphatic fuels, the only difference being the simultaneous cyclization and hydrogen loss.

Colket[45] reached similar conclusions, suggesting that acetylene addition to n-C_4H_3 is the major pathway leading to cyclic compounds[46] (Figure 4.2).

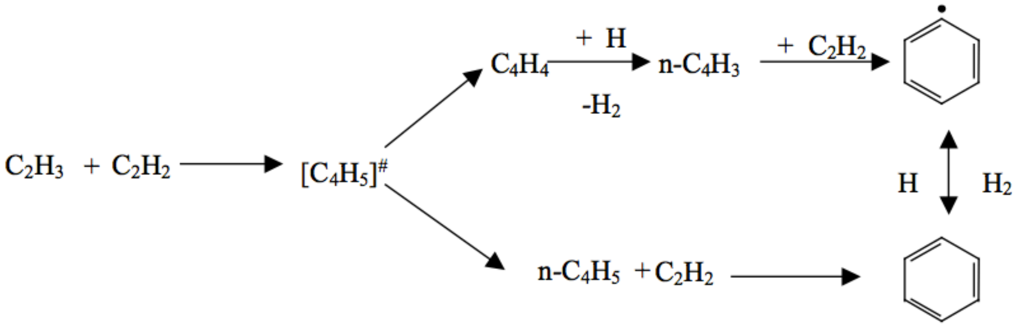

Figure 4.2: Mechanism for benzene formation via n-C_4H_5 according to Frenklach et al.

Miller and Melius[47] proved that this pathway alone is not able to account for the benzene formed and showed that, as Fahr and Stein[48] had suggested, in flames the first aromatic ring is mostly likely formed *via* an odd-carbon-atom pathway that consists in the combination of propargyl radicals (Figure 4.3).

$$C_3H_3 + C_3H_3 \rightarrow \text{benzene or phenyl} + H$$

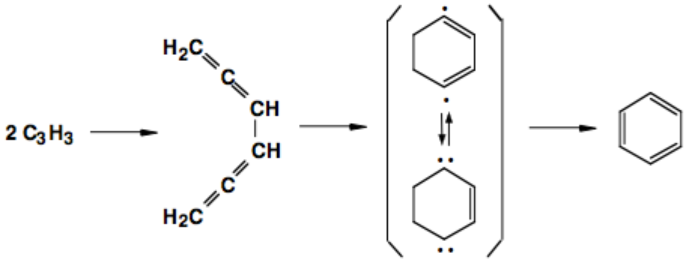

Figure 4.3: Formation of a benzenic ring from C_3H_3.

Indeed, the propargyl radical is resonantly stabilized and therefore very stable, thus its concentration in the system can be quite high.

Marinov[49] and coworkers recognized the importance of all the resonantly stabilized radicals and not only propargyl. In particular they confirmed the importance of the reaction between cyclopentadienyl radicals:

$$C_5H_5 + CH_3 \rightarrow \text{benzene} + H + H$$

$$C_5H_5 + C_5H_5 \rightarrow \text{naphthalene} + H + H$$

D'Anna and Violi[50] confirmed the importance of resonantly stabilized radicals, in particular in an oxidizing environment that enhances their formation, because they observed that the HACA mechanism is dominant only in rich conditions.

After the first ring is formed, the molecules can grow *via* different mechanisms. The HACA mechanism involves the repetition of two steps: abstraction of a hydrogen atom from the reacting hydrocarbon by a gaseous hydrogen atom followed by the addition of a gaseous acetylene molecule to the radical site formed and this leads to the formation of larger PAHs starting from phenyl radical in case of benzene. A sequence for the growth of the benzyl radical is proposed in figure 4.4.

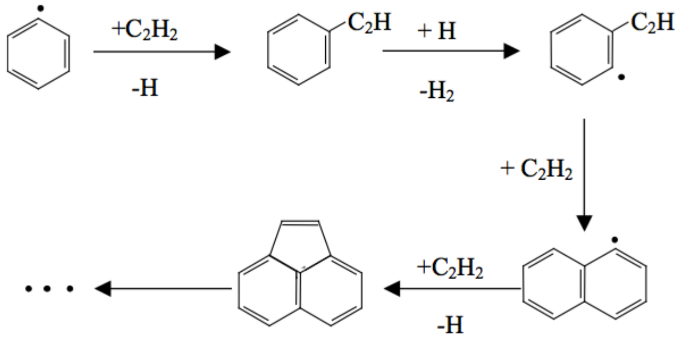

Figure 4.4: HACA sequence for the growth of PAHs[41].

The other pathway considered for the growth of aromatic species up to pyrene is the combination of resonantly stabilized radicals, like cyclopentadienyl radicals and the benzyl and propargyl radicals (Figure 4.5).

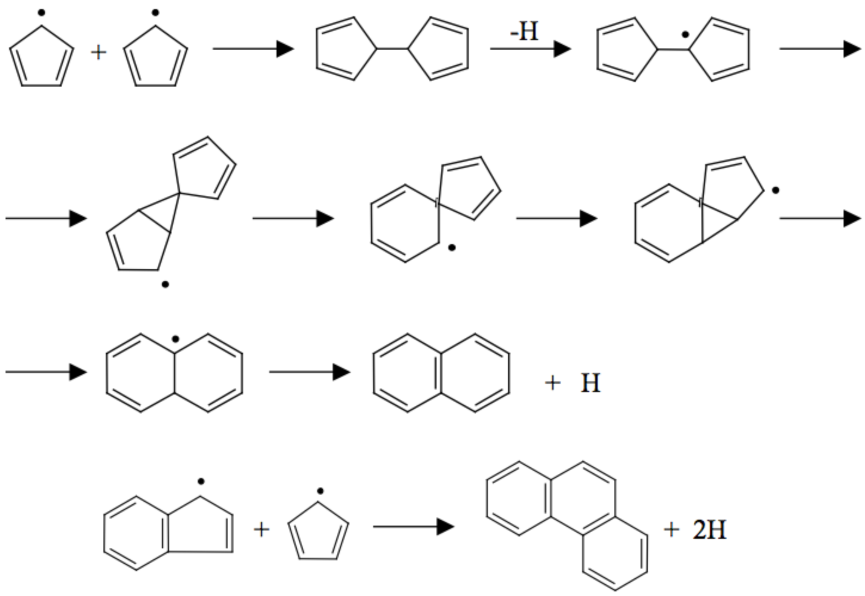

Figure 4.5: Mechanism for the formation of naphthalene and phenantrene via resonantly stabilized radicals.

The aromatic species consisting only of benzenic rings are planar and are called pericondensed aromatic hydrocarbons. Their H/C ratio decreases with increasing molecular weight. The presence of five-membered rings, instead, leads to a molecular distortion and induces a curvature in the molecule. Their active sites react with another aromatic compound or with a radical originating non-completely condensed aromatic oligomers; their H/C is constant from moderately small molecules up to bigger dimensions, as shown in figure 4.6[51].

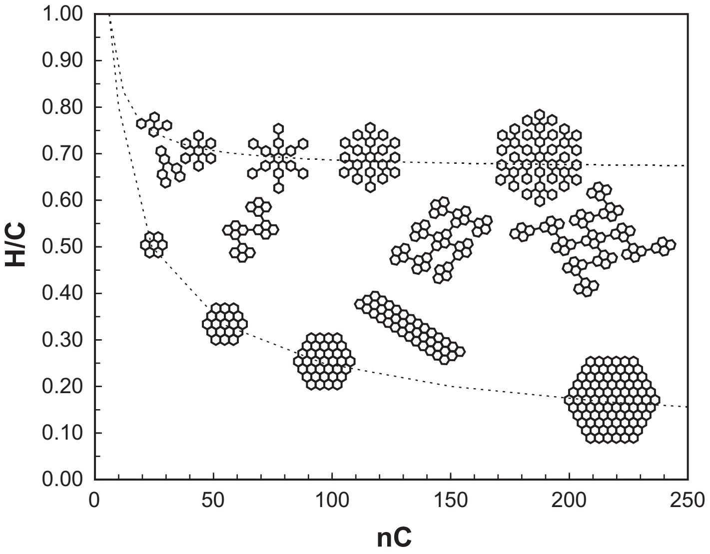

Figure 4.6: Schematic representation of the pericondensed aromatics and the oligomers of benzene[51].

4.3 SOOT FORMATION AND GROWTH

It is widely accepted that further growth of the PAHs leads to soot formation through nucleation, surface growth and coagulation. In figure 4.7 the axis on the left indicates the time scales characteristic of the different steps.

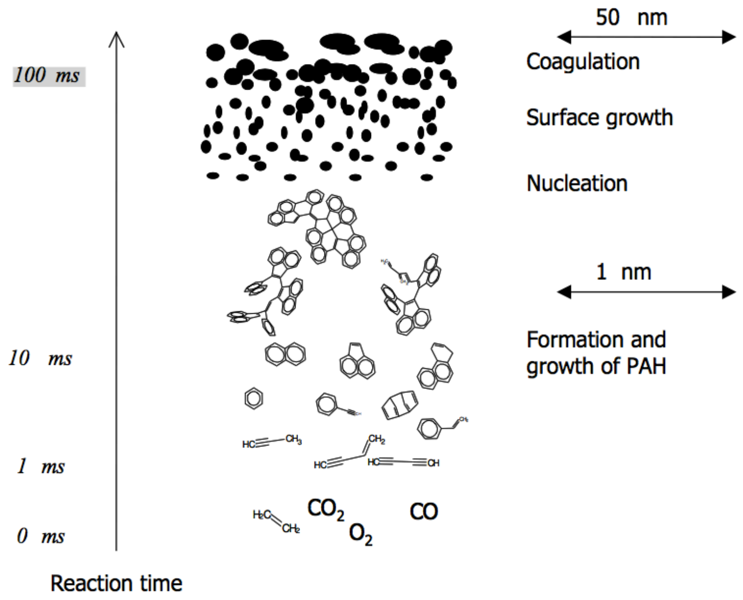

Figure 4.7: Schematic representation of the pathway that leads to soot formation[52].

4.3.1 Nucleation

Soot nucleation represents the transition of gas-phase species to solid particles and it is one of the least known parts of the process.

Initially[41], this transition was seen as a result of a purely chemical growth, with soot simply being the mass accumulated in PAH species above a certain size, but this model underestimated particle size. Nowadays, there are three different pathways that are the most discussed ones (Figure 4.8). Path A, proposed by Kroto and coworkers[53], considers the growth of two-dimensional PAHs into curved, fullerene-like structures that are the nucleus of spherical particles. These particles cannot close into a layer of carbon, but develop in successive layers. Path B, envisioned by Frenklach and coworkers and Miller et al.[43,52,54,55], represents the nucleation as physical coalescence of moderate-sized PAHs into stacked clusters[38]; whereas path C, proposed by Richter and also

Ciajolo, Violi and coworkers[56-59], consists in the reaction or chemical coalescence of PAHs into cross-linked three-dimensional structures.

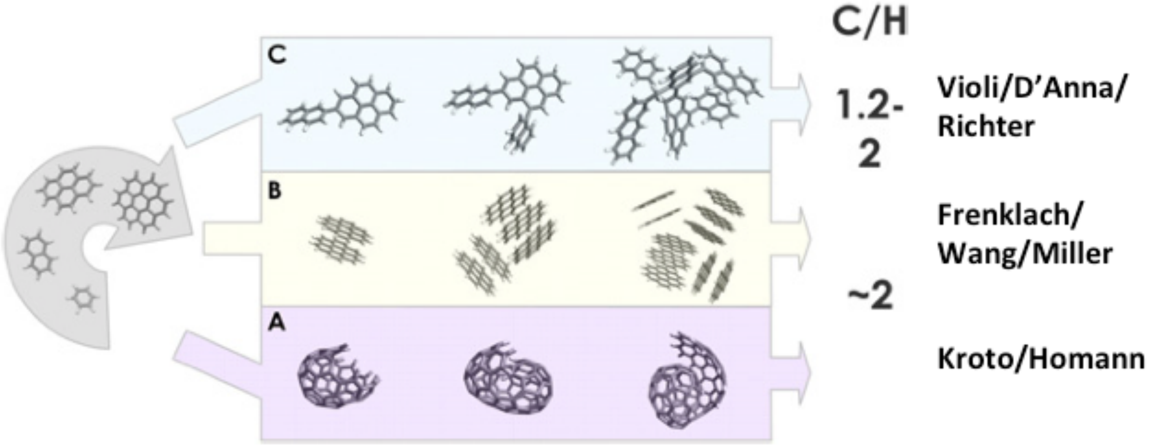

Figure 4.8: Schematic representation of the three possible pathways[38].

It is worth to notice that, as Frenklach pointed out[39], while the first pathway is substantially different, the other two might be considered as two extreme regimes of the same mechanism. In fact, path B is better in high-temperature combustion, when the chemical growth is limited by a high degree of reaction reversibility, while path C becomes predominant when the formation of chemical bonds is not counterbalanced heavily by fragmentation.

The fullerenic growth is too slow to explain the time scale of the soot inception phenomena, considering also the concentrations of the PAHs with growing number of rings.

PAH dimerization as the initial nucleation step (paths B and C) is supported by experimental evidence that shows a bimodality of particle size distribution functions of nascent soot particle in premixed flames and well stirred or plug flow reactors[26,60-68]. In fact, a mechanism based on dimerization has a second-order kinetics in monomer concentration, consistent with a bimodal distribution that indicates a persistent nucleation parallel to the growth process of the particles already formed.

A theoretical study on PAHs dimerization as in path B[55] has proposed electrostatic and dispersive forces as driving force for binding even at flame temperatures. In particular, studies on pyrene dimerization[54,69] demonstrated that this reaction is physically realistic inside the flames and that dimers' lifetime is compatible with soot formation time scale. However, further research has to be conducted to understand if a dimer would survive all the non-reactive collisions that happen during its lifetime before it reacts.

For path C the presence of aliphatic groups joint with aromatic structures has been hypothesized. This conformation is explained through reactions of aromatic molecules with an aryl radical[56-59], but the mechanism cannot explain the persistent nucleation in the post flame zone, where H concentration drops drastically and cannot initiate these reactions.

4.3.2 Surface growth

The formed particles' nuclei acquire mass by means of surface growth induced by acetylene addition, by reactions with small resonant radicals or aromatic radicals. In fact, if nucleation controls the number of particles, the growth determines their mass instead.

Surface growth consists in reactions that occur on the surface of the particles. It is thought that soot growth mechanisms are similar to the ones for PAHs[39,70] and that involve mainly surface acetylene, small resonant radicals and aromatic radicals reactions. Their contribution depends on the reaction conditions[71] and the fuel. The main difference between the mechanism for PAHs and soot is that in the latter the reactions are not in gas phase, but they are heterogeneous reactions between a solid and a gas. As mentioned earlier, however, in the kinetic scheme developed in Politecnico di Milano there is the hypothesis of chemical similarity, which means that chemical reactions on particles' surface are treated in analogy to the ones involving gas-phase PAHs and the reactions' kinetics is modified to take into account the heterogeneity of the system on the basis of aerosol dynamics. This allows to define the specific physical nature of the active sites in generic terms and to describe the growth, but also the oxidation, in terms of elementary chemical reactions[39].

In fact, the HACA mechanism is activated by hydrogen atoms (H•) that by extracting a hydrogen bonded to the surface form radicals that can thus react with gaseous species and grow.

Surface growth reaction rate is directly proportional to the concentration of hydrogen atoms.

Experimental evidence shows that soot mass continues to increase even in the post-oxidative region of the flame, where H• concentration is very small. This led to the hypothesis that there are persistent free radicals on soot surface and the theory has been confirmed by experimental measurements of the concentration of anthracite's free radicals[72] and of free aromatic radicals from ethylene and acetylene pyrolysis[73].

Despite the similarity hypothesis there are some substantial differences with respect to the gas phase reactions in the definition of the active sites. In fact, in surface reactions the kinetics depends on the collision frequency while the sticking coefficient and the equilibrium constant might depend on the nature of the surrounding sites. The reaction rate decreases with increasing particles' dimensions, because the H/C ratio decreases and that means that less active sites are available. Furthermore, bigger particles have a lower surface per volume unit and surface reactions become of secondary importance.
Bigger particles are indeed subject to physical rather than chemical interactions.

4.3.3 Coagulation

The coagulation implies a further increase in particles' dimensions due to collisions between growing soot particles and controls the final particles size. Usually this phenomenon involves relatively small particles with high growth rates. Surface growth continues after the particles coagulate leading to the structure represented in figure 4.9, where the fine particles constitute the inner core and PAHs form the outer shell.

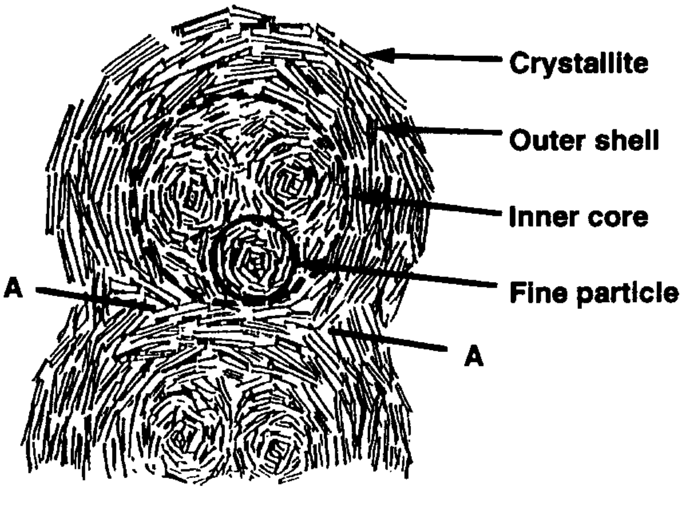

Figure 4.9: Schematic model of particles' coagulation in soot from Diesel fuel[74].

The rate of reaction of this process can be calculated with the Smoluchowski formula[75]. For this calculation the particles are considered as spherical and small with respect to the gas mean free path and it is assumed that every collision results in a coagulation. Small particles or low-density gas verify this assumption. In particular this is valid in low-pressure flames[76,77], in free molecular regime.

It is possible to distinguish two different types of coagulation: coalescence and agglomeration. Coalescence happens when a gas-phase molecule or a small particle collides against another particle to form a structure that, to minimize the free energy, tends to reduce its surface[51].

This means that smaller particles or gas-phase species are incorporated inside a bigger particle. The sphericity is maintained also because surface reactions act on these structures "smoothing" the surface[38] (Figure 4.10).

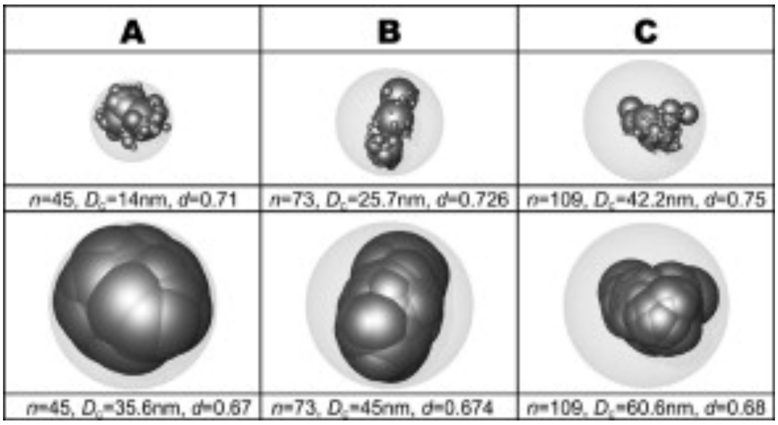

Figure 4.10: Nascent, primary soot particles simulated with a kinetic Monte Carlo procedure[78]. Upper panel: particle structure after coagulation of single soot nuclei. Bottom panel: particle structure after a period of surface growth.

When bigger particles collide the interacting species maintain their own structure and aggregate into chain-like fractal structures[39,46]. This is because particles are more graphitic, rigid, the coalescence is not effective anymore and the surface growth is too slow to smooth and reshape the structure into a spheroidal form, also because in this phase soot particles are about 20 nm in diameter, therefore a massive growth would be needed to fill in the gaps. The whole growth process is summarized in figure 4.11.

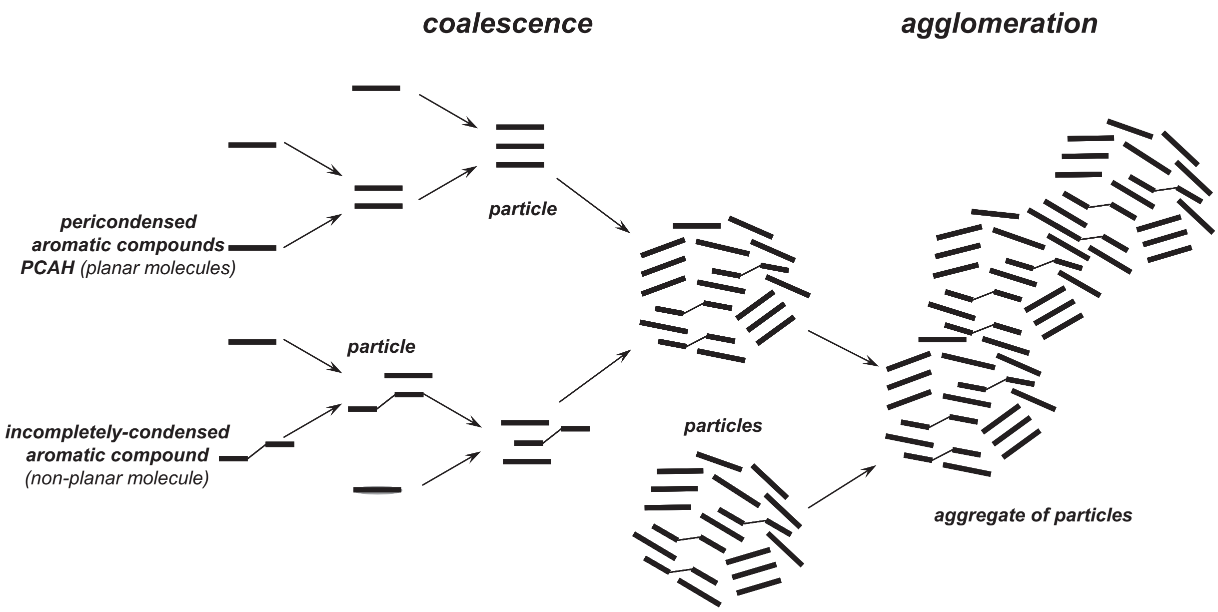

Figure 4.11: Scheme of the nucleation and coagulation processes[51].

4.3.4 Oxidation

Soot formation and growth processes are in competition with soot depletion due to oxidation reactions. These mechanisms are poorly understood and the models' predictive capabilities are way smaller than for the previous ones. Oxidation consists in particles' mass removal due to chemical reactions at the surface[79]. A particular case is the oxidation-induced fragmentation[80], in which oxygen penetrates into the particles and by removal of carbon atoms weakens the structure until it eventually breaks up, forming smaller particles. Only recently mechanisms that include both oxidation and oxidation-induced fragmentation have been developed[79,81].

The main species responsible for the oxidation are atoms, radicals and molecules mainly made of oxygen, like OH, O, O_2 but also NO.

The dominant radical is OH, even though it has been measured that the collision efficiencies of radical oxygen are similar[82], because OH concentration is far higher. During the oxidation carbon monoxide is formed.

On the contrary, it is supposed that only oxygen participates in fragmentation, because OH reactivity is too high, therefore it cannot penetrate into particles but gets depleted near to the surface before reaching the core, whereas oxygen diffusion inside the particles' pores is in a reaction limited regime[81].

4.4 APPROACHES TO MODELING

As explained in the previous chapter, the gas and solid phase kinetics of the system must be coupled with transport equations. However, it is not possible to write an equation for every species, since particles' dimension, molecular weight and chemical composition span over a wide range. For this reason an accurate description of soot is also numerically very complex and demanding in terms of computational cost.

Three main parameters are considered to describe soot: soot volume fraction, number density and particle size distribution.

The soot volume fraction (f_v) is defined as the ratio between soot volume and the total volume:

$$f_v = \frac{V_{soot}}{V_{total}}$$

The number density ($[n]_{soot}$) is the ratio between the number of soot particles and the total volume and might be related to soot concentration (c_{soot}) through Avogadro's number (N_A):

$$[n]_{soot} = \frac{n_{soot}}{V_{total}} = N_A \, c_{soot}$$

The particle size distribution (PSD) defines the relative amount, typically by diameter, of particles present according to size.

These three properties give the information on how much soot is formed, its concentration and how the mass is distributed among the different sizes.

To face this problem different approaches to modeling are used. The historically most significant ones are the method of moments[83] and the discrete sectional method[70,84]. Later also the Galerkin method[85] has been implemented. Recently some efforts have been made to add chemical resolution, chemical composition, size distribution and morphology to nascent soot particles, for example using Monte Carlo methods[86].

4.4.1 Methods of moments

The method of moments is based on a statistical approach. In fact, to overcome the impossibility of writing equations for all the species, a transport equation is used:

$$\frac{\partial f(\xi)}{\partial t} + \frac{\partial}{\partial x_i}\left(u_i\, f(\xi)\right) - \frac{\partial}{\partial x_i} D_x \left(\frac{\partial\, f(\xi)}{\partial x_i}\right) = S_\xi(\xi)$$

This expression describes the soot evolution in time through a population balance equation (PBE). In this case the x is the external coordinate; ξ, the internal coordinate, is the soot particle diameter and the function f that describes it is the particle size distribution function (PSDF). The transport equation expresses therefore a balance on the particles' number.

The source term, $S_\xi(\xi)$, is in general an implicit and complex function of moments and accounts for all the phenomena that modifies the PSDF, like nucleation, molecular growth, aggregation and oxidation. Particles' dynamics is thus expressed through the moments of the particle size distribution function (PSDF).

To solve the system numerically it is necessary to discretize not only time and space, but also the distribution function itself.

In fact, a distribution is identified by an infinite number of moments, but to make the problem solvable it is simplified by describing it through a finite number of moments.

If the PSDF shape is known then two moments are sufficient. The moment about zero, m_0, is the area of the distribution and represents the number of soot particles, while the third moment, m_3, is the soot volume fraction. A transport equation is written for each of these properties, and the source term for m_0 depends only on the mechanisms modifying the number of particles, like nucleation, coagulation, aggregation and fragmentation, while the source term for m_3 accounts for nucleation, growth and oxidation, that change the soot volume fraction.

The source term is then expressed through pseudo-reactions, but the exact evaluation of this term is numerically and experimentally very complex, therefore approximations, called closure moments, are needed.

One of the simplest closure methods is the MOMIC (method of moments with interpolative closure)[83], which allows to solve the system with a low number of equations.

Successive methods, like the quadrature method of moments (QMOM)[87] allow not to impose the distribution form *a priori*.

4.4.2 Galerkin methods

A discrete Galerkin method had been formulated by Wulkow[88] for polymerization reactions. Applied to soot modeling, the algorithm describes the dynamics of particles of specific sizes in a Lagrangian coordinate[85].

Polynomial functions in one discrete variable are used for the expansion of the particle size distribution function. These polynomials are built on the basis of a weight function, defined depending on the chemical process to be modeled.

The weight function is known, hence it is possible to calculate its moment about zero without assuming its form.

The distribution function might be expressed as:

$$P_s^{(\infty)}(t) = \psi(s;\varrho) \sum_{k=0}^{\infty} a_k(t;\varrho)\, l_k(s;\varrho)$$

Where $\psi(s;\varrho)$ is the weight function expressed, for example, through the Schulz-Flory distribution; $l_k(s;\varrho)$ are the polynomials associated to the weight functions and $a_k(t;\varrho)$ are the coefficients that take in account time dependence. ϱ is the parameter used to optimize the representation[89].

4.4.3 Monte Carlo methods

The Monte Carlo is a statistical method used to determine the PSDF. The distribution function is described through a stochastic process which is computationally very demanding, therefore its application is limited to simple configurations, like homogeneous reactors or laminar premixed one-dimensional flames. In some methods the simulations describe particles' trajectories based on Langevin equation, while in Direct Simulation Monte Carlo the system is considered as a stochastic statistical ensemble of events, each associated to a given probability.

4.4.4 Discrete sectional methods

In the discrete sectional methods particles are discretized in classes of pseudo-species, called BINs in our model. Each of the classes is defined by the average molecular mass and a given number of carbon and hydrogen atoms. BINs' kinetics is defined in analogy with the gas phase one, the two phases are coupled and both written in the common form A + B → C + D, with the usual Arrhenius form to describe formation and growth rates.

A transport equation is written for each of the classes. This method has a very high computational cost, but it is accurate if an appropriate number of classes is chosen.

The discrete sectional method is the one used for in the model developed by the CRECK Modeling group in Politecnico di Milano and it is used for all the simulations. A comparison with the model used by D'Anna's group in Università degli studi di Napoli, based on the same approach, is here proposed.

4.5 DISCRETE SECTIONAL METHOD USED IN POLITECNICO DI MILANO

As the number of carbon atoms in a molecule increases, the number of isomers and species with similar mass increases enormously, until it becomes impossible to describe each of them with a detailed model. This is especially true for the particles, because the chemical composition and the precise structure are not even known. The discrete sectional method overcomes the issue by using lumping techniques, that means dividing them into lumped pseudo-species, called BINs, that span over a certain mass range and have a given average molecular weight and an assigned number of carbon and hydrogen atoms.

In the model under exam classes with same mass and different hydrogenation are considered to follow better the chemical evolution of the system, especially to describe in a more flexible way condensation and dehydrogenation reactions.

All of the species starting from polycyclic aromatic hydrocarbons with 20 carbon atoms are divided into BINs, each represented by 2 or 3 reference species with different H/C ratios.

The peculiar characteristic of the discrete sectional method is the analogy between gas and particles' phase, which are directly coupled and written in the usual form A + B → C + D.

The kinetics is therefore described by the modified Arrhenius and hence, from a computational point of view, the introduction of the solid particulate consists only in the addition of the new species, the BINs, with the corresponding reactions and transport equations.

The following table summarizes the characteristics of the BINs included in the model.

BIN	Mass	nC	Mean Diameter		H/C	
	[amu]		[nm]	A	B	C
1	≈ 250	20	0.76	0.8	0.5	0.3
2	≈ 500	40	0.96	0.8	0.5	0.3
3	≈ 1000	80	1.21	0.75	0.45	0.3
4	≈ 2000	160	1.52	0.7	0.4	0.2
BIN	Mass	nC	Mean Diameter		H/C	
	[amu]		[nm]	A	B	C
5	≈ 4000	320	1.91	0.65	0.35	0.2
6	≈ 8000	640	2.41	0.6	0.35	0.15
7	≈ 15500	1250	3.01	0.55	0.3	0.1
8	≈ 30000	2500	3.78	0.5	0.25	0.1
9	≈ 61000	5000	4.76	0.45	0.2	0.1
10	≈ 121000	10000	5.99	0.4	0.15	0.1
11	≈ 245000	20000	7.55	0.35	0.1	-
12	≈ 490000	40000	9.52	0.35	0.1	-
13	≈ 970000	80000	11.98	0.30	0.1	-
14	≈ 1950000	160000	15.10	0.30	0.1	-
15	≈ 3900000	320000	19.01	0.25	0.1	-
16	≈ 78000000	640000	23.92	0.20	0.05	-
17	≈ 15100000	1250000	29.90	0.20	0.05	-
18	≈ 30200000	2500000	37.67	0.20	0.05	-
19	≈ 60200000	5000000	47.46	0.20	0.05	-
20	≈ 121000000	10000000	59.80	0.20	0.05	-

Table 4.1: Definition of the BINs

As shown in the table, large PAHs and soot are divided into 20 classes of pseudo-species. The first BIN is a molecule with 20 carbon atoms and an average molecular mass of 250 amu (atomic mass unit). Each class has a number of carbon atoms double than the previous one; therefore BIN2 for example has 40 carbon atoms and an average mass of 500 amu. The largest BIN is the BIN20, with 1×10^7 carbon atoms and a mass of about 1.21×10^8 amu. Diameters have been determined under the assumption of spherical form and a density of 1.8 g/cm^3. The next step is to change it to 1.5 g/cm^3, a more suitable value for nascent soot particles, as measured also by Maricq and coworkers[90], or to assign a different density from 1.5 to 1.8 g/cm^3 to each BIN class depending on the particle size.

BINs from 1 to 4 are still considered as large PAHs while the first soot particle corresponds to BIN5, with 320 carbon atoms. The threshold has been determined based on observation of species containing around 160 carbon atoms extracted from condensed material produced in flame[91] and it is consistent with measurements of particles in the flame[66,92,93].

Hydrogenation decreases with increasing molecular mass, both due to the growing number of condensed rings and to the increase in curvature induced by the presence of five-membered rings. Curvature is expected to influence in a great extent properties of soot material, therefore the importance of its correct assessment in model predictions is significant.

Three H/C ratios are considered for each class until BIN10, whereas for BINs from 11 to 20 only two different hydrogenation levels are involved. This seems to be more consistent with experimental data[94], showing that above a certain number of carbon atoms the hydrogenation level becomes almost constant and inside a certain range.

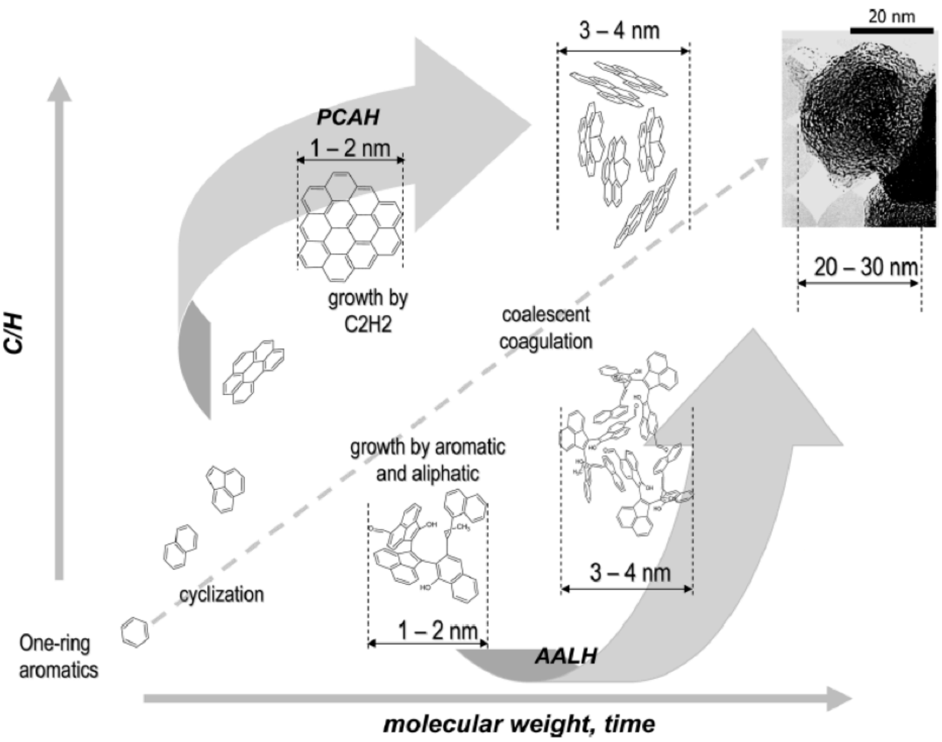

Figure 4.12: Trend of the hydrogenation level in soot particles with increasing molecular weight (and therefore residence time). PCAH: peri-condensed aromatic hydrocarbons. AALH: aromatic-aliphatic-linked hydrocarbons[94,95].

Figure 4.12 shows the change in hydrogenation due to the increasing number of condensed rings, while figure 4.13 illustrates the correspondence between the curvature and the H/C ratio.

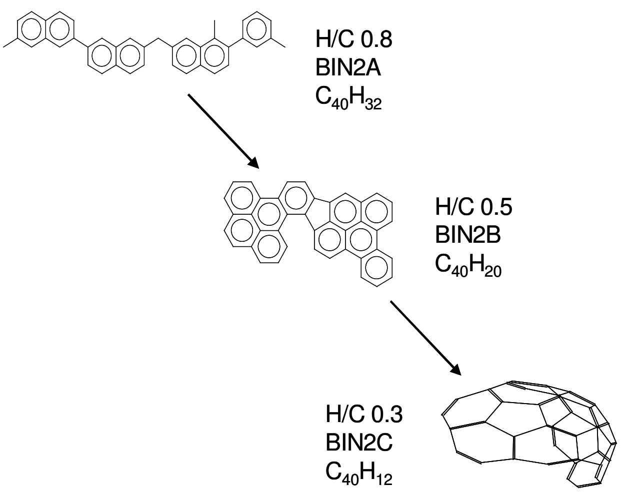

Figure 4.13: Structures of BIN2 corresponding to different hydrogenation levels[96].

Figure 4.14 represents the hydrogenation trend with respect to the average molecular mass of each class.

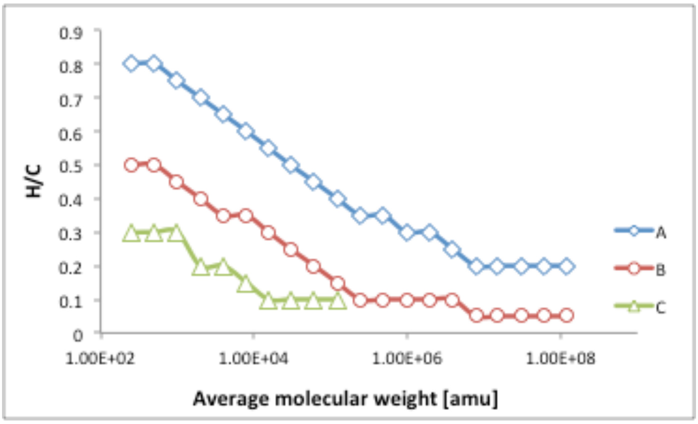

Figure 4.14: Graphic visualization of the H/C ratio trend in our model. A, B, C are the different hydrogenation levels possible for each BIN class.

For each BIN molecular species there is a corresponding radical BIN*.

Obviously, a particular approach has to be adopted to respect the stoichiometry in the reactions involving BINs, since not all of the possible species are present in the model.

The explanation of this approach will be given through the example of the acetylene addition to the radical BIN1A* ($C_{20}H_{15}$).

Formally, the real stoichiometry of the reaction would be:

$$C_2H_2 + BIN1A^* \rightarrow H + C_{22}H_{16}$$

The species with 22 carbon atoms is not contained in the kinetic scheme, hence a lever rule is applied to “split” the product between adjacent BINs (Figure 4.15).

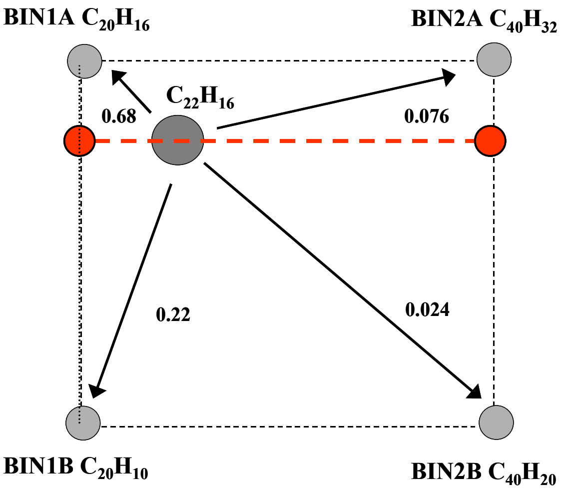

Figure 4.15: Splitting of $C_{22}H_{16}$ into the four adjacent BINs pseudospecies[96].

First the carbon atoms are split between the classes BIN1 and BIN2, then the hydrogen atoms are split between the different hydrogenation levels.

The resulting stoichiometry is the following:

$$C_2H_2 + BIN1A^* \rightarrow H + 0.68\ BIN1A + 0.22\ BIN1B + 0.076\ BIN2A + 0.024\ BIN2B$$

The program performs the splitting automatically in a similar way for all of the reactions involving BINs. The atomic balance is closed, H and C atoms are preserved and the sum of the coefficients of the produced BINs is equal to 1 because physically only one particle is formed during the reactions of superficial growth.

Soot formation, growth and oxidation are described through a detailed kinetic model coupled with the gas phase. As mentioned earlier, soot reactions are developed in analogy with the ones for PAHs. Once defined the kinetic rates, the source program automatically generates reactions. The reaction classes here presented are the detailed reconstruction of the general kinetic pathway presented in paragraphs 4.2 and 4.3. For each of the reaction classes a plot with the comparison between the values proposed by D'Anna[81] and ours will be presented. The values refer to A-type BINs.

The units of measure used for the kinetic constants are mol, l, K, cal.

4.5.1 Reactions of aromatics formation and growth

These reactions occur in the gas phase and include the formation of the first aromatic ring and the subsequent growth.

The link with the soot kinetic model is based on the evaluation of the kinetic constants in gas phase considered significant, which are used as reference.

Their value is taken from literature and adapted by means of tuning, as explained in paragraph 2.1, Chapter 2. Soot kinetics is then built from these values through a rescaling and correction procedure that takes into account the heterogeneity of the system. The parameters are adapted using aerosol dynamics theory and experimental evidences

4.5.2 Metathesis reactions

Metathesis reactions involve hydrogen abstraction. They are fundamental for the activation of the process since they contribute to radical species' formation. H and OH radicals play a primary role, but there are also secondary radicals like O, CH_3 and the reactions with O_2.

The kinetic constants, as explained in paragraph 2.4, Chapter 2, depend both on the abstracting radical and the type of hydrogen extracted.

The kinetic rate scales with the number of H atom, as already proposed by Ranzi et al.[14] and confirmed by Violi and coworkers[97] for species with 5 or 6 membered rings.

$$H + PAH_{m,n} \leftrightarrow H_2 + PAH^*_{m,n-1} \qquad k_{ref} = 0.32\ 10^{11} \exp(-14000/RT)$$

$$OH + PAH_{m,n} \leftrightarrow H_2O + PAH^*_{m,n-1} \qquad k_{ref} = 0.59\ 10^{10} \exp(-5000/RT)$$

An analogy between the reactive sites of PAHs and those of particles is assumed. All the molecular BINs are activated by H-abstraction reactions or unimolecular reactions with hydrogen loss (Figure 4.16).

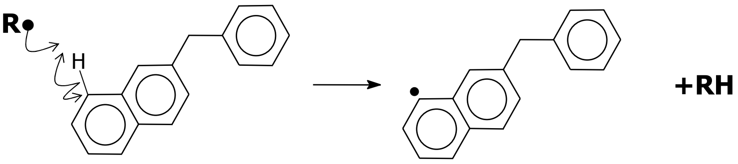

Figure 4.16: Metathesis reaction for aromatic species.

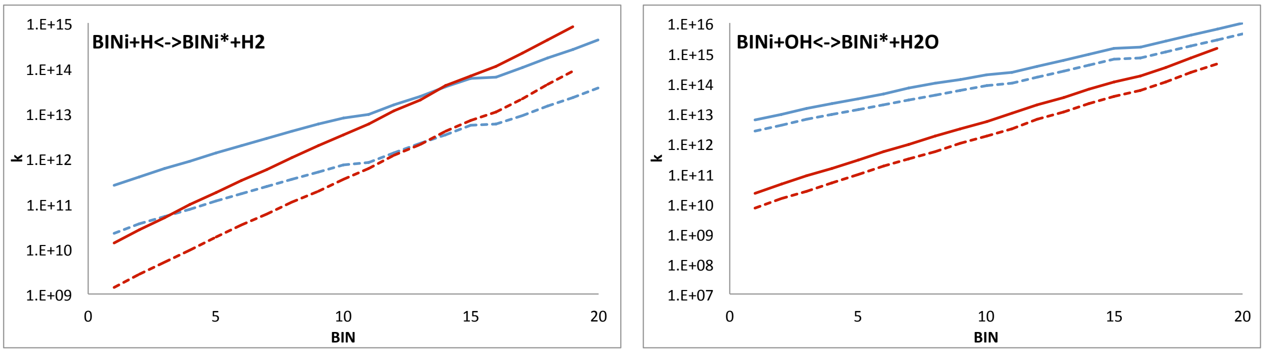

Figure 4.17: Comparison of the kinetic constants for metathesis reactions in our model (red lines) and D'Anna's model (light blue line). Solid lines: 1800 K, dashed lines: 1200 K.

4.5.3 Unimolecular H loss

For this class the reference is the reaction involving benzene:

$$C_6H_6 \rightarrow C_6H_5 + H \qquad k_{ref} = 1.5\ 10^{17}\ \exp(-114000/RT)$$

The reaction constant is determined by multiplying the reference constant by the ratio between the hydrogen number of the considered species (nH) and the benzene's one ($n_{C6H6} = 6$)

$$k = k_{ref}\ (nH/6)$$

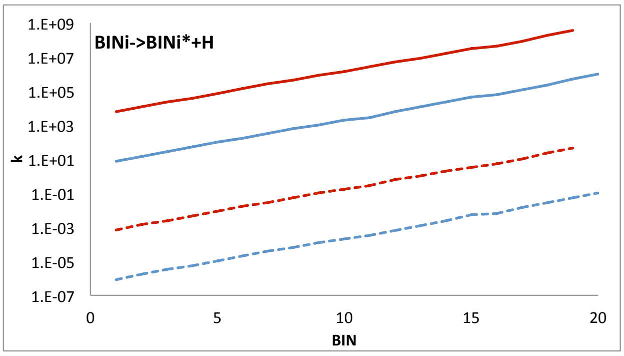

Figure 4.18: Comparison of the kinetic constants for unimolecular H loss in our model (red lines) and D'Anna's model (light blue line). Solid lines: 1800 K, dashed lines: 1200 K.

4.5.4 Dehydrogenation reactions

Dehydrogenation reactions involve both molecular and radical species and produce H or H_2, respectively (Figure 4.19).

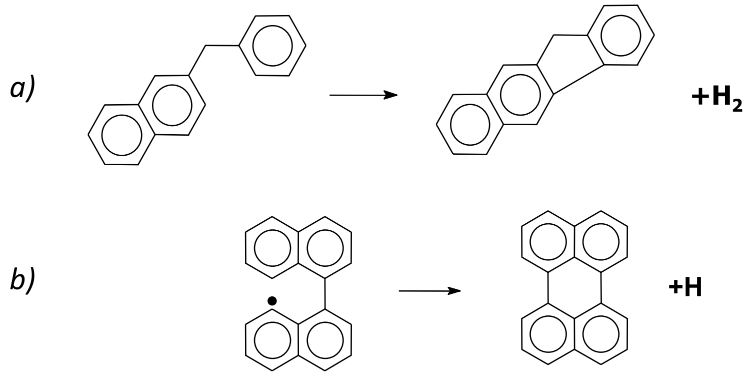

Figure 4.19: Dehydrogenation and subsequent cyclization of aromatic molecules (figure *a*) and radicals (figure *b*).

As the hydrogenation level decreases, the cyclization is fostered. The BINs of the class with the lowest H/C ratio are not involved in dehydrogenation reactions.

For the dehydrogenation of radical BINs with H production the reference is the constant proposed by Richter[70] for the reaction that leads to fluorene production from the benzyl benzene radical:

$C_{13}H_{11} \rightarrow C_{13}H_{10} + H$ $k_{ref} = 1.0\ 10^{11} \exp(-12000/RT)$

For BINs reactions the pre-exponential factor (A) is corrected in function of the H/C, H/C_{ref} and H/C_{lim} ratios, the number of carbon atoms (nC) and the spherical diameter (σ), where $H/C_{ref}=11/13$ and $H/C_{lim} = 0.05 + 1/(nC^{0.25})$.

$$A = A_{ref} \frac{\frac{H}{C}}{\left(\frac{H}{C}\right)_{ref}} \sigma \left(\frac{H}{C} - \left(\frac{H}{C}\right)_{lim}\right)$$

Dehydrogenation reactions of BINs molecules and radicals with H_2 production make reference to the reaction diphenylmethane to give fluorine proposed by Colket and Seery[98]. Radicals' reactions involve only particles; hence they are considered only for BIN5 and following.

$C_{13}H_{12} \rightarrow C_{13}H_{10} + H_2$ $k_{ref} = 1.0\ 10^8 \exp(-32000/RT)$

The pre-exponential factor (A) is corrected in function of the number of hydrogen (nH) and carbon (nC) atoms, the H/C and H/C$_{lim}$ ratios, where H/C$_{lim}$ = 0.05 + 1/(nC$^{0.25}$).

$$A = A_{ref}\ nH \left(\frac{H}{C} - \left(\frac{H}{C}\right)_{lim}\right)$$

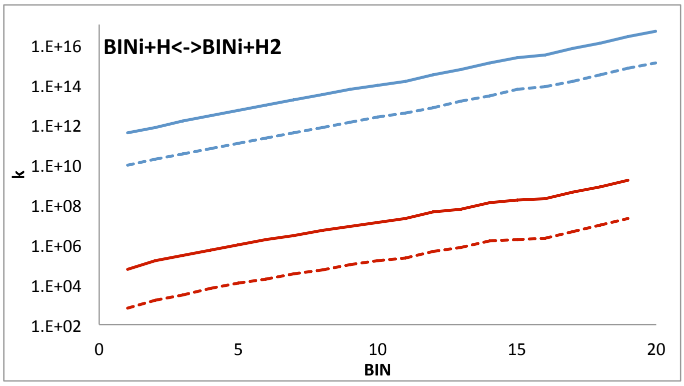

Figure 4.20: Comparison of the kinetic constants for dehydrogenation of molecular BINs in our model (red lines) and D'Anna's model (light blue line). Solid lines: 1800 K, dashed lines: 1200 K.

4.5.5 Nucleation reactions

Nucleation is described by all of the reactions involving PAHs, molecular or radical, reacting with other PAHs. The molecular weight increases leading to the formation of the first solid particle, considered to be BIN5 in the model developed at Politecnico di Milano.

Three kinds of reactions are possible: between two radicals, a molecule and a radical or two radicals.

In the first case the reference reaction is the recombination of two cyclopentadiene radicals to produce naphthalene.

$C_5H_5 + C_5H_5 \rightarrow C_{10}H_8 + 2H$ $k_{ref} = 1.0\ 10^9 \exp(-6000/RT)$

For BINs, the pre-exponential factor is multiplied by a scaling factor, defined as the ratio between the frequency factor of the reaction under exam and the frequency factor of the reference reaction (scalingfactor = $C_f/C_{f,ref}$):

$$A = A_{ref} \text{ scaling factor}$$

The frequency factor is derived from the aerosol dynamics and calculated in function of Avogadro's Number (N_A), of the diameter ($\sigma = (d_A + d_B)/2$, where d_A and d_B are the diameters of the reacting particles), of the universal gas constant (R), of the temperature (T) and of the reduced mass ($\mu = (m_A\, m_B)/(m_A + m_B)$):

$$C_f = N_A \sigma^2 \sqrt{\frac{8\pi RT}{\mu}} 10^3 \qquad \left[\frac{l}{mol\ s}\right]$$

The activation energy, instead, depends on the structure of the reacting radicals. It is therefore necessary to distinguish between resonantly stabilized radicals and non-stabilized radicals.
In case of non-resonant radicals the activation energy is zero, whereas it increases to 3000 kcal/kmol in case of one resonant radical and to 6000 kcal/kmol if both the reacting radicals are resonant.

For the reactions between a radical and a molecule the reference is C_8H_6 reacting with a non-resonant radical C_6H_5 or a resonant radical C_7H_7:

$C_6H_5 + C_8H_6 \rightarrow C_{14}H_{10} + H$ $\qquad k_{ref} = 1.0\ 10^9 \exp(-8000/RT)$

$C_7H_7 + C_8H_6 \rightarrow C_{14}H_{10} + CH_3$ $\qquad k_{ref} = 1.0\ 10^9 \exp(-19000/RT)$

Also in this case the reaction is corrected through the scaling factor based on the collisional factor, when it involves particles.
The reference value for the reaction between two molecules is the one proposed by D'Anna and D'Alessio:

PAH + PAH → aBIN1 + bBIN2 $\qquad k_{ref} = 1.0\ 10^6\ T^{0.5}$

Where a and b are the stoichiometric coefficients.

In figure 4.21 the different reactions are schematized. Figure *a* shows the reference reaction for radical recombination; cyclopentadienil radicals form a peri-condensed structure, the naphthalene. In figures *b* and *c* two reactions between a molecule and a radical are represented and the hydrocarbons formed are aromatic-aliphatic linked, therefore with a higher hydrogenation level with respect to a peri-condensed structure.

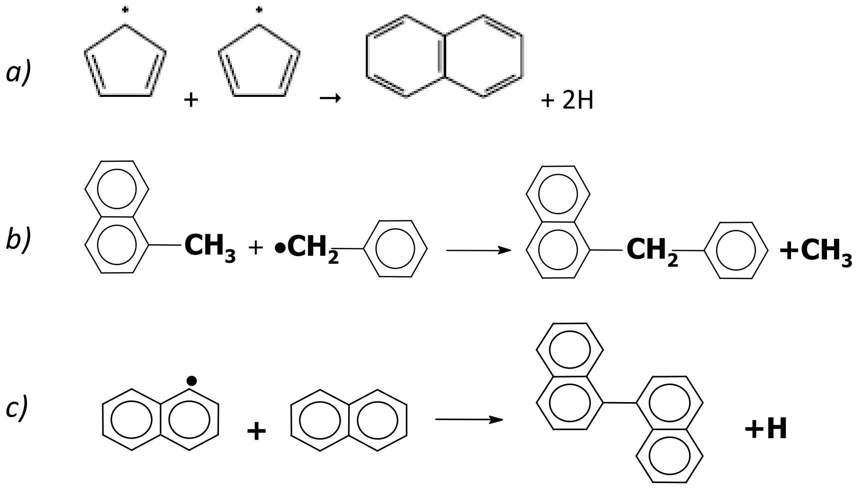

Figure 4.21: Nucleation through recombination of aromatic radicals (figure *a*) or a radical and a molecule (figure *b*).

4.5.6 Superficial growth reactions

The growth of soot particles occurs *via* gas-solid phase reactions. The main gaseous species involved are acetylene, aromatic species and resonance-stabilized radicals like C_3H_3, C_4H_3, C_4H_5P and cy-C_5H_5.

Acetylene addition occurs according to the HACA mechanism. The kinetic parameters used are the same as those of C_2H_2 addition on aromatics. The reaction constants are based on the reaction of acetylene addition on naphthalene radical, as shown also in figure 4.22:

$$C_2H_2 + C_{10}H_7 \rightarrow C_{12}H_8 + H \qquad k_{ref} = 1.0\ 10^9 \exp(-5000/RT)$$

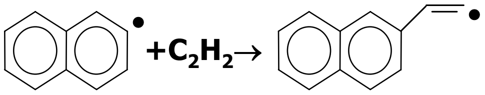

Figure 4.22: Addition of acetylene on naphthalene radical.

In our model two different HACA reactions are distinguished: in the first type the reacting BIN* radical is dehydrogenated, while in the second one it is not.

Reaction rates are scaled by means of a collisional frequency factor (γ) that multiplies the asymptotic value calculated for BIN20 and equal to 1.0 10^{11} exp(-5000/RT). The collisional efficiency is a function of the equivalent spherical diameter (σ) expressed in nanometers:

$$\gamma = \frac{1+\sigma^3}{100+\sigma^3}$$

To compare our value with the one used in the kinetic model developed by D'Anna and coworkers the kinetic constants for both the HACA mechanisms are summed, since they consider only one type of HACA.

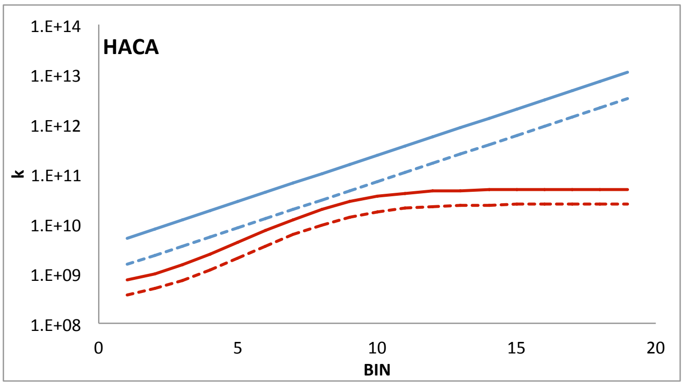

Figure 4.23: Comparison of the kinetic constants for HACA mechanism in our model (red lines) and D'Anna's model (light blue line). Solid lines: 1800 K, dashed lines: 1200 K.

Other surface growth reactions involving PAHs are present in the kinetic scheme. It is assumed that reactions between molecular BINs and PAHs are slow and therefore neglectable[99].

The reactions involving radical BINs and molecular PAHs or molecular BINs and radical PAHs have as reference the reaction of C_8H_6 with the non-resonant radical C_6H_5 (k_{ref} = 1.0 10^9 exp(-6000/RT)) or with the resonant radical C_7H_7 (k_{ref} = 1.0 10^9 exp(-19000/RT)), analogously to the nucleation reactions.

For BINs' classes from 1 to 5 the kinetic constants are calculated starting from the values of the reference reactions and scaled by means of a scaling factor, while from BIN5 onward, considered solid particles, the reaction rate is calculated referring to the asymptotic value for BIN20, equal to 5 10^{11} exp(-5000/RT). The pre-exponential factor is multiplied by a collisional efficiency and a temperature function. The activation energy is considered to be zero:

$$K = A_{ref}\,\gamma\,T^{0.5}$$

The collisional efficiency, in case of reactions between a molecular and a radical species, depends on the spherical diameter of the radical with bigger dimensions ($\sigma=\max(d_{A,B})$):

$$\gamma = \frac{100+\sigma^8}{10^6+\sigma^8}$$

The reactions between radical BINs and PAHs refer, as for nucleation, to the recombination of two cyclopentadiene radicals to form naphthalene (k_{ref} = 1.0 10^9 exp(-5000/RT)).

For BINs from 1 to 5 the kinetic constant is scaled with the same method used for reactions between a radical and a molecule, but in this case the activation energy is zero for non-resonant radicals and 3000 if one of the two radical species is resonant. For BINs representing solid particles the asymptotic limit, the temperature dependence and the spherical diameter considered are the same, while the collisional efficiency is calculated as:

$$\gamma = \frac{1000+\sigma^8}{10^6+\sigma^8}$$

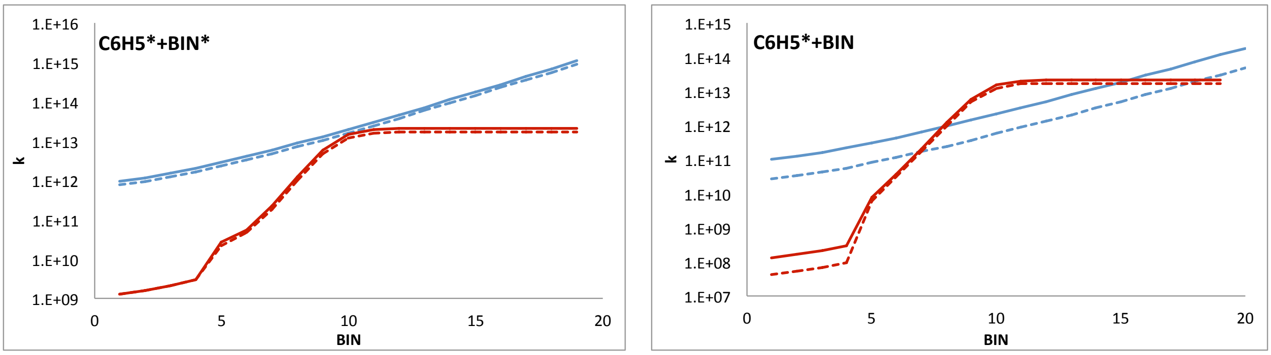

Figure 4.24: Comparison of the kinetic constants for the reactions between PAHs and BINs and in our model (red lines) and D'Anna's model (light blue line). Solid lines: 1800 K, dashed lines: 1200 K.

Another contribution to the growth comes from resonance-stabilized radicals, like C_3H_3, C_4H_3, C_4H_5P and cy-C_5H_5. The kinetic constants are independent from the BIN species and are calculated from a reference value specific for each radical, which is corrected by means of a scaling factor. The reference kinetic constant is given from the reaction of the desired radical species with C_6H_5 or C_6H_6 depending on whether the other reacting species is a radical or a molecule.

4.5.7 Coagulation reactions

Coagulation is the process in which particles coalesce or aggregate, thus their mass increases, while their number decreases. In our model all the particles are considered to be spherical, the information about the fractal form of aggregates is not present yet.

The reaction between two radical BINs refers to the reaction described earlier between two cyclopentadiene radicals to give naphthalene. For a radical coagulating with a molecule, instead, the reference is C_8H_6 reacting with C_6H_5 producing phenanthrene.

For BINs representing large PAHs the kinetic constant is the same as the reference one, corrected with a scaling factor. For particles, instead, the kinetic constant is calculated on the basis of the asymptotic value for coagulation between two BIN20 (k_{ref} = 1.0 10^{11} $T^{0.5}$). The activation energy is zero and the pre-exponential factor is corrected with a frequency factor based on collisional frequencies.

The collisional efficiency, instead, is calculated from interpolation of experimental data[100] in the two different cases of reactions between radical species or between one radical and one molecule. The efficiency for two colliding molecules is the same as the one for a molecule and a radical.

When the interacting species are two radicals, the collisional efficiency depends on the diameter of the bigger particle ($\sigma=\max(d_{A,B})$)

$$\gamma = \frac{10 + \sigma^5}{10^4 + \sigma^5}$$

Whereas in the other cases it can be expressed as:

$$\gamma = \frac{5 + \sigma^6}{5\ 10^4 + \sigma^6}$$

The next step will be to introduce a dependence of the collisional efficiency from the temperature, able to describe the decrease of the efficiency with increasing temperature.

In figure 4.25 the comparison with the values proposed by D'Anna and coworkers is shown.

When coagulation takes place between two molecules, D'Anna considers two different reactions: coagulation and agglomeration. Agglomeration, leading to fractal aggregates, is slower than coagulation for smaller particles and becomes important only for the bigger ones, as confirmed by experimental data. It is worth to notice that in this case the kinetic constant is higher at lower temperature, due to the collision efficiency dependence on temperature.

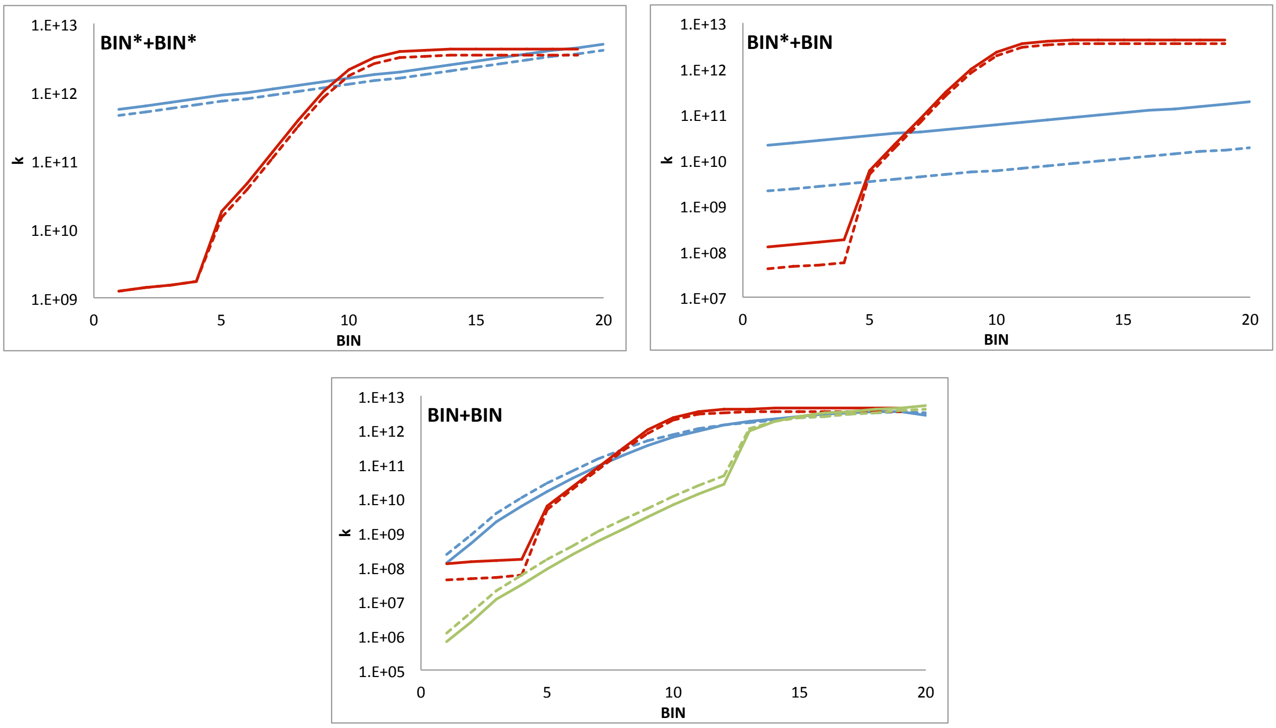

Figure 4.25: Comparison of the kinetic constants for the reactions between PAHs and BINs and in our model (red lines) and D'Anna's model (light blue and green lines). Solid lines: 1800 K, dashed lines: 1200 K. The lower panel shows D'Anna's constant for coagulation (blue lines) and agglomeration (green lines).

4.5.8 Oxidation reactions

Twelve classes of oxidation reactions have been identified; the reaction rates strongly depend on the internal structure. The dominant radical is OH, followed by molecular oxygen:

$O_2 + BIN^* \rightarrow CO + HCO + BIN$ $k_{ref} = 2.1\ 10^{9} \exp(-7400/RT)$

$O_2 + BIN^* \rightarrow O + CO + BIN^*$ $k_{ref} = 2.6\ 10^{10} \exp(-6120/RT)$

$OH + BIN \rightarrow CH_3 + CO + BIN$ $k_{ref} = 1.0\ 10^{10} \exp(-4000/RT)$

$OH + BIN \rightarrow CH_2CO + BIN^*$ $k_{ref} = 1.0\ 10^{10} \exp(-10000/RT)$

$OH + BINi^* \rightarrow aBIN^*_{i-1} + bBIN^*_{i} + CO + gH$ $k_{ref} = 2.0\ 10^{11}$

$O + BIN^* \rightarrow CO + BIN^*$ $k_{ref} = 5.0\ 10^{10}$

$O + BIN \rightarrow HCCO + BIN^*$ $k_{ref} = 2.0\ 10^{10} \exp(-4000/RT)$

$HO_2 + BIN^* \rightarrow OH + CO + BIN^*$ $k_{ref} = 1.0\ 10^{10}$

$OH + BIN \rightarrow BIN + HCO$ $k_{ref} = 3.0\ 10^{9}\ T^{0.5} \exp(-10600/RT)$

$OH + BIN^* \rightarrow BIN^* + HCO$ $k_{ref} = 3.0\ 10^{9}\ T^{0.5} \exp(-10600/RT)$

$O_2 + BIN \rightarrow 2CO + BIN$ $k_{ref} = 4.2\ 10^{8} \exp(-8000/RT)$

$O_2 + BIN^* \rightarrow 2CO + BIN^*$ $k_{ref} = 4.2\ 10^{8} \exp(-8000/RT)$

The reference reactions are oxidations of aromatic species. For the first eight reactions the reference comes from the open meeting on combustion held in Ischia in 2000, while the last 4 reactions refer to the work of D'Anna and Kent[101]. The pre-exponential factor is multiplied by a scaling factor that takes into account the increase of the reaction rate with increasing particles' diameter.

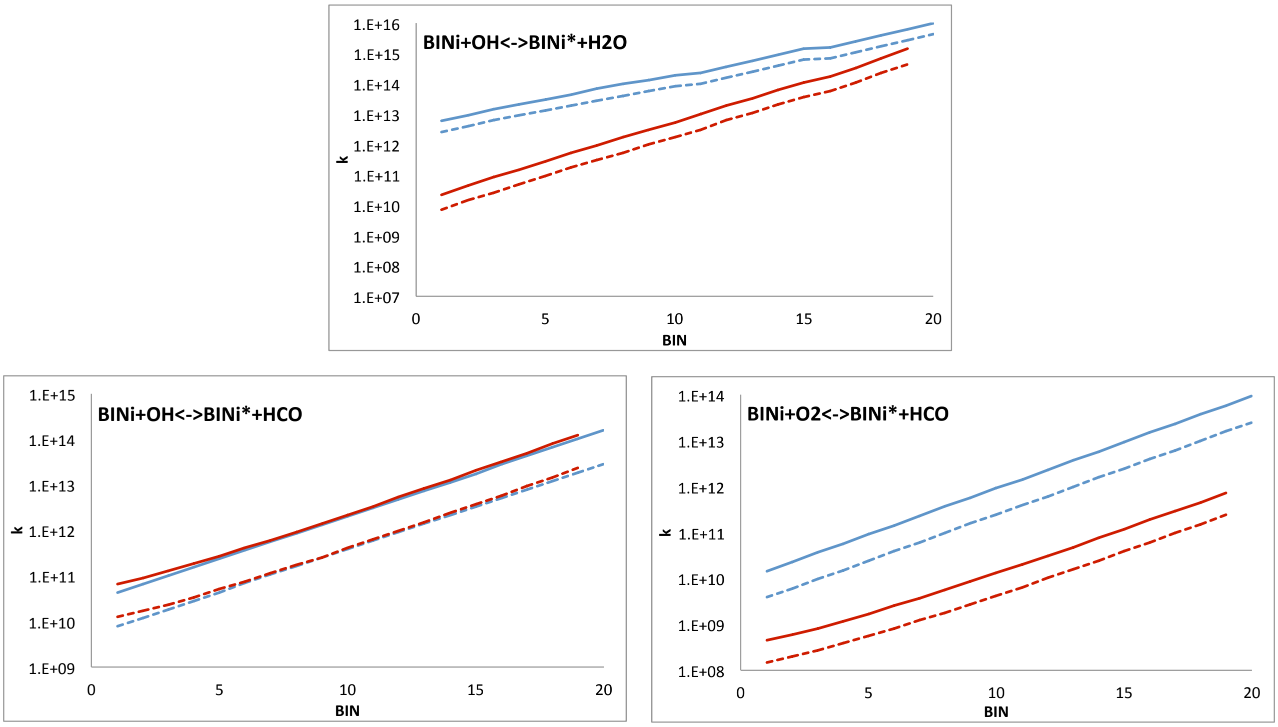

Figure 4.26: Comparison of the kinetic constants for main oxidation classes in our model (red lines) and D'Anna's model (light blue lines). Solid lines: 1800 K, dashed lines: 1200 K.

Currently, the oxidation-induced fragmentation is being introduced in the model.

4.5.9 Demethylation reactions

During demethylation reactions a methyl group is removed from the molecule by a hydrogen atom, causing at the same time a dehydrogenation of the species. The studies of Marinov[102] are taken as reference.

$H + BIN \rightarrow CH_3 + BIN$ $k_{ref} = 1.2\ 10^9 \exp(-5000/RT)$

The reference constant comes from demethylation of aromatic species. This reaction is applied only to the most hydrogenated BINs, with H/C ratio higher than 0.3. The kinetic constant is obtained by multiplying the actual H/C ratio by the reference constant.

The inverse reaction does not play a key role in the system:

$CH_3 + BIN \rightarrow H + H_2 + BIN$ $k_{ref} = 1.2\ 10^9 \exp(-16000/RT)$

4.5.10 Discrete sectional model developed at Università degli studi Federico II

The model developed by D'Anna has a lot of similarities with the one developed in Politecnico, starting from the same approach with the discrete sectional method. In D'Anna's model three classes of particles are defined: ARM1, ARM2 and ARM3 that represent respectively lumped particles, clusters and aggregates. The kinetic constants for different reaction classes are scaled in the same way for the three types of particles. The oxidation induced fragmentation is already implemented in the model and acts differently for clusters and aggregates[81].

The gas phase, instead, is taken from literature and it is based on GRI-MECH 3.0[103] for species C1-C2 and on Miller and Melius' mechanism for C3-C4 species[47]. The growth of aromatics is described through reactions of acetylene addition and recombination of resonance-stabilized radicals.

5 Comparison with experimental data

The modeling and the experimental activities are intimately bound for the development of a reliable kinetic scheme. In fact, even if a mechanism is hypothesized on the basis of theoretical calculations, experimental results are fundamental for the tuning process (described in chapter 2) that leads to a better adherence of the model to reality. The tuning requires a wide range of data collected in different conditions; only this way the model can achieve the “generality” feature. In particular, this thesis work is mainly centered on ethylene as fuel.

In this chapter, the model behavior, with respect to temperature, equivalence ratio and pressure variations, is first analyzed by means of simulations of a plug flow reactor.

Subsequently, the focus is moved on ethylene premixed laminar flames. The capability of the model to predict soot formation under different temperature conditions is tested by means of comparison with the experimental data collected by Ciajolo et al.[104].

The effect of the equivalence ratio is discussed from the simulation of three flames from Faeth and coworkers[105] at atmospheric pressure.

Flames from Tsurikov and coworkers[106] at different pressures and equivalence ratios are then modeled. The influence of the fuel used on the kinetic pathways that lead to soot formation is analyzed through a comparison of three atmospheric flames from ethylene, propylene and toluene. Finally, the burner-stabilized stagnation flame from Wang and coworkers[26] is studied in detail and the sensitivity of the model to the different reaction classes is presented to analyze the influence that each of them has on the mechanism.

The kinetic scheme used for the simulations is the HT1306s, containing 298 species and 16558 reactions. HT stands for “high temperature”, because the reactions that occur only at low temperature are taken out from the scheme, since the low temperature conditions are not of interest to this work. This is an example of the modularity of the scheme (chapter 2), because the ability to select only the reactions that matter at high temperature allows to reduce enormously the computational cost.

5.1 PLUG FLOW REACTOR

The plug flow reactor (PFR) is a convenient environment to study soot formation processes at relatively larger residence time, like surface growth, PAH surface condensation and particle coagulation.

In fact the conditions are similar to those found in the postflame region of laminar flames, but the system is more controllable and well defined. A remarkable difference, however, is that diffusive and thermophoretic effects are not considered in PFRs, even if they play an important role in flames.

The PFR might be schematized as a cylinder with a continuous mass flow. The fluid flowing through the PFR can be modeled as flowing through a series of infinitely thin coherent “plugs”, each with a uniform composition but different from the ones before and after it. Indeed, the assumption underlying the modeling of a PFR is that the mixing of the fluid is perfect on the radial direction, but absent in the axial one.

The simulations are run in an ideal and isothermal plug flow; therefore the temperature is constant along the whole axis. The program used is OpenSMOKE and the PFR is modeled as an ideal reactor.

Specifically, in this paragraph the model behavior is tested by means of simulations of ethylene/air PFRs at two different equivalence ratios: 2.5 and 4. The characteristics of the inlet streams are the defined in table 4.1.

Equivalence ratio ϕ	C_2H_4 mole fraction	O_2 mole fraction	N_2 mole fraction	Temperature [K]	Pressure [atm]
2.5	0.147	0.176	0.677	1800	1
4	0.219	0.164	0.617	1800	1

Table 5.1: Inlet conditions of the simulated PFRs

These conditions were chosen because an equivalence ratio of 2.5 is similar to those found in laminar premixed flames, while a richer flame (equivalence ratio equal to 4) has a more pronounced sooting tendency. Around 1800 K is the temperature at which the model shows a maximum soot volume fraction, as it will be analyzed later.

The evolution of the light gas species in the two different cases (Figure 5.1) shows how the equivalence ratio affects the structure of the system. In fact, ethylene is consumed more slowly in the richer environment, while oxygen is consumed faster. This, together with the lower CO_2 and H_2O concentration at $\phi = 4$, is a clear indication of the fact that the ideal reaction ($C_2H_4 + 3O_2 \rightarrow 2CO_2 + 2H_2O$) is penalized while the pyrolytic mechanism is fostered, as confirmed by the much higher acetylene concentration. Acetylene, as discussed in chapter 4, plays a fundamental role in the formation and growth of the polycyclic aromatic hydrocarbons and hence of soot.

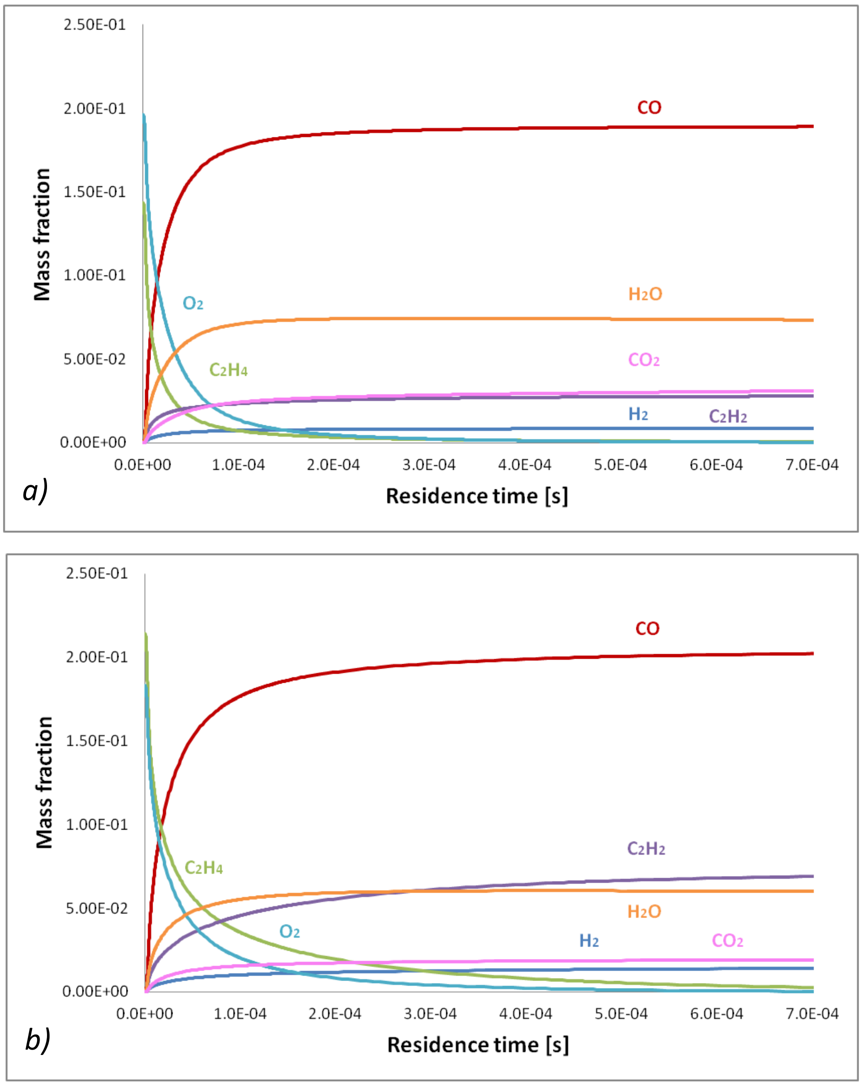

Figure 5.1: Computed mass fractions of light gaseous species in case of $\phi = 2.5$ (Figure *a*) and $\phi = 4$ (Figure *b*).

The pathway that leads to soot formation includes PAHs formation; thus their concentrations are strictly related to the tendency to form soot. Figure 5.2 shows the computed mass fractions of benzene (C_6H_6), naphthalene ($C_{10}H_8$), phenanthrene ($C_{14}H_{10}$) and pyrene ($C_{16}H_{10}$). As expected, their concentrations are higher in richer conditions and in both cases the maximum is shifted toward higher residence time as the molecular weight increases, because heavier PAHs are a subsequent step of the growth of the lighter ones. Their characteristic formation time scale is higher than that of fuel consumption.

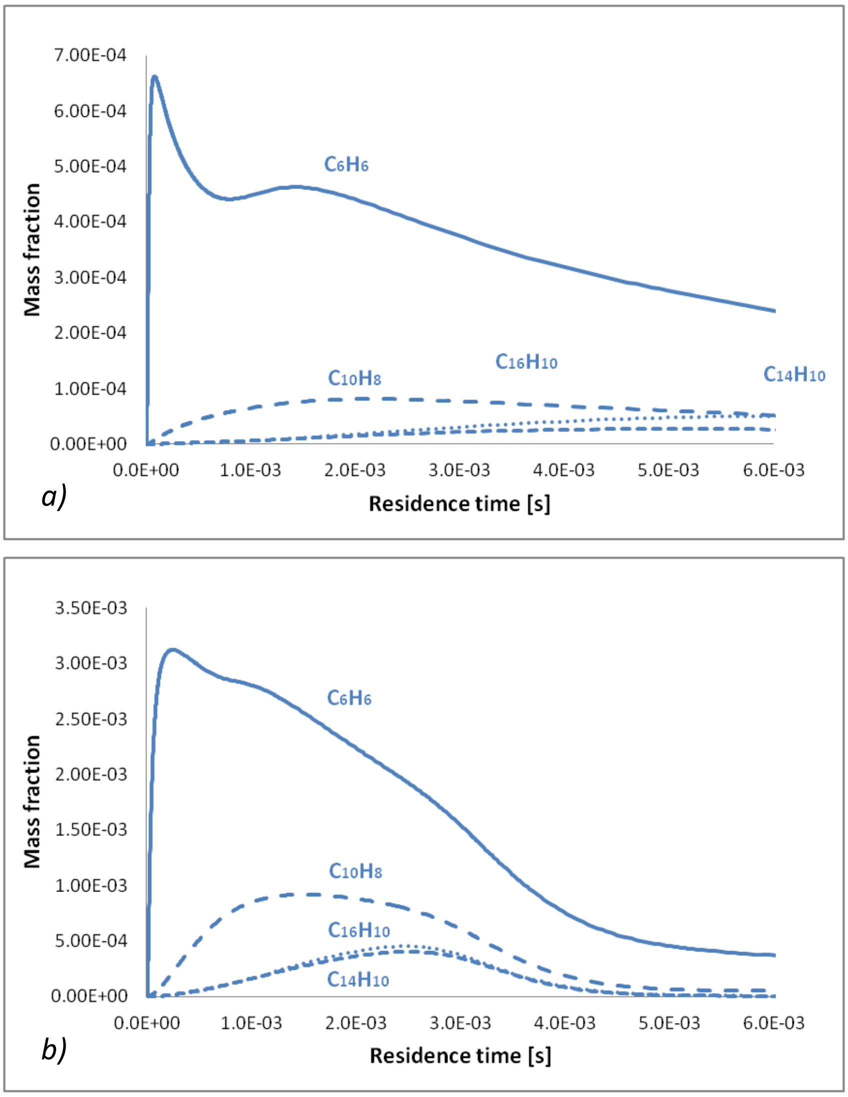

Figure 5.2: Computed profiles of benzene (C_6H_6), naphthalene ($C_{10}H_8$), phenanthrene ($C_{14}H_{10}$), pyrene ($C_{16}H_{10}$). Figure *a*: $\phi = 2.5$. Figure *b*: $\phi = 4$.

A similar trend is found in BINs' profiles. Figure 5.3 represents the computed mass fractions for BIN1, BIN5, BIN20, BIN15 and BIN20 in their molecular (solid lines) and radical (dashed lines) form summing all the differently hydrogenated species. Once again, heavier species show peaks at progressively higher times. Lighter species, in fact, undergo a growing process and become larger particles. Radicals' concentrations become more and more important as the diameter of the particles increases, because the electrons are so delocalized that the instability of the particle is minimal, and they are almost as stable as molecules. This introduces the possibility of eliminating from the kinetic scheme the heavier radicals and treating all the larger particles of a BIN class as one only species.

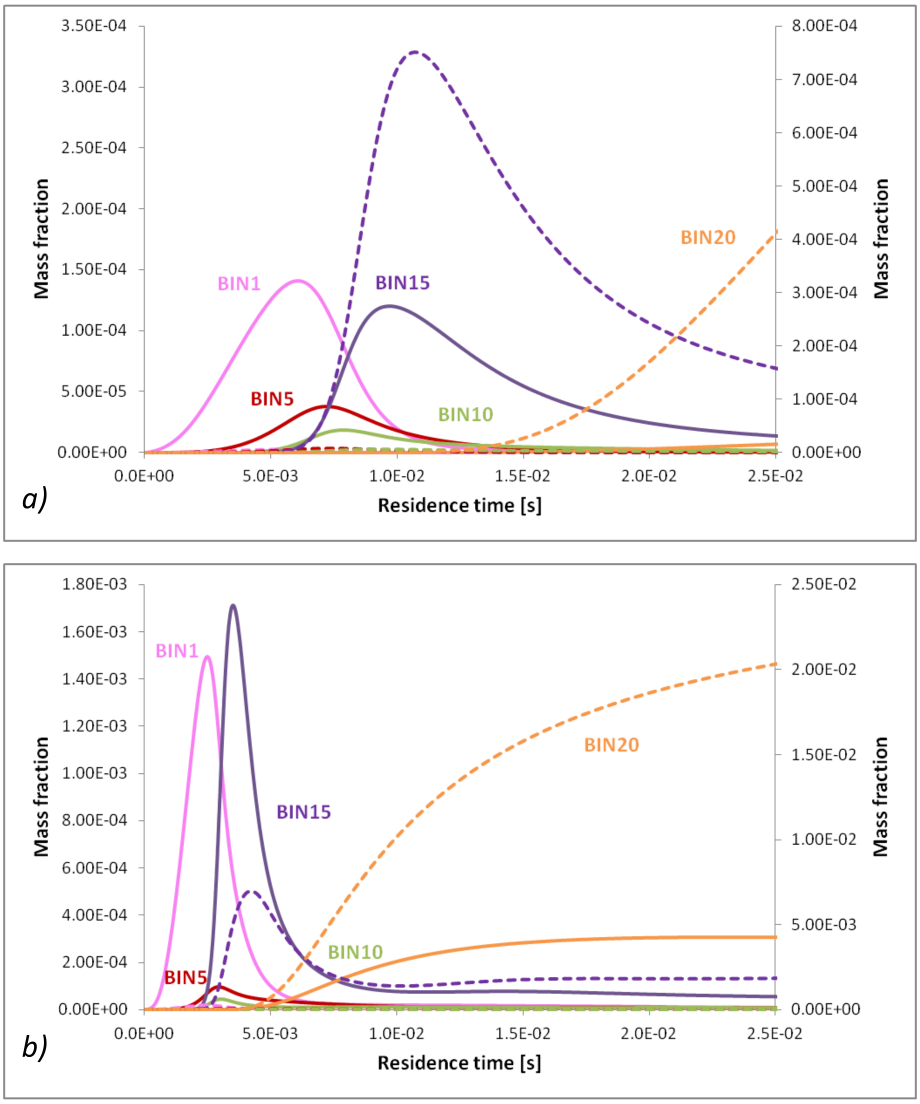

Figure 5.3: Computed mass fractions of BIN1, BIN5, BIN10, BIN15 and BIN20 for the two cases at ϕ = 2.5 (Figure *a*) and ϕ = 4 (Figure *b*). Solid lines: molecular species. Dashed lines: radical species. BIN20J, the radical form, refers to the secondary axis. All the other species refer to the primary axis.

At higher equivalence ratio the concentration of the BINs are higher and they form at lower times, because the pyrolytic pathway is fostered by the absence of oxygen. The same information can be obtained by the particle size distribution function (Figure 5.4). Initially, only small particles are present, while at longer residence times the bimodality becomes stronger, because nucleation is still active, forming small particles, but the growth process leads to the formation of the first aggregates. At longer residence times larger particles become predominant. This evolution is slower in leaner conditions, while at ϕ = 4 aggregates form faster, as already discussed by analyzing the BINs' profiles evolution in time.

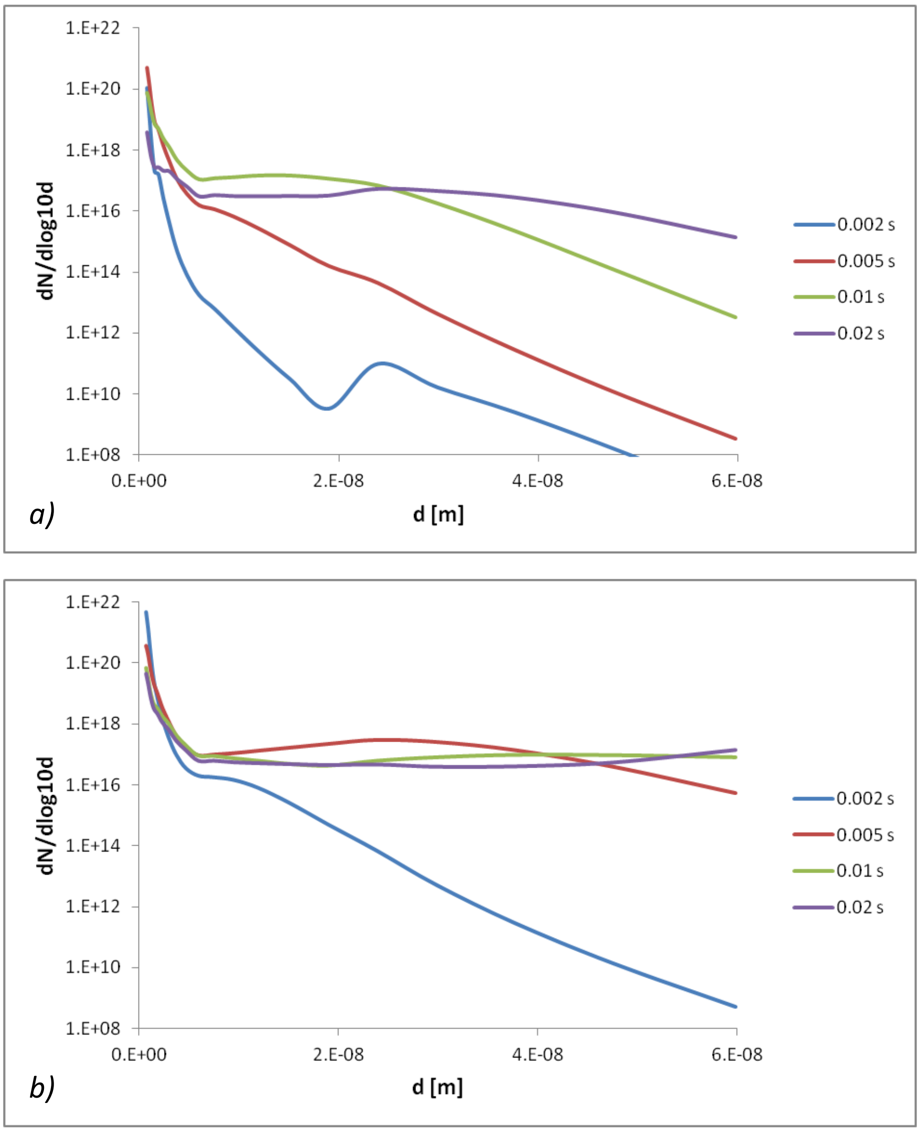

Figure 5.4: Computed particle size distribution functions for soot particles at 2, 5, 10 and 20 ms. Figure *a*: ϕ = 2.5. Figure *b*: ϕ = 4.

The soot mass fraction (Figure 5.5) in function of the residence time in the PFR reactor substantially confirms a more pronounced tendency to soot formation in richer environments.

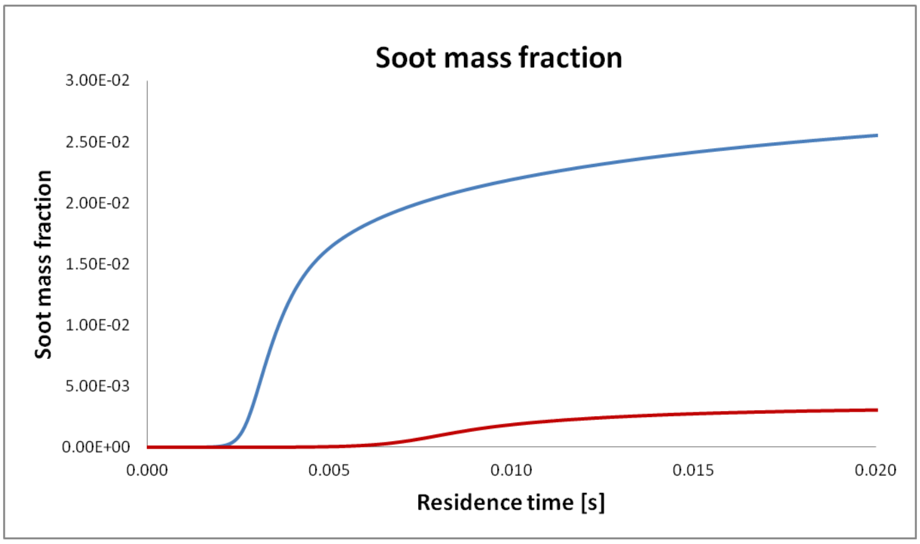

Figure 5.5: Computed soot mass fraction in case of ϕ = 2.5 (red line) and ϕ = 4 (blue line).

The total number density (Figure 5.6), to which small particles contribute the most, shows how the nucleation phenomena start earlier at higher equivalence ratios, as seen from the shift of the maximum toward lower residence times. The maximum in the number density is due to coagulation phenomena that increase the molecular mass but decrease the number of particles because of coalescence.

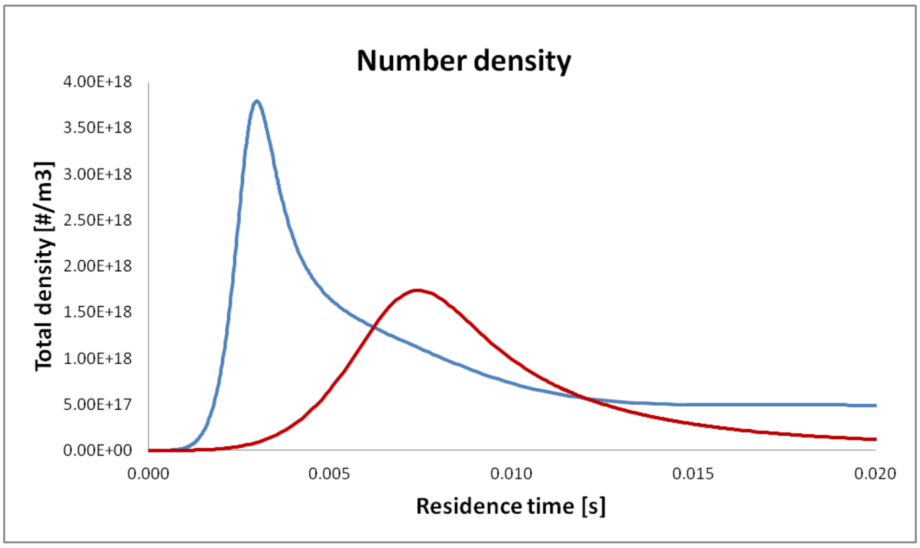

Figure 5.6: Computed total number density in case of ϕ = 2.5 (red line) and ϕ = 4 (blue line).

It is worth to discuss the variation of soot mass fraction as a function of temperature and pressure. Soot mass fraction presents a maximum with respect to temperature[107], because at low temperatures the process is not activated, while at high temperature and in pyrolytic conditions particles break up to produce acetylene, which is more stable. Soot production is very sensitive also with respect to pressure, because growth reactions like condensation and coagulation involve a decrease of the moles' number; therefore they are favored by a pressure increase (at least in the pressure-range of interest). For this purpose simulations were run with the same conditions presented earlier at ϕ = 2.5; the results, at 0.02 s residence time and pressures of 0.1, 1 and 5 atm, are presented in figure 5.7.

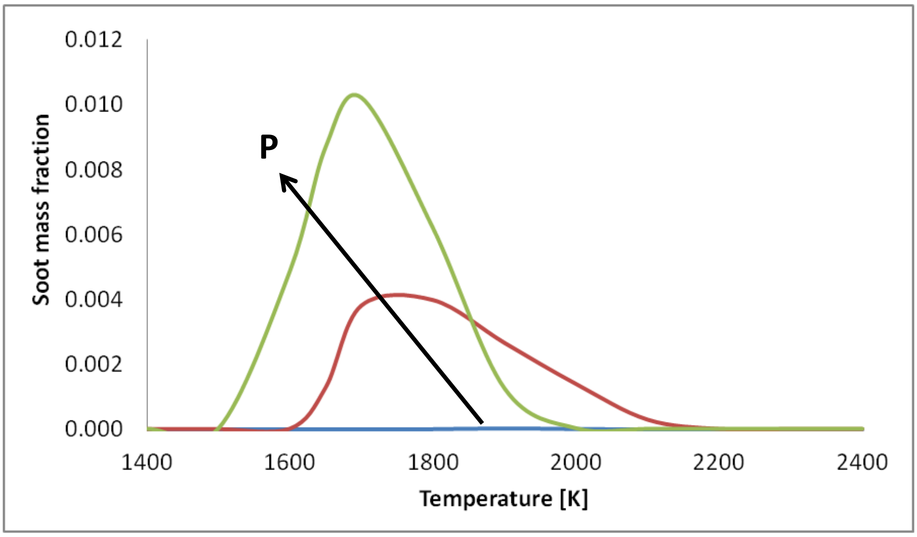

Figure 5.7: Results from the numerical simulation at ϕ = 2.5 of the soot mass fraction as a function of temperature at 0.02 s residence time and different pressures. Green line: 5 atm; red line: 1 atm and blue line: 0.1 atm.

5.2 LAMINAR PREMIXED FLAMES

Laminar premixed flames involve the combustion of a premixed mixture of reactants. The reaction occurs at constant pressure, with heat and light radiation, analogously to what described in paragraph 3.3, chapter 3, for the burner-stabilized stagnation flame. Different regions can be distinguished inside a laminar premixed flame. The first region consists in the unburned mixture approaching the flame zone. As it approaches the flame front, in the preheat region it is heated by conduction and radiation from upstream. Once temperatures are high enough, chemical reactions are activated, thus creating the reaction zone, where the combustion takes place. The products of reaction form the burned gas zone. Each laminar premixed flame has a distinct characteristic burning velocity, which is the speed at which a flame front propagates relative to the unburned gas.

5.2.1 Experimental data from Ciajolo et al: effect of temperature

Ciajolo and coworkers[104] studied the temperature dependence of soot in fuel-rich, premixed C_2H_4/O_2 flames. As seen in the previous paragraph, soot production forms a bell-shaped domain with respect to temperature. To analyze such behavior three different flames are set up, all with the same equivalence ratio but different cold-gas velocities, which means different temperatures.
The flames are stabilized on a water-cooled, sintered-bronze McKenna burner (diameter = 6 cm) surrounded by a shroud of nitrogen. The temperature is measured with a thermocouple following a fast insertion procedure to prevent soot from depositing and affecting the measurements, while the measured species are sampled by means of a stainless steel, water-cooled probe. On-line gas chromatography is used to analyze the light hydrocarbons and the amounts of soot and condensable species are determined gravimetrically. Table 5.2 shows the characteristics of the three flames.

	Equivalence ratio ϕ	C_2H_4 mole fraction	O_2 mole fraction	Cold gas velocity [cm/s]	Maximum Temperature [K]	Pressure [atm]
Flame 1	2.4	0.444	0.556	2	1520	1
Flame 2	2.4	0.444	0.556	4	1715	1
Flame 3	2.4	0.444	0.556	6	1820	1

Table 5.2: Inlet characteristics of the premixed laminar flames of Ciajolo et al.[104]

The temperature profiles (Figure 5.8) are imposed in the simulation; therefore the energy balance is taken out from the system of equations to be solved.

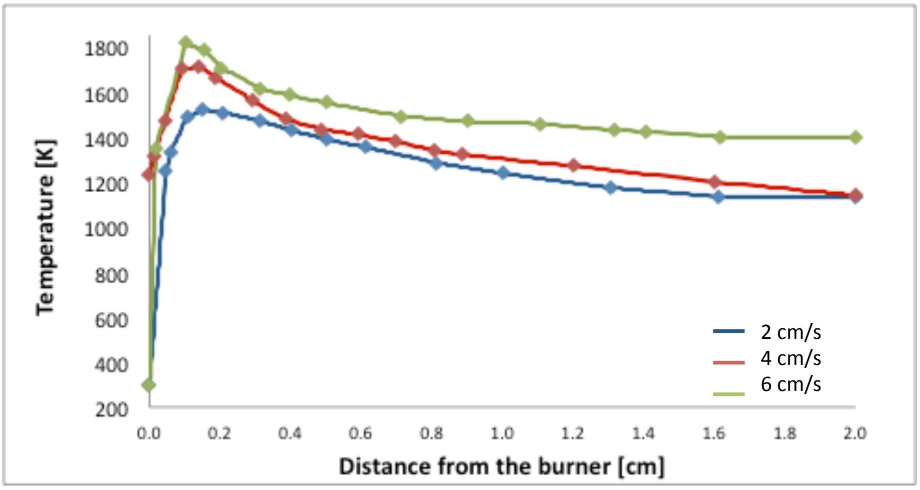

Figure 5.8: Measured temperature profiles for the three flames. The diamonds represent the experimental points, the lines are the fitting performed by OpenSMOKE. Blue line: flame 1; red line: flame 2; green line: flame 3.

Figure 5.9 shows the profiles of ethylene, acetylene and benzene along the flame axis for the three different flames. To account for the probe perturbation the computed profiles are shifted to match the 50% of ethylene conversion.

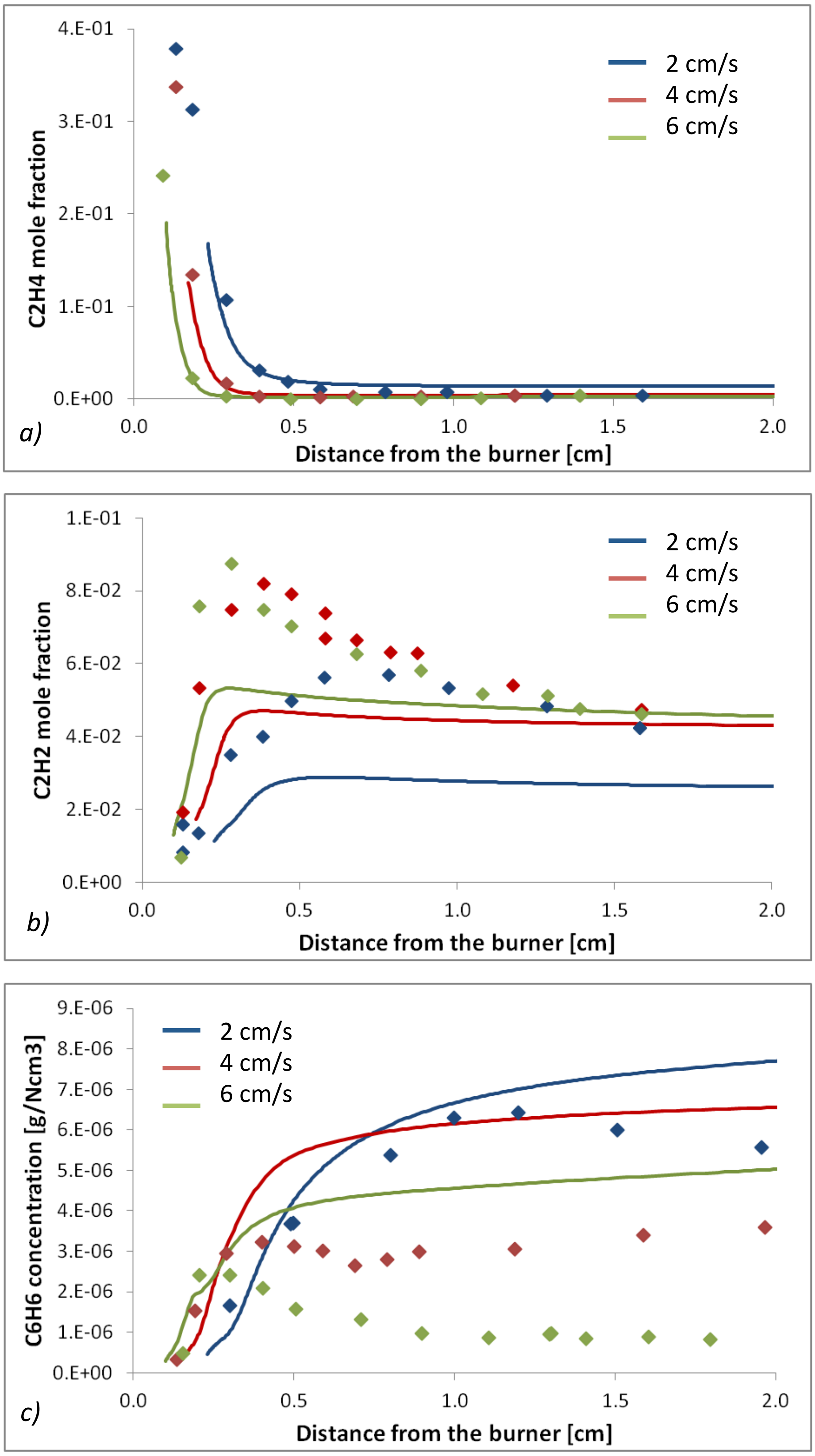

Figure 5.9: Comparison between experimental measurements (diamonds) and computed profiles (solid lines) of ethylene (Figure *a*), acetylene (Figure *b*) and benzene (Figure *c*) in the three flames. Blue diamonds and lines: flame 1; red: flame 2; green: flame 3.

As the cold-gas velocity increases the maximum temperature, located around the flame front, rises, increasing the burning velocity and hence shortening the main reaction zone. In fact, fuel is consumed closer to the burner surface, all the species profiles shift and ethylene conversion increases. Acetylene peaks after the fuel is consumed and then levels off. Even though the model underpredicts acetylene concentration in the main reaction zone, the relative trend of the three flames is well represented and further from the burner the computed concentrations of the two flames at higher temperature match the experimental data. Probably in the flame with the lowest cold-gas velocity the temperature is too low to activate the reactions that lead to acetylene production. If we compare the rates of production at the lowest temperature (figure 5.10, first panel) and the highest (figure 5.10, second panel) it can be noticed that the reactions involved are not drastically different, the pathway is analogous, but the main reactions leading to acetylene formation at high temperature lose importance at low temperature with respect to acetylene disruption pathways.

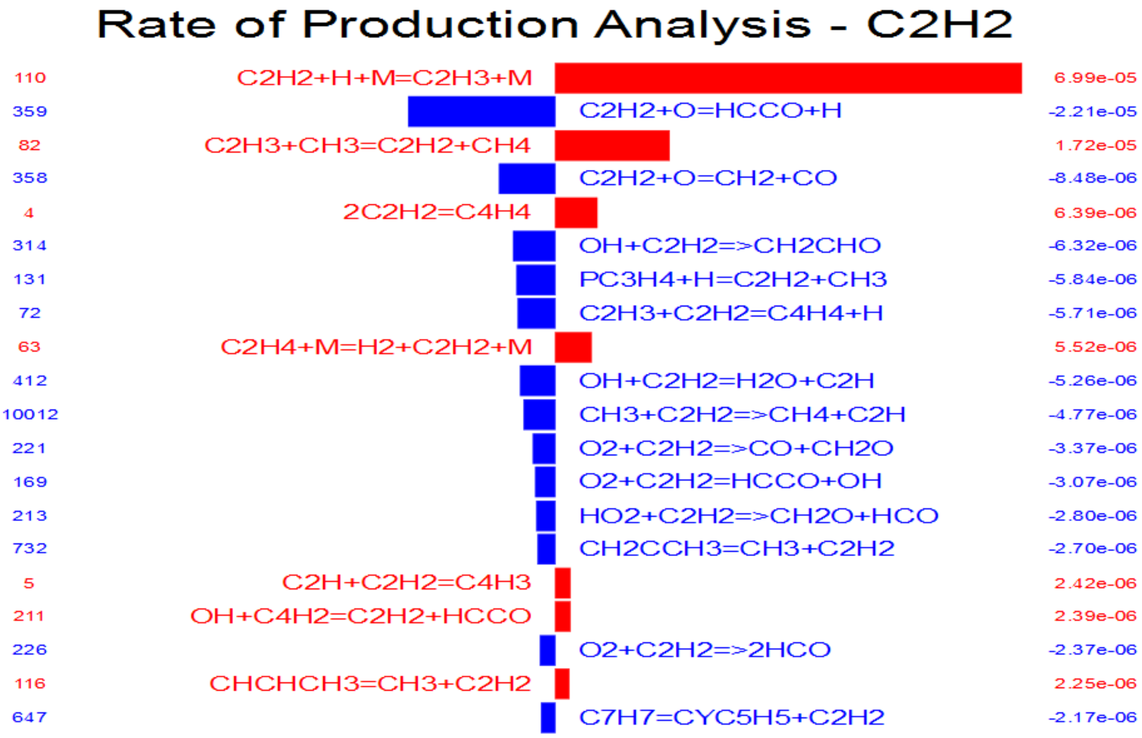

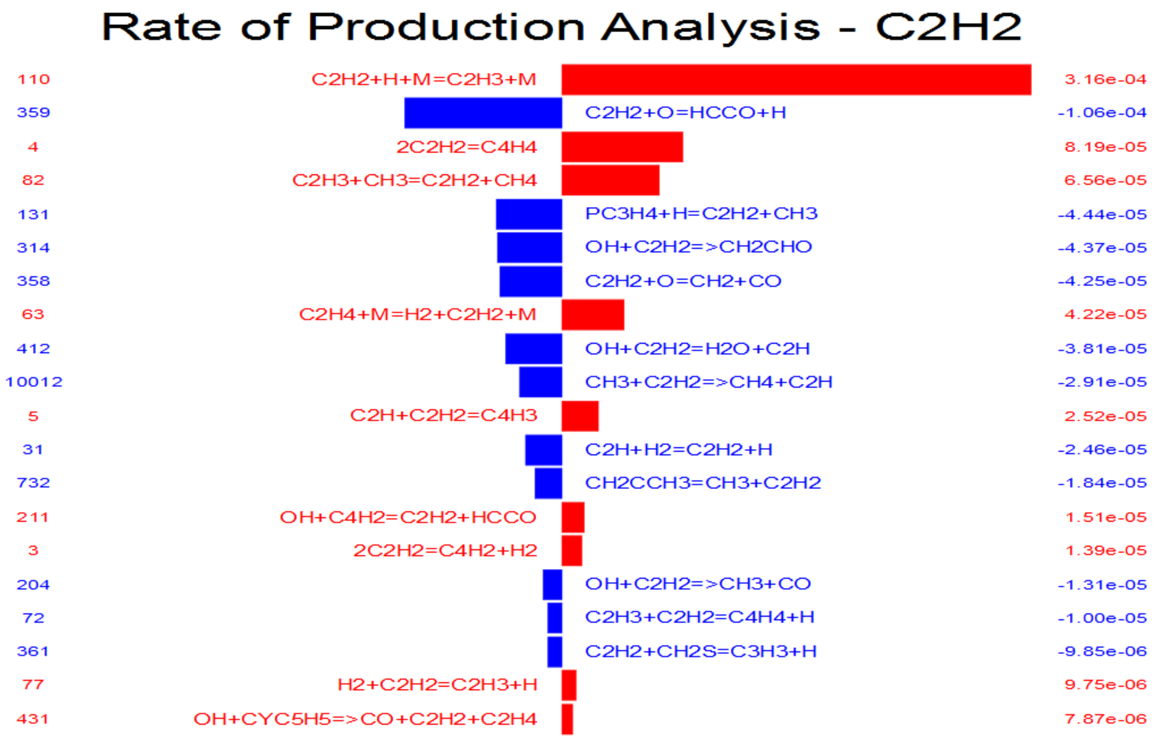

Figure 5.10: Rate of production analysis for flame 1 (upper panel) and flame 3 (lower panel). The numbers on the left column identify the reaction number inside the kinetic scheme. The right column presents the values of the global rate of reaction. The negative values indicate reactions that lead to depletion of the considered species, the positive ones those in which the species is produced.

The model overpredicts benzene concentration, even though the trend is well represented. In this case the penalization of kinetics due to lower temperature allows the model to match the experimental data. Soot concentration (Figure 5.11) is underpredicted, as it could be expected considering that the acetylene plays a fundamental role in the growth process of PAHs and soot. For flame 1 the model does not see any soot formation, because the temperature is too low to activate the processes of the pathway that leads to its production. Figure 5.11*b* shows the measured and computed maximum soot concentrations as a function of the maximum flame temperature. The soot bell described earlier in this case attains the experimental maximum at 1700 K, whereas the model is still in the rising side of the bell, confirming the PFR results (figure 5.7) under similar conditions, at atmospheric pressure, which showed that 1700 K is a threshold temperature for soot formation and that the maximum of the bell is reached around 1800 K.

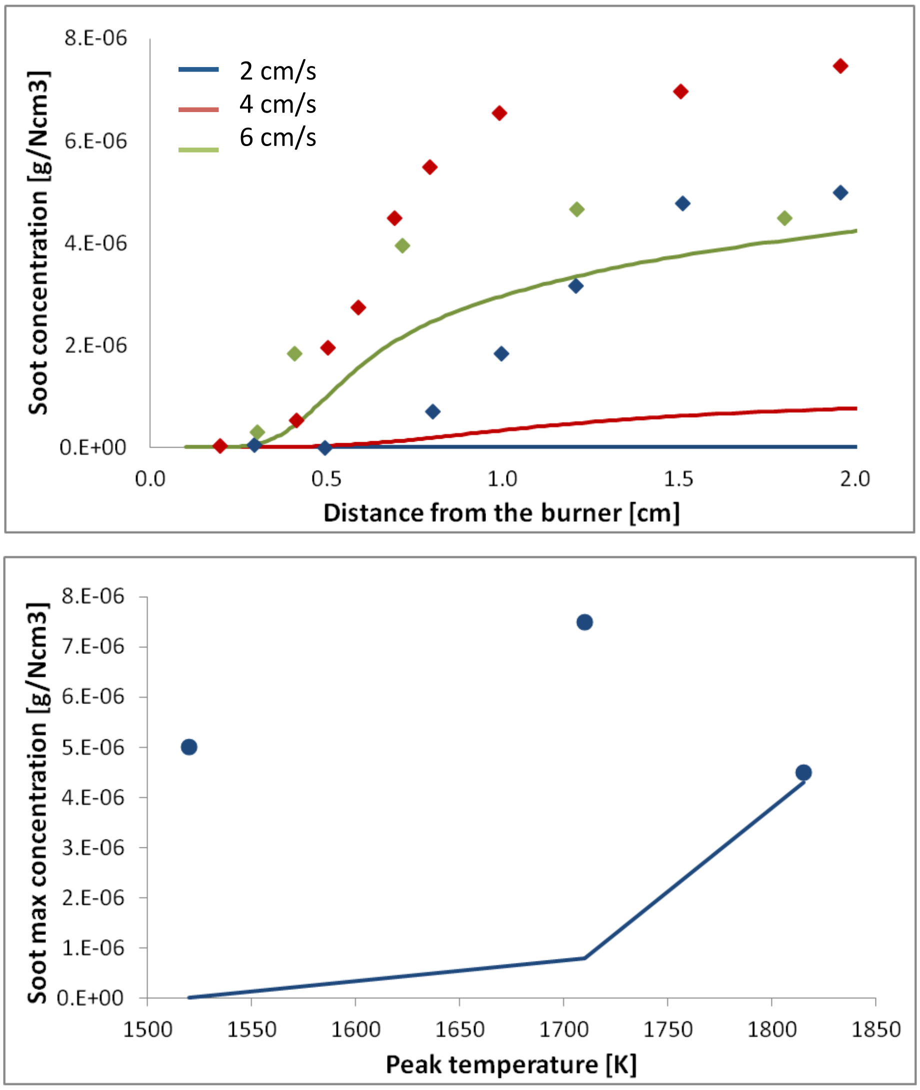

Figure 5.11: Comparison between experimental measurements (diamonds) and computed profiles (solid lines) of soot concentration in the three flames along the flame axis (Figure *a*). Blue diamonds and lines: flame 1; red: flame 2; green: flame 3. Figure *b*: Maximum soot concentration against maximum flame temperature. Dots are the experimental values, the solid line the computed ones.

5.2.2 Experimental data from Faeth and coworkers: effect of equivalence ratio

Faeth and coworkers[105] studied soot formation in laminar premixed ethylene/air flames at atmospheric pressure with respect to variations of the equivalence ratio (between 2.35 and 2.95). The flames are produced by a 6 cm diameter water-cooled McKenna burner with wide annular nitrogen flow. Soot volume fractions were measured using both laser-extinction measurements and gravimetric methods, with experimental uncertainties less than 15%. Concentration of major gas species are measured by gas chromatography, with experimental errors below 15%.

Temperatures were found with multiline emissions measurements, with experimental uncertainties below 50 K. Table 5.3 shows the characteristics of the three flames.

	C/O ratio	Equivalence ratio ϕ	Cold gas velocity [cm/s]	C_2H_4 mole fraction	O_2 mole fraction	N_2 mole fraction
Flame 1	0.78	2.34	6.8	0.14	0.18	0.68
Flame 2	0.88	2.64	6.8	0.156	0.177	0.667
Flame 3	0.98	2.94	5.3	0.17	0.174	0.656

Table 5.3: Inlet characteristics of the premixed laminar flames of Faeth et al.[105]

The profiles of the major species at different C/O ratio are shown in figure 5.12. The experimental data are presented in a logarithmic scale; therefore it is difficult to make a precise comparison. However, there is a good agreement between the model and the measured values.

Similarly to the PFR, ethylene is consumed more slowly in the richer environment, since oxygen is consumed faster (even though the experimental oxygen profiles are not shown in the paper). CO_2 and H_2O concentration decreases in richer flames, because the ideal reaction is penalized.

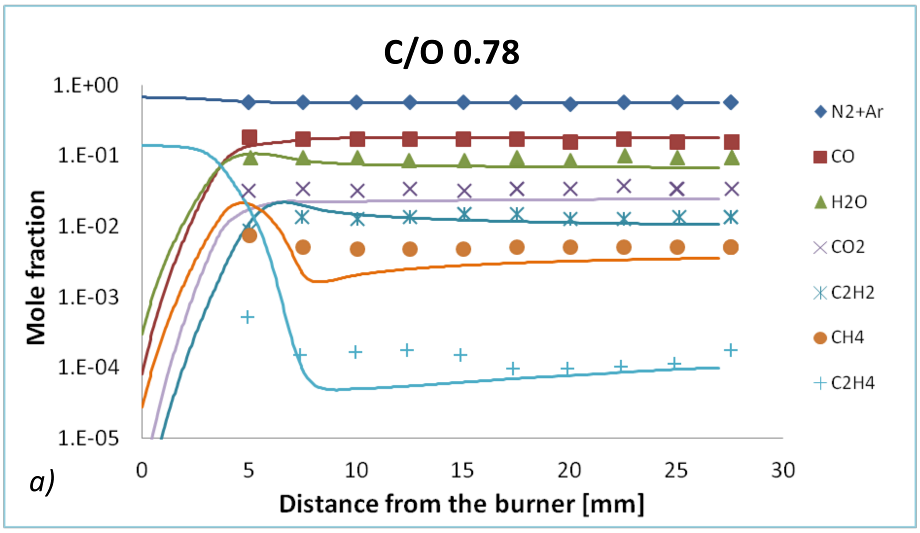

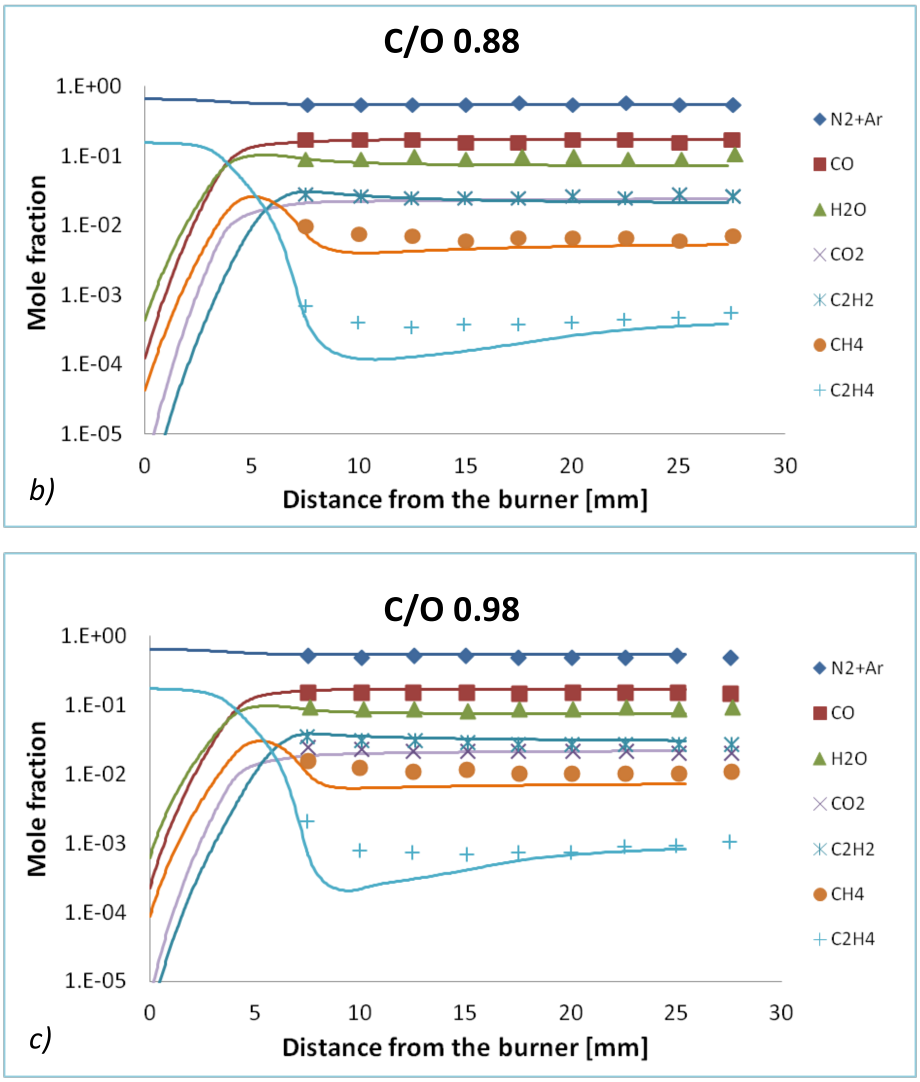

Figure 5.12: Comparison between the experimental measurements and simulation results (solid lines) for the major gas species at the three different C/O ratios.

The soot volume fraction is presented (Figure 5.13, solid lines and diamonds), together with the temperature profiles (Figure 5.13, dashed lines). At higher C/O ratios of course the soot volume fraction is higher, because the pyrolytic pathway is fostered. The model predicts well the point of soot inception, but overpredicts the soot volume fraction for the richest flame. No data on number density or PSDFs are available, hence it is hard to analyze the possible causes of the overestimation.

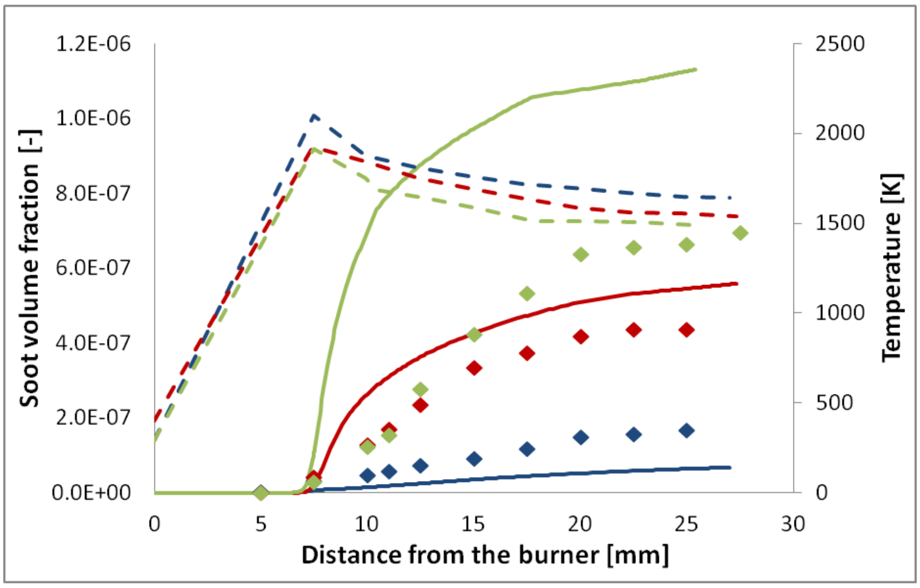

Figure 5.13: Comparison between the computed (solid lines) and experimental (diamonds) soot volume fraction profiles. Dashed lines: temperature profiles. Blue: C/O = 0.78; red: C/O = 0.88; green: C/O = 0.98.

5.2.3 Experimental data from Tsurikov et al.: effect of pressure, equivalence ratio and fuel

Tsurkov and coworkers[106] conducted an experimental investigation into soot formation in laminar premixed flames at atmospheric and elevated pressures (1-5 bar). The flames are produced in a dual-flame burner enclosed in a pressure housing; air is used as oxidizer. Soot volume fraction measurements are obtained using laser-induced incandescence, while temperature measurements are obtained with shifted vibrational coherent anti-Stokes Raman scattering. The experimental errors are within 30% for soot volume fraction and 3% for the temperature. The results from ethylene flames at different pressures and equivalence ratios are here presented and the pathways leading to soot are compared with those of two atmospheric pressure flames burning propylene and toluene. A summary of the inlet conditions and characteristics of the flames here discussed is presented in table 5.4.

Fuel	ϕ	Pressure [atm]	Inlet mass flow rate [kg/s]	Maximum temperature [K]	Maximum soot f_v experimental	Maximum soot f_v computed
C_2H_4	2.3	1	1.2e-4	1734	0.5	0.5
	2.5	1	1.2e-4	1671	0.6	0.4
	2.3	3	2.6e-4	1732	1.7	2.25
	2.5	3	2.6e-4	1710	4	2.3
	2.05	5	3.2e-4	1724	1.7	2.3
	2.4	5	3.2e-4	1738	10	6.4
C_3H_6	2.23	1	8.8e-5	1672	0.7	0.07
C_7H_8	1.88	1	3.6e-5	1490	3.25	$7.8\ 10^{-7}$

Table 5.4: Inlet conditions and summary of the characteristics of the premixed laminar flames from Tsurikov et al.[106]. ϕ is the equivalence ratio and f_v the soot volume fraction.

The comparison between the experimental and computed values of the maximum soot volume fraction for the ethylene flames is shown in figure 5.14. The model manages to predict the soot volume fractions quite well at different pressures and equivalence ratios.

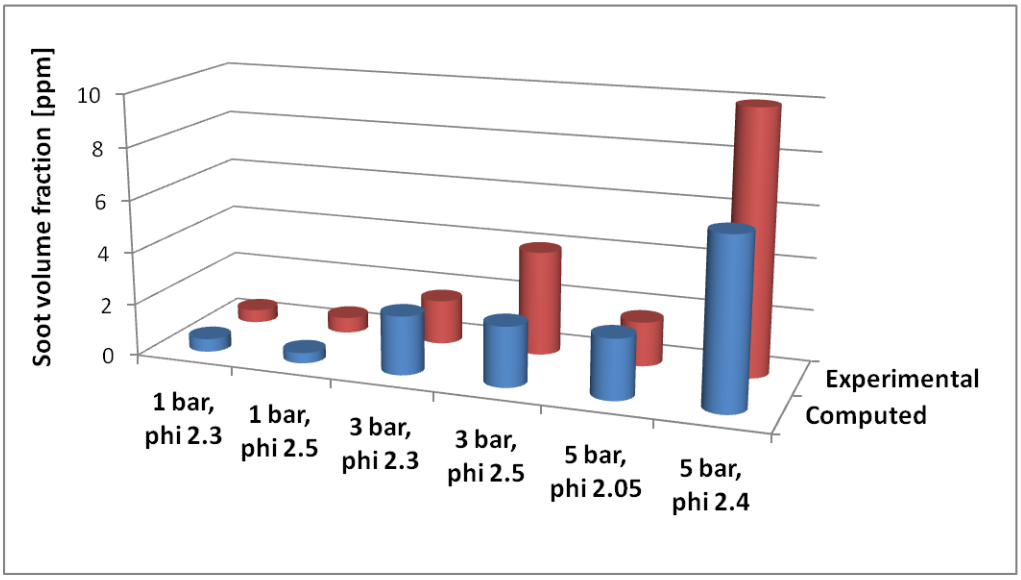

Figure 5.14: Comparison between the experimental and computed values of the maximum soot volume fraction in the ethylene flames.

C_2H_4

Pressure: 1 atm

Φ = 2.3 Φ = 2.5

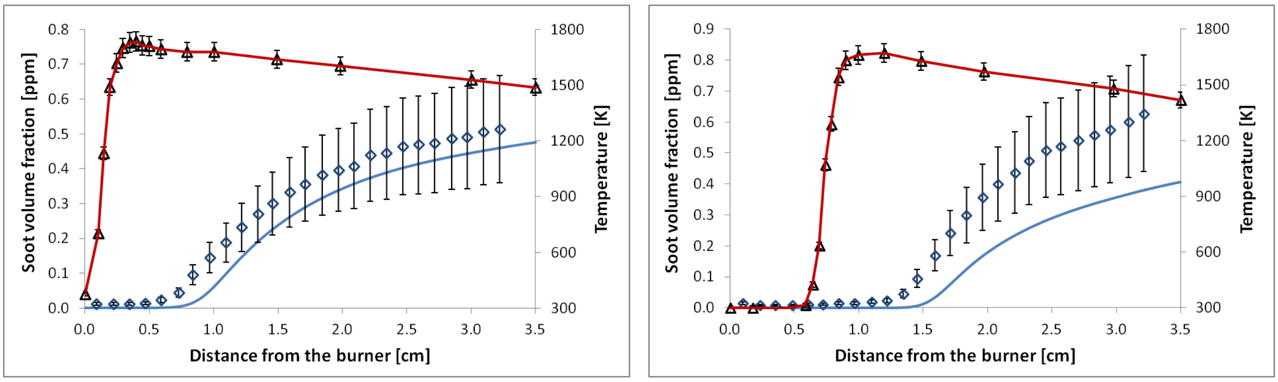

Pressure: 3 atm

Φ = 2.3 Φ = 2.5

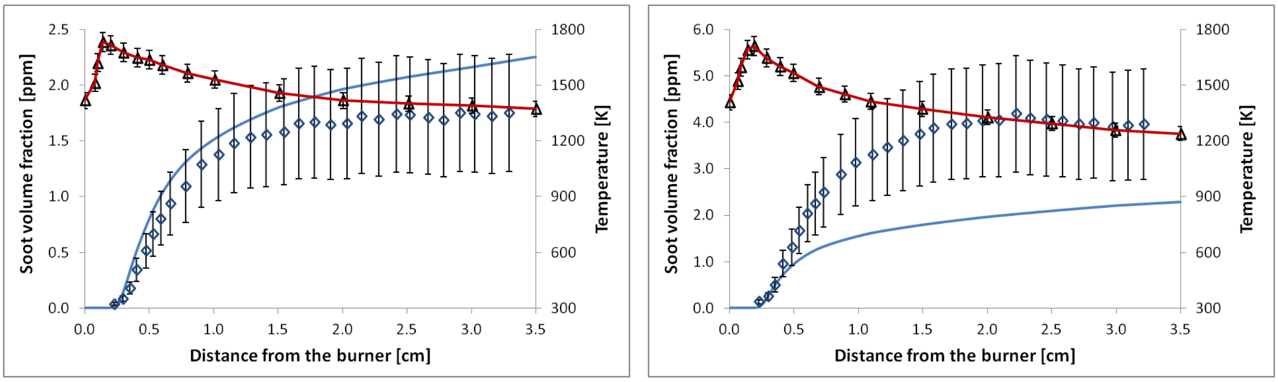

Pressure: 5 atm

Φ = 2.05 Φ = 2.4

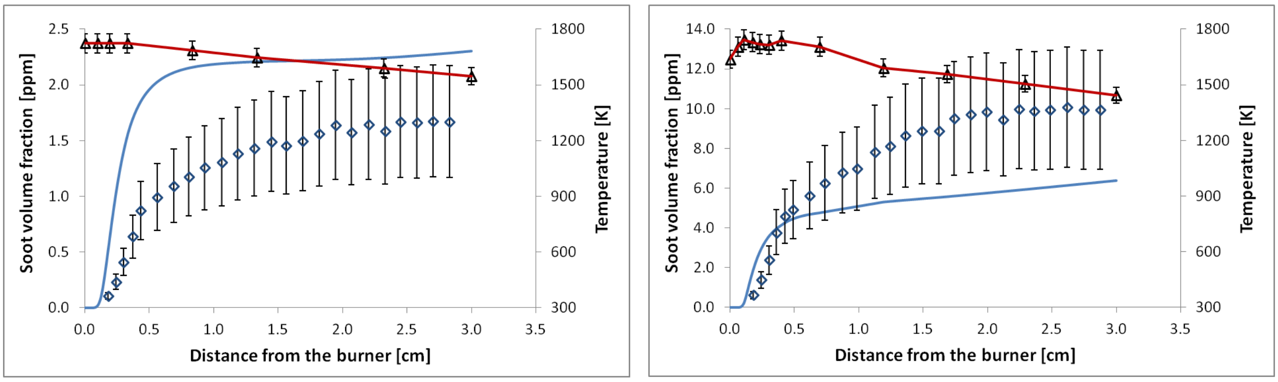

Figure 5.15: Comparison of the experimental and the computed soot volume fraction profiles along the flame axes. Triangles: experimental measurements of temperature. Red: temperature from OpenSMOKE interpolation. Blue: soot volume fraction; diamonds: measured values; solid line: computed values.

In figure 5.15 the temperature and soot volume fraction profiles are illustrated. The temperature peaks in the main reaction zone; at higher heights above the burner it decreases because of radiative losses from soot particles. Soot starts to form further downstream with respect to the main reaction zone, after the sequential growth processes have occurred. The soot volume fraction increases with pressure and its formation starts closer to the burner surface. Surface growth, nucleation and coagulation reactions are in fact enhanced at higher pressure, fostering the pathway that leads to soot. The earlier soot formation, instead, is related to the shift of the main reaction zone towards the burner surface because, as described in the paper, the flame it self moves closer to the burner since it was not possible to lift it at high pressure.

Figure 5.16 shows the experimental and computational results for the propylene and toluene flames.

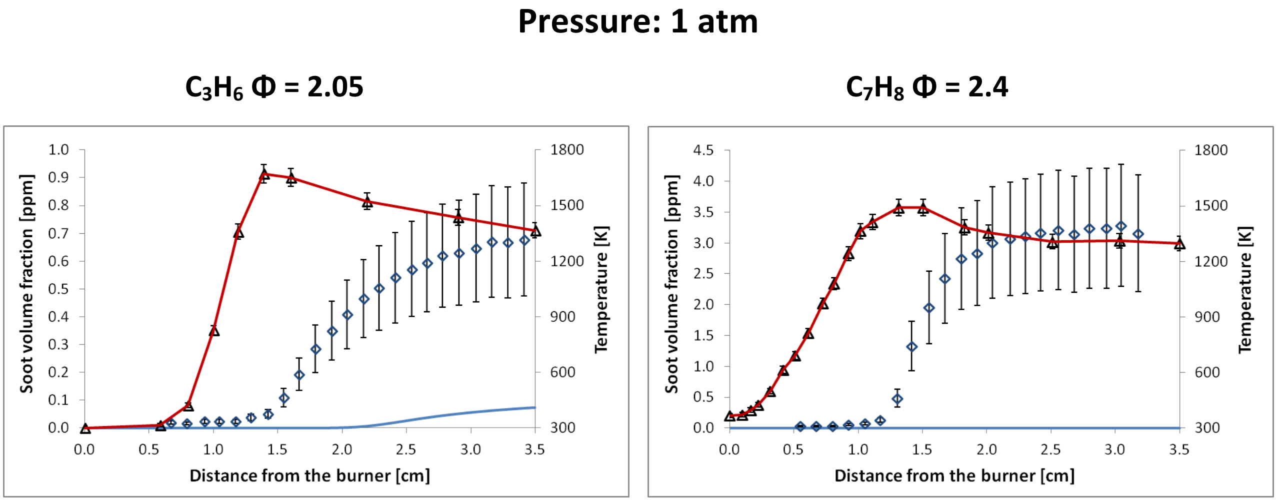

Pressure: 1 atm

C_3H_6 Φ = 2.05

C_7H_8 Φ = 2.4

Figure 5.16: Comparison of the experimental and the computed soot volume fraction profiles along the flame axes. Triangles: experimental measurements of temperature. Red: temperature from OpenSMOKE interpolation. Blue: soot volume fraction; diamonds: measured values; solid line: computed values.

The model capability to predict soot concentration is worse in case of propylene and toluene. The maximum temperature reached in the toluene flame according to the experimental results is around 1490 K; not high enough to activate significantly the pyrolytic pathway to soot in the model.

However, it is interesting to analyze the situation in greater detail by studying the different pathways that lead to soot depending on the fuel. Figure 5.17 represents the results from the rate of production analysis for the ethylene flame at atmospheric pressure with equivalence ratio equal to 2.3, the propylene and the toluene flame.

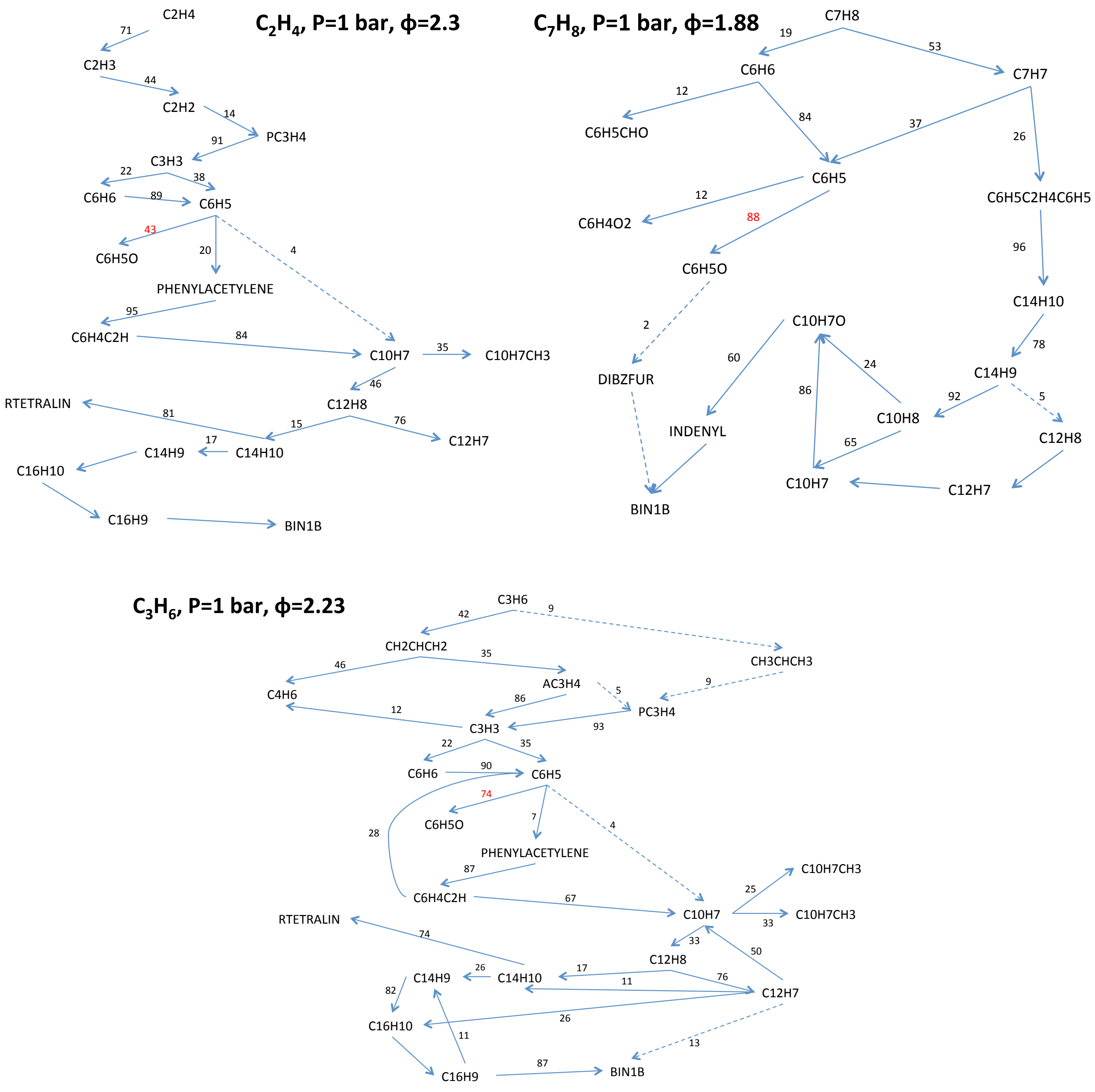

C_2H_4, P=1 bar, ϕ=2.3

C_7H_8, P=1 bar, ϕ=1.88

C_3H_6, P=1 bar, ϕ=2.23

Figure 5.17: Pathways from fuel to BIN1B for ethylene, propylene and toluene flames. The numbers on the arrows represent the percentage of reactant that is converted into a product based on the sum of the rates of reactions (as those seen in figure 5.10) considered with their stoichiometry.

In ethylene and propylene flames after the formation of the propargyl radical (C_3H_3) the pathways are analogous. The central step is the formation of phenyl radical that afterwards grows to phenylacetylene, naphthalene and heavier PAHs. The importance of the HACA mechanism can be clearly understood, since it can be noticed how the most important steps involve growth of PAHs through addition of two carbon atoms. In the toluene flame, instead, the HACA mechanism does not play a central role in the kinetic scheme, because most of the fuel undergoes a dimerization reaction through the benzyl radical (C_7H_7) that leads to phenanthrene ($C_{14}H_{10}$). Afterwards, the phenanthrene forms naphthalene and acenaphthylene by means of demethylation reactions and the main pathway to soot formation involves indenyl.

Another interesting step is the competition of phenyl reaction to phenylacetylene and the oxidation to phenoxy radical (C6H5O). The underprediction of soot volume fraction is more important in toluene flames where soot is basically not produced, then in propylene flames and finally in ethylene flames the prediction is inside the experimental error and this might be related to this step. In fact, the percentage of phenyl reacting to phenoxy radical is 88% in the toluene flame, 74% in the propylene flame and 43% in the ethylene one.

Two factors might contribute: first, the three flames do not have the same equivalence ratio, therefore oxygen concentration is lower in the ethylene flame with respect to the others (Figure 5.18); besides, acetylene concentration decreases from ethylene to propylene and then to toluene. If acetylene concentration is too low the HACA mechanism is penalized with respect to the oxidation to phenoxy radical. This would explain the smaller importance of the HACA mechanism in the toluene flame and the subsequent soot underestimation.

These results highlight the need of further investigations in case of different fuels. Moreover, it clearly appears the necessity of a larger set of experimental data in case of fuels different from ethylene, which is the most investigated in literature.

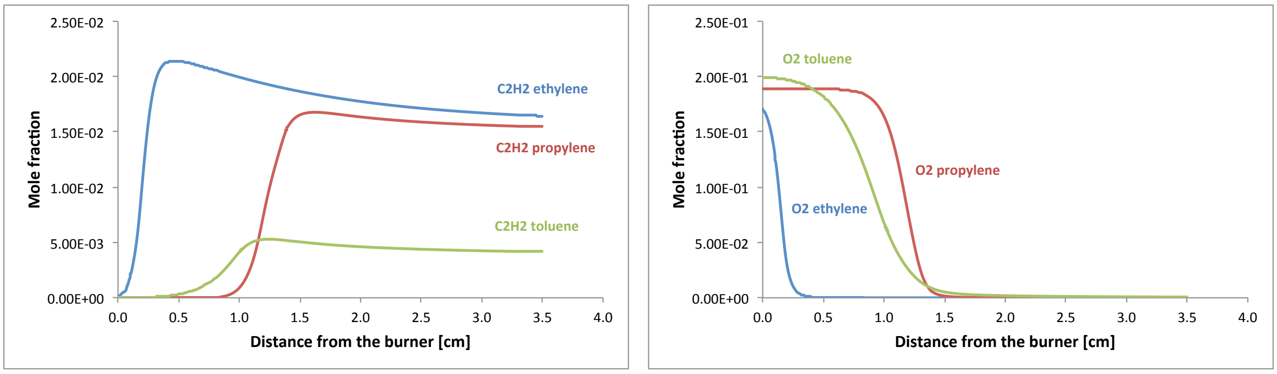

Figure 5.18: Acetylene profiles in the three flames under analysis: blue line: ethylene flame; red line: propylene flame; green line: toluene flame.

This is also an example of how the model is tuned with experimental data. In fact, the model can be tested against experimental data under different conditions and with different fuels involving oxidation to understand if indeed the kinetic constant for this reaction has to be lowered.

5.3 BURNER-STABILIZED STAGNATION FLAME of Wang et al.

Wang and coworkers[26] introduced an innovative method to measure soot volume fraction and particle size distribution that allows to describe rigorously the perturbation brought to the flame by the sampling probe through well defined boundary conditions.

The stagnation plane approach has been widely described in chapter 3, together with the equations used to describe it as a counterflow flame with zero velocity on the oxidizer side.

It is important to notice that each sampling position gives a different flame, even if the inlet conditions are the same, because the temperature and velocity profiles change with the distance between the stagnation plane and the burner. Therefore, it is not possible anymore to obtain a profile of soot properties along the axis with a single simulation, but it becomes necessary instead to run various simulations for each of the considered separation distances between the burner and the stagnation plane (H_p). This leads to an increase in the computational cost, which is well counterbalanced by higher accuracy in describing the flame conditions.

The inlet conditions for the flame are presented in table 5.5.

Equivalence ratio ϕ	C_2H_4 mole fraction	O_2 mole fraction	Ar mole fraction	Cold gas velocity [cm/s]	Pressure [atm]
2.07	0.163	0.237	0.60	8	1

Table 5.5: Inlet conditions for the burner stabilized stagnation flame from Wang et al.[26]

Figure 5.19 shows the temperature profiles along the flame axis for different positions of the stagnation surface with respect to the burner (lower panel). The cooling effect of the stagnation plane is evident; the temperature does not decrease slowly as in a free flame (Figure 5.19, upper panel), but cools down quickly to the value measured on the water-cooled plate. However, the maximum temperature is around 1830 K for all of the positions, therefore the flames are still comparable. The temperature profile has been computed as described in chapter 3, paragraph 3.3, taking into account gas and soot radiation, even if (Figure 3.5) the soot radiation effect is negligible since the flame is lightly sooty.

The model manages to describe the temperature profile within the experimental error. The fluid dynamics is also well described, as seen in chapter 3 through the comparison with the 2D simulations.

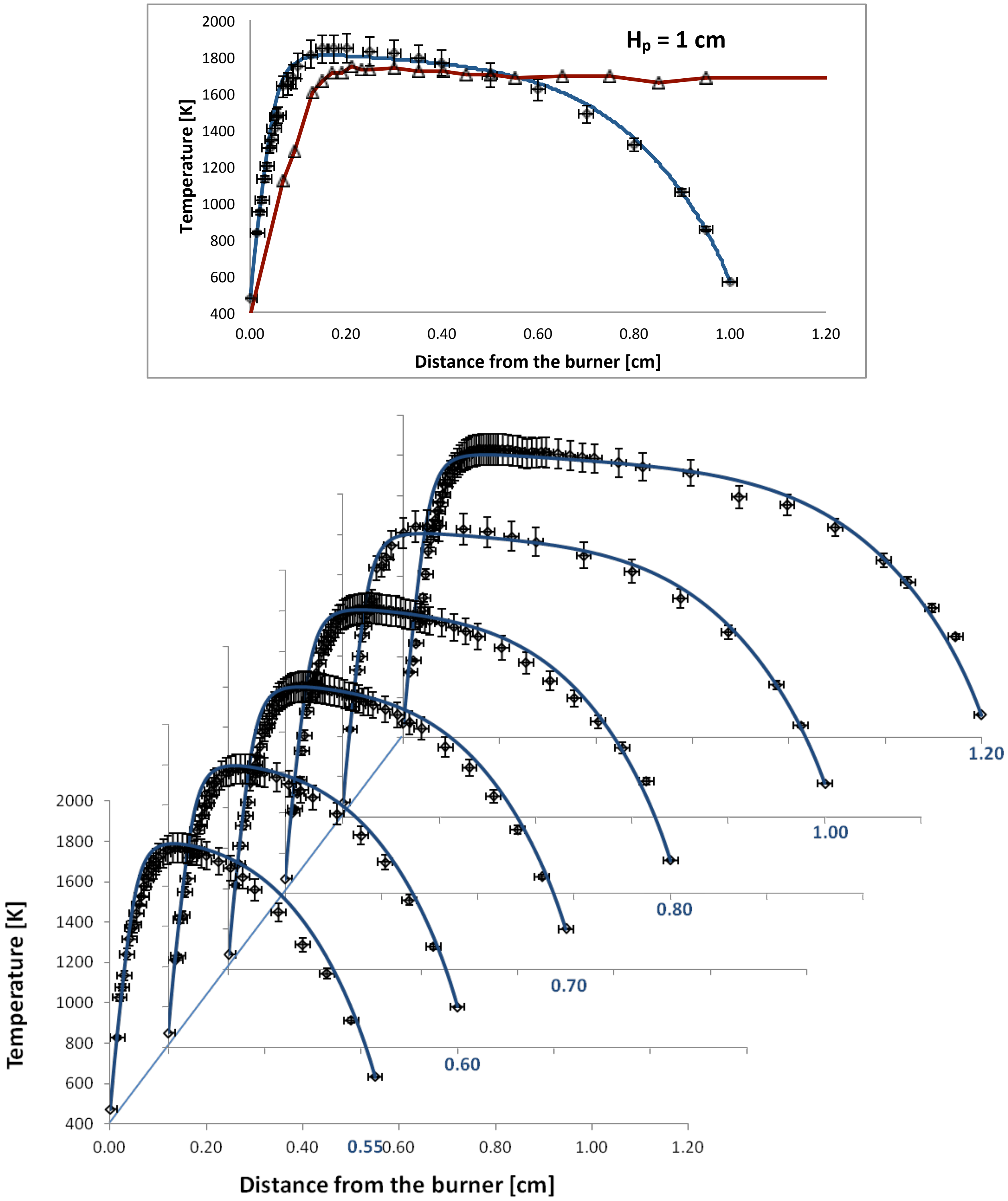

Figure 5.19: Upper panel: free flame temperature profile (red line and triangles) vs BSSF (blue line and diamonds). Lower panel: temperature profiles for different H_p. Diamonds: Measured values; solid lines: computed profiles.

The temperature free flame profile does not decrease sharply as in the BSSF and the residence times are shorter because the velocity does not decrease to zero, therefore if the simulations did not take into account the stagnation surface the surface growth reactions would be overestimated and the coagulation reactions underestimated.

Figure 5.20 shows the comparison between measured and computed values of the soot volume fraction (Figure *a*), number density (Figure *b*) and PSDFs (Figure *c*). Only particles larger than 2.4 nm are considered.

For all of the three features, the trends are well represented. The major contribution to soot volume fraction comes from larger particles, hence it is useful to analyze the model predictions for soot concentration jointly to the right tail of the PSDFs.

The computed soot volume fraction matches quite well the experimental data, especially at larger distances from the burner. As expected, also the right tail of the PSDF is in agreement with the measured values. At lower distances, the model tends to overpredict the concentration of larger particles, and hence of soot. A discussion on the reaction classes that could bring to this overestimation is presented later, together with the sensitivity analysis of the model to the kinetic parameters of these classes.

The number density is mainly determined by the smaller particles, thus it is related to the first mode of the PSDF.

Overall it is slightly overpredicted, apart from the data at 0.8 cm above the burner. The nucleation mode of the PSDF, in fact, is overestimated at larger distances while at lower distances the experimental data show particles up to 10 nm, whereas the model already sees a hint of bimodality.

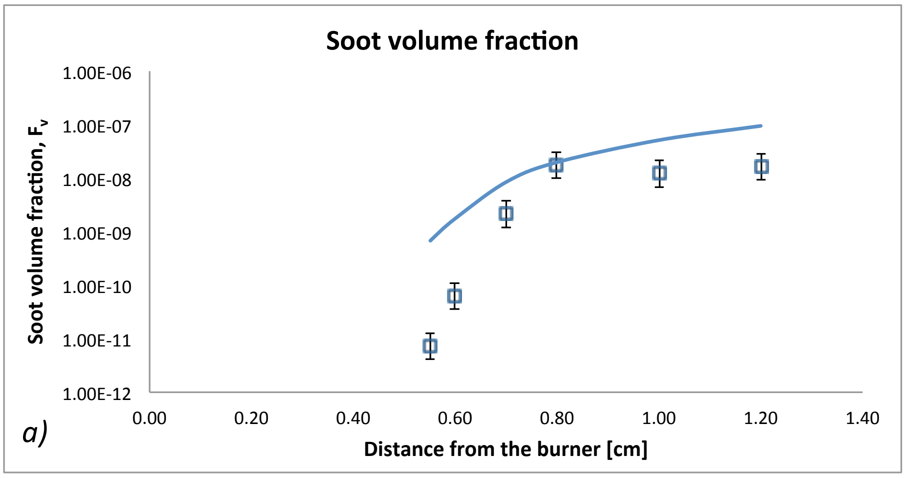

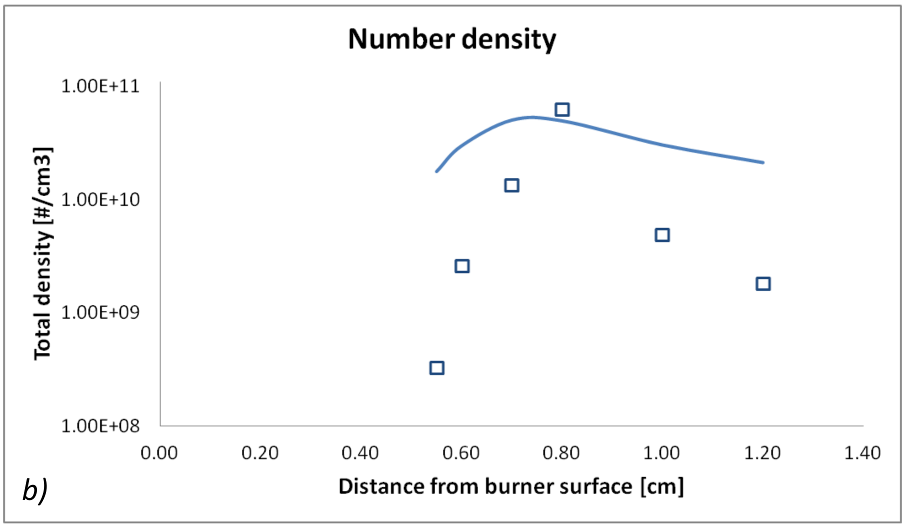

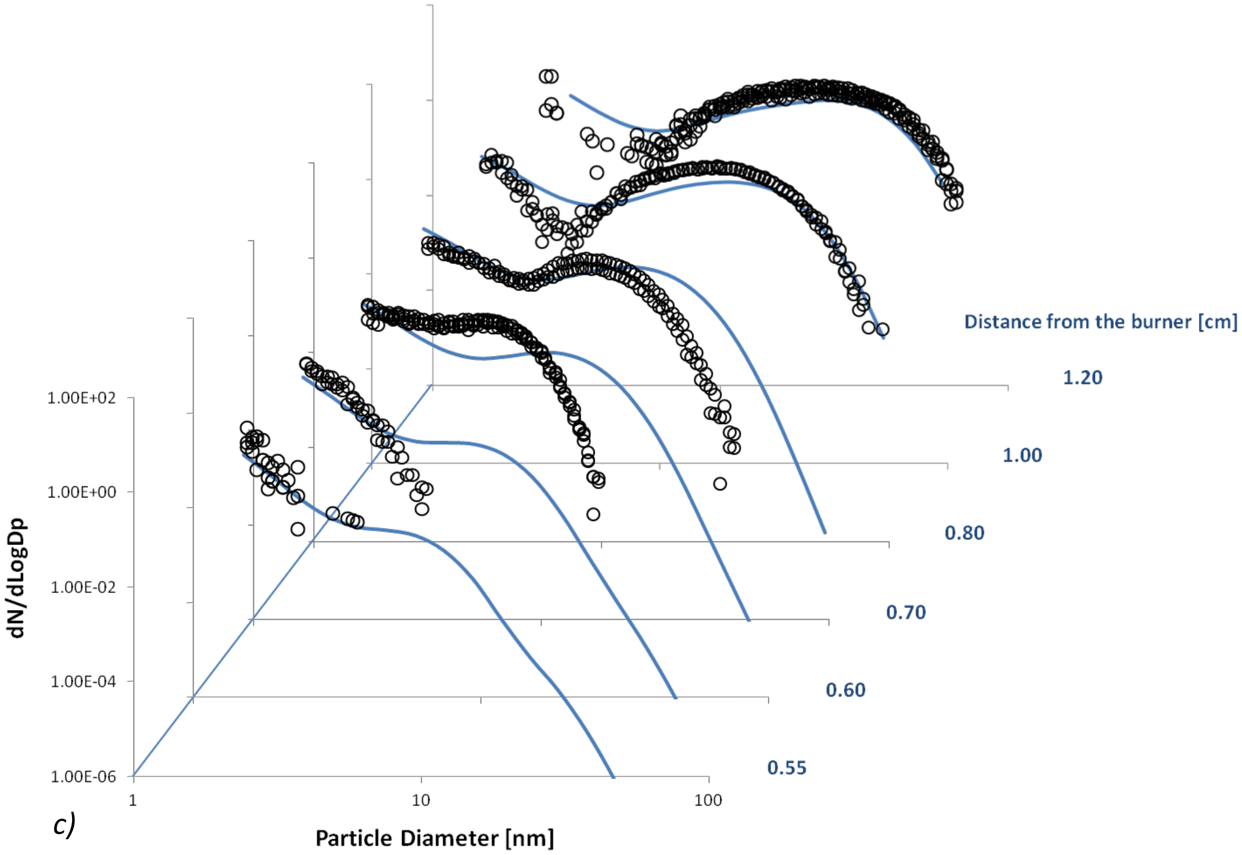

Figure 5.20: Comparison between experimental values (squares and circles) and model predictions (solid lines) of soot volume fraction (Figure *a*), number density (Figure *b*) and PSDFs (Figure *c*)

The accuracy of the model predictions depends on the precision in the description of the phenomena underlying soot formation. In particular, the poor knowledge on the nucleation mechanism, which is the passage from gas to solid phase, determines huge uncertainties on the results. A good approach to understand how the different reactions affect the various soot features and hence be able to tune the model is to carry out a sensitivity analysis to the different reaction classes involved in soot evolution.

In this work the focus is on reactions that are significant for soot growth and coagulation, while the oxidation reactions are not considered.

For the surface growth the HACA mechanism is of primary importance and it is distinguished in HACA1 if it produces a molecular species and hydrogen and HACA2 if it produces a radical and hydrogen. Reactions of PAHs condensation on BINs and those with small resonant radicals C_3-C_5 are also considered through the PAH+BIN and RR reaction classes, respectively. BIN+BIN reactions represent the coagulation process.

To emphasize the effect that each of the reaction classes has on soot features their kinetic constant is multiplied by a factor of 10 and new simulations are run with the modified kinetic scheme. The effects are decoupled; in each simulation only the rate of one class is changed, apart from the joint analysis of the PAH-BIN and BIN-BIN, in which both are increased (indicated as PBeBB).

This sensitivity analysis is carried out on the BSSF with a distance of 1 cm between the burner and the stagnation surface. The results on the soot volume fraction, number density and PSDF are shown in figure 5.21.

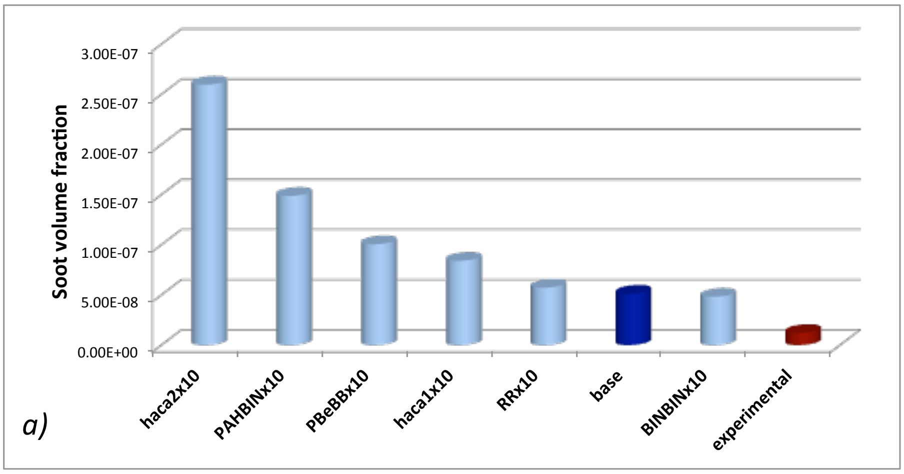

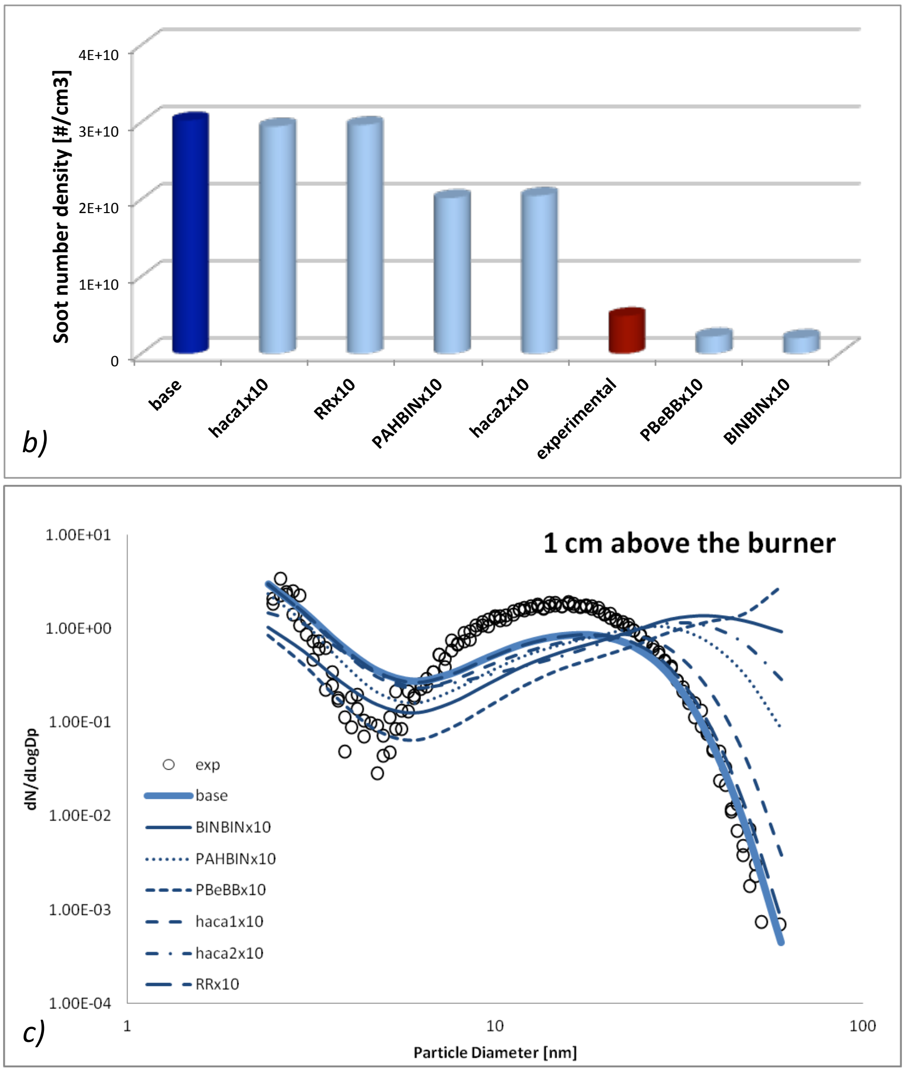

Figure 5.21: Results of the sensitivity analysis: soot volume fraction (Figure *a*), number density (Figure *b*) and PSDF (figure *c*).

All of the reaction classes increase the soot volume fraction with respect to the base scheme, except for the coagulation (BIN-BIN) that leads to a slight decrease. This can be explained in relation to the decrease in the surface area with respect to the volume unit due to coagulation. As for the other cases, the HACA2 mechanism has a more pronounced effect with respect to the HACA1. Enhancing the rate of the condensation reactions (PAH-BIN) also increases soot volume fraction because by enhancing their rate the amount of gaseous species that passes to solid phase is greater.

In line with the soot volume fraction, the PSDF shows an increase in the concentration of the larger particles to the detriment of the smaller ones, because the effect of all the considered reactions is to foster the growth.

By consequence, the number density decreases with respect to the base case in all of the other situations. In fact, the coagulation efficiency is higher for larger particles, thus if the growth is more significant, also the coagulation gains importance and the number density decreases.
Thus, the BIN-BIN reaction has a huge influence because it directly affects the coagulation, while the other classes have an indirect influence. The HACA2 mechanism and the PAH-BIN reactions foster the growth more than the others; thus also the effect on the number density is greater.

The analysis of the model through comparison with experimental data allowed to test in detail the model behavior in the prediction of the key component in soot formation.
The illustrated trends are in agreement with theoretical knowledge and experimental data, confirming the capability to simulate different conditions of temperature, pressure and composition, despite of some discrepancies.
The sensitivity analysis to reaction classes clarifies the weight of the growth and coagulation mechanisms on particulate formation, while a more detailed study has to be carried out on the role of oxidation.

6 Experimental setup and results

In a diffusion flame combustion occurs at the interface between the fuel gas and the oxidizer, thus the controlling phenomenon might be the diffusion rate of reactants rather than the rate of the chemical processes involved. Furnaces and aero turbines' flames are usually diffusive, because fuel and air are not mixed before the ignition, therefore the interest in diffusion flames is mainly related to their similarity with these real devices. In particular, high-pressure combustion is present in many practical applications, hence it is of primary importance to test the models under pressure conditions of practical systems[108]. Thus, establishing a well-controlled high-pressure experiment is desirable to collect reliable data, necessary to tune the models also under these conditions, since the strong dependence of transport properties on pressure and the nonlinearity of Arrhenius kinetics might affect the ability of the model to match experimental data at high pressure. Diffusive coflow flames at high pressure present many issues like instability and this fostered the efforts to stabilize high-pressure counterflow flames. The counterflow configuration is a convenient environment to study soot inception at high pressure in diffusion flames, thanks to controllable soot load, flame stability and the limited computational cost it requires for modeling. Hence a sampling technique has to be developed in order to collect data on soot volume fraction, number density and particle size distribution function.

As the flame structure becomes thinner with increasing pressure (from about 5 mm at 1 atm to 1 mm at 25 atm) flame diagnostics must bring minimal perturbation to the flame structure and have high spatial resolution. For these reasons it was chosen to exploit the thermophoretic effect to collect soot on a thin wire. Thermophoresis, as discussed in Chapter 3, is the phenomenon wherein small particles, such as soot particles, in a gas stream characterized by a temperature gradient ∇T, drift in the direction opposite to that of ∇T.

Inserting a wire into a flame creates a temperature gradient inside the gaseous stream, because, as illustrated in paragraph 6.4, it has radiative losses toward the external environment, therefore its equilibrium temperature is lower than the one present inside the flame.

In analogy with the case of the stagnation plane simulated in chapter 3.5 the thermophoretic force acting on the particles is directed toward the wire and this generates a flux of soot particles that deposit on top of it. Afterwards the wire can be analyzed under some microscopes and all the information on soot distribution can be inferred by the images if the residence time is chosen accurately so that the coverage is sparse and the single particles can be seen and are not overlapping. An overview of the different imaging techniques that might be used is given in paragraph 6.3 with a comparison of the resolution that each of them can reach and the information obtainable from the analysis.

The thermophoretic phenomenon has been extensively studied and used for similar purposes, for example in thermocouple particle densitometry (TPD), a method for measuring absolute soot volume fraction in flames which was suggested by Eisner and Rosner[109].

In particular, thermophoretic sampling has been exploited by D'Anna and coworkers[92,100,110,111] to measure the particle size distribution in premixed laminar flames. In their studies, a mica disk was inserted at controlled residence time into the flame by means of a double acting pneumatic cylinder and atomic for microscopy (described in paragraph 6.3.3) was used to obtain quantitative information.

In the high-pressure configuration, however, it is not possible to use a disk, because at 25 atmospheres the soot region is only about 400 µm thick, hence a plate or a thick wire would be too intrusive to follow the evolution of the particles with high spatial resolution. Ideally, the wire should not be thicker than 100 µm to sample at 25 atm.

Since a wire is substantially different from a flat plate, both for fluid dynamics conditions in the boundary layer and temperature, the technique has to be validated.

For this purpose it was chosen to work with an atmospheric laminar premixed ethylene flame, because it is similar to the reference C3 flame studied by Hai Wang and coworkers[66,67] and it has been widely studied with different techniques. Also, working at atmospheric pressure allows to avoid all the problems related to high pressure; for example, wires of different sizes can be used to compare the information obtained with the thin ones and if the position of the sample in the flame changes by some microns this does not sensibly affects the observed particle size distribution.

The first question that arises when considering the thermophoretic sampling is if what we see on the wire corresponds to the real particles in flame. Indeed, some artifacts might affect the results obtained: the particles deposited on the wire might interact with the surrounding flame environment once deposited, and this would prevent to observe their original structure, shape and size.

In the region where nascent soot can be found the flame environment is rich in acetylene, reactive radicals, PAHs and other heavy condensable species, thus there are mainly two kinds of artifacts that could affect the particle size distributions (PSDs): particle growth by surface reactions on the wire and with the substrate itself (if the wire is above 1400 K) or by condensation (if the wire temperature is well below). In the former case, particles do not cool down once they reach the surface and they continue to grow by reaction with gas phase species. In the latter case heavy PAHs and condensable species[104] with low vapor pressure can condense on the cold substrate on top of the particles of interest, hence altering the distribution.

A first evidence of artifacts can be obtained by sampling on the same substrate for different residence times. In fact, if there is any growth on the wire due to chemical reactions or condensation, the PSD should shift toward higher diameters at longer residence time.

As the diameter of the wire increases, its temperature drops because more heat is radiated by the surface to the surroundings. Accordingly, if a wire is thick enough, its surface attains such a temperature that all the surface reactions are frozen. Another indication of artifacts might be inferred by sampling on colder and hotter substrates in the same flame conditions. If the PSDs on the thicker wires are different from those on the thinner ones, it can be inferred that growth reactions play an important role on the latter.

Initially, the best substrate in terms of perturbation of the flame and resistance was thought to be a 13 µm diameter silicon carbide wire. The final goal of the experimental activity was hence to validate the use of the 13 µm silicon carbide by analyzing the morphology of the particles and particle size distribution on different substrates or on the same substrate at different residence times.

In this chapter, after the description of the experimental setup, the equations underlying the thermophoretic effect are presented. They justify the use of the technique by demonstrating that the thermophoretic force, in the conditions under analysis, is independent from the particles' size. The possible microscopy techniques are discussed and for each of them different characteristics of the substrate are required, narrowing down the choice of possible materials.

Since the wire temperature is important to determine the possible interactions with the flame, the equations used for its calculation and the assumptions made are shown in paragraph 6.4, before the presentation and discussion of the results on the silicon carbide wire.

Particles on this substrate were actually growing, therefore it was decided to sample on a colder substrate, to eliminate the possibility of chemical growth. The logic behind the search of the new material is presented in paragraph 6.7 and the results on the colder substrate, also affected by growth, are shown.

Even though quantitative data could not be obtained, it was still possible to gather important information about morphology, in line with the literature. The flame was also simulated, to analyze the information inferred from the experimental activity with the expected results.

6.1 EXPERIMENTAL SETUP

An ethylene premixed laminar flame at atmospheric pressure over a flat flame burner was set up.

The flat flame burner has an inner diameter of 5 cm and an outer ring for a Nitrogen shroud to stabilize the flame.

Oxygen flow is controlled by a rotameter UCC P/N FM 4334, Ethylene flow by a rotameter Brooks R-2-15B, Nitrogen flow by a United Mass Flow controller 1100. The box controlling the MFC is a MKS 247D.

The wire is inserted into the flame by means of a pressurized air piston; it is thrust horizontally like a needle in case of rigid substrate, while in case of the thin silicon carbide substrate a fork is been used to hold it tense. The wire passes through a hole in a metal shield before entering the flame, to prevent the air moved by the piston to perturb the flame (Figure 6.1).

The residence time is measured with a high-speed camera Phantom V 7.3, with time resolution of a millisecond.

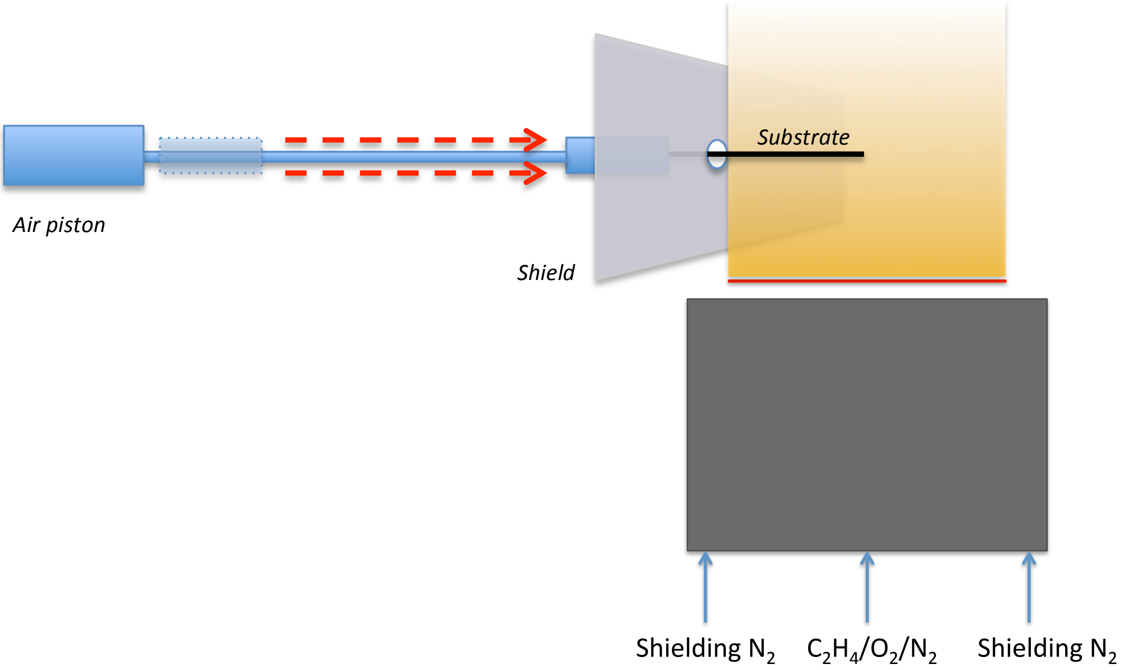

Figure 6.1: Schematization of the experimental setup.

The flame chosen for the study has the inlet characteristics shown in table 6.1:

Equivalence ratio	Dilution (N_2/C_2H_2)	Cold gas velocity [cm/s]	Maximum Temperature
2.1	6.5	6.5	1651 (±40) K

Table 6.1: Flame characteristics. Cold gas velocity is at 298 K, 1 atmosphere

Nitrogen flow is 5.57 l/min, Oxygen 1.23 l/min and Ethylene 0,86 l/min.

As mentioned earlier, it is important to have a sparse coverage on the substrate, because to analyze particles they cannot be overlapping, otherwise it becomes impossible to measure their size. The particles' mass flux towards the wire depends mainly on two parameters, as described mathematically in the next paragraph: the soot volume fraction and the ratio between the wire and the gas temperature. Thus, if the wire is thicker, and therefore colder, the thermophoretic force becomes stronger and the substrate gets fully covered faster. The other parameter we can play with is the soot volume fraction, easily controllable by changing the inlet composition.

This explains the choice of the inlet values for the flame under consideration. In fact, it is an incipient sooting flame; the soot volume fraction is quite low (the simulation indicates a maximum of about 10^{-7}) and a proper coverage of the wire can be reached with reasonable residence times.

Furthermore, these sampling conditions allow to avoid aggregates at low height above the burner, undesired both because the interest lies mainly in the early process of the soot formation and because it becomes very difficult to measure their volume.

6.2 THERMOPHORETIC MASS FLUX

It is of primary importance to describe the thermophoretic mass flux to verify if the assumption of thermophoretic force independent from the particle's size is acceptable.

The following conditions must be satisfied:

- Low Reynolds number, acceptable since the system under study is a laminar flame;
- Spherical particles in free molecular regime (Knudsen number $Kn = \lambda/L$>>1, where λ is the mean free path and L is the characteristic length of the particle). This is also verified since the maximum dimension of the aggregates is far less than 1 µm, which is a threshold value.

It follows that Stokes number is well below the critical one. Stokes number is defined as:

$$Stk = \frac{\tau\, U_o}{d_c}$$

Where τ is the relaxation time of the particle, U_o is the fluid velocity of the flow well away from the obstacle and d_c is the characteristic dimension of the obstacle (typically its diameter). In case of Stokes flow, when the particle Reynolds number is low enough that the particle drag coefficient is inversely proportional to the Reynolds number itself, the characteristic time of the particle can be defined as:

$$\tau = \frac{\rho_d\, d_d^2}{18\, \mu_g}$$

Where ρ_d is the particle density, d_d is the particle diameter and μ_g is the gas dynamic viscosity.

For large Stokes number the particles' inertia dominates, thus they will continue along their initial trajectory when the stream encounters an obstacle, whereas at low Stokes number, like in this situation, particles follow fluid streamlines[112].

Therefore, particles follow the streamlines around the wire and do not deposit inertially, but just by thermophoresis or Brownian diffusion[113].

As explained in chapter 3, paragraph 3.2, the thermophoretic diffusivity ($\mathrm{D_T}$) for soot can be expressed as:

$$\mathrm{D_T} = \left(\frac{3}{4}\right)\left[1 + \left(\frac{\pi}{8}\alpha\right)\right]^{-1} \nu$$

In this case ν, the momentum diffusivity of the prevailing gas mixture, can be calculated assuming N_2 as the only species present, since it is the most abundant species (≈73% in the initial mixture) and some cancellation occurs for the contribution of H_2O and CO_2 having, respectively, lower and higher diffusivity than N_2[114].

The thermophoretic mass flux of particles to the wire per unit time and surface area can be written as[109]:

$$\gamma = \left(\frac{D_T\, Nu_w\, f_v\, \rho_p}{2d_w}\right)\left[1 - \left(\frac{T_w}{T_G}\right)^2\right]$$

With:

- f_v local soot volume fraction (constant during the whole sampling, since the flame is steady state)
- ρ_p intrinsic density of the soot particles
- Nu_w Nusselt number for heat transfer around the wire
- d_w wire diameter
- T_w wire temperature
- T_G gas temperature

McEnally et al. measure[113] how the wire temperature (T_w) changes in time.

With the technique under analysis, the sampling stops before reaching a full coverage of the surface, therefore the diameter can be assumed constant throughout the whole sampling procedure (hence there are no changes in temperature due to the variation of the diameter and consequently of the radiation emitted).

It is then possible to work under the assumption that after the transient-response stage the wire temperature is constant.

The formulas confirm that the thermophoretic force does not depend on the particles' diameter in the working conditions; it is therefore possible to study the particle size distribution function (PSDF) by thermophoretic sampling.

6.3 MICROSCOPE ANALYSIS AND SUBSTRATE CHARACTERISTICS

Once particles are collected they can be analyzed under the microscope to draw a PSDF and verify the presence/absence of artifacts.

Different microscopes can be used: scanning electron microscope (SEM), transmission electron microscope (TEM) and atomic force microscope (AFM).

In order to understand the characteristics required for the substrates and the issues relied to the different techniques a brief description of the different microscopes is needed.

6.3.1 Scanning Electron Microscope

The Scanning Electron Microscope (SEM) is a special type of electron microscope that produces images of a sample by scanning it with a focused beam of electrons. It is one of the most commonly used electron microscopes for the examination of microstructures and their morphology. The microscope uses a focused beam of high-energy electrons that hitting the surface of the sample generates a variety of signals, including secondary electrons (SE), back-scattered electrons (BSE), characteristic X-rays, light (cathodoluminescence) (CL), specimen current and transmitted electrons that can be analyzed. Optical lenses are installed to enlarge the visual angle and it is also possible to obtain compositional and orientation data on the sample. Basically, in a scanning electron microscope a small beam of electrons (of the order of ~10 nm) scans the surface of a sample, while the subsequent interactions of the electrons with this sample are further analyzed by several detectors as shown in the schematization of the tool (Figure 6.2). In the most common or standard detection mode, the secondary electron imaging (SEI), the SEM can produce very high-resolution images of a sample surface, revealing details less than 1 nm in size. Due to a very narrow electron beam, SEM micrographs have a large depth of field yielding a characteristic three-dimensional appearance useful for understanding the surface structure of a sample. Also the intensity of back-scattered electrons (BSE) is normally evaluated because the signal is strongly related to the atomic number (Z) of the specimen; BSE images can then provide useful information about the distribution of different elements in the sample. The source of electrons is usually a tungsten filament or a field emission gun. The electrons emitted are focused by a series of electromagnetic lenses and accelerated to an energy in the range of 1-30keV. Subsequently, scan coils deflect the beam to direct it to a specific position on the sample[115].

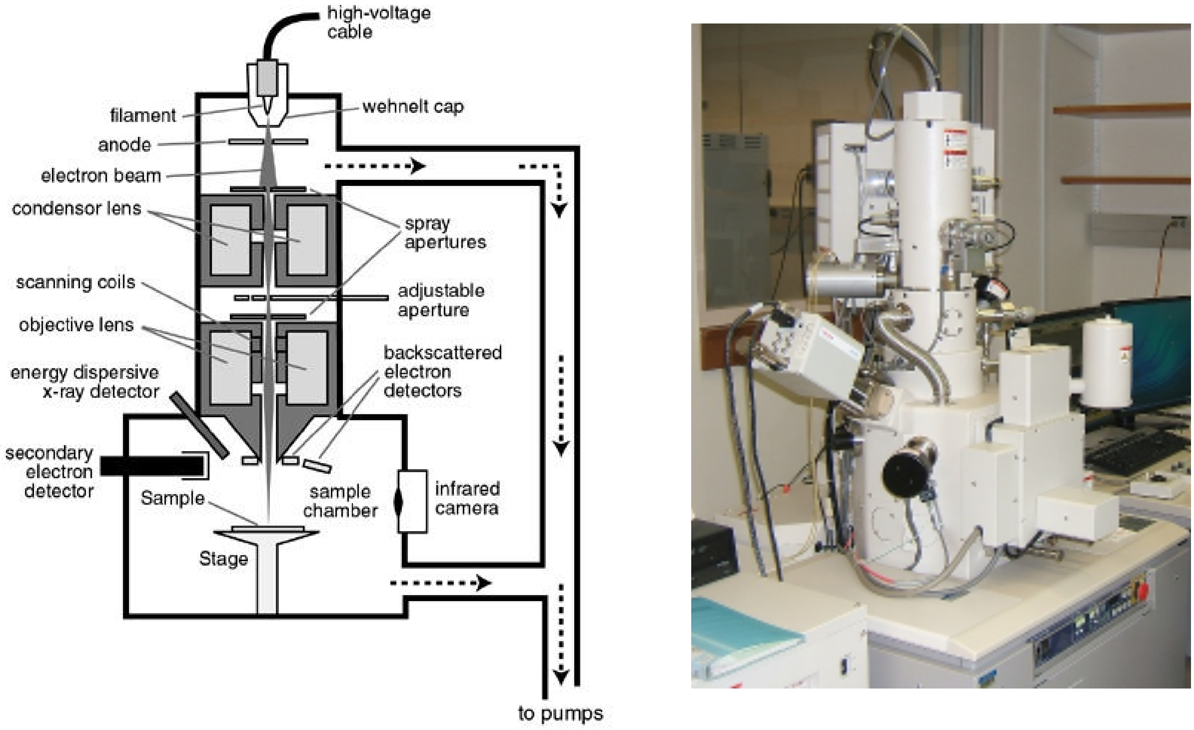

Figure 6.2: Schematization of SEM and picture of the Hitachi SU-70 SEM in the YINQE, Yale University[116]

Figure 6.3 shows typical images of soot particles obtainable under the SEM.

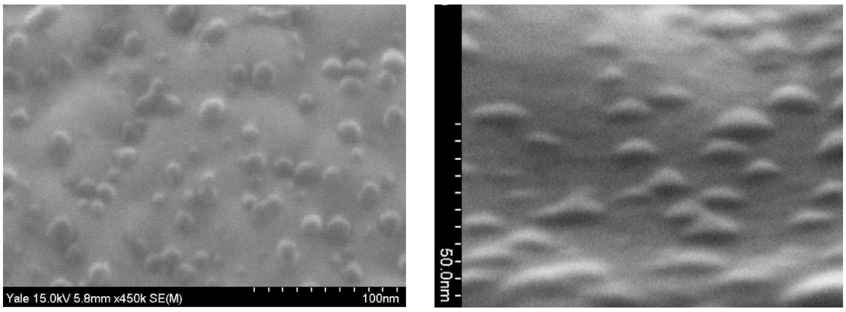

Figure 6.3: SEM image of soot particles on silicon carbide viewed from the top (left panel) and from the side (right panel)

6.3.2 Transmission Electron Microscope

The transmission electron microscope (TEM) operates on the same basic principles as the light microscope but uses electrons instead of light. The resolution with a light microscope is limited by the wavelength of light. TEMs use electrons as "light source" and their much lower wavelength makes possible to get a resolution a thousand times better than with a light microscope.

A high-energy monochromatic and coherent beam of electrons is transmitted through vacuum in the column of the microscope. Electron lenses are used instead of optical ones; they usually use electromagnetic coils to generate a convex lens that focuses parallel rays at some constant focal length. The focused beam of electrons passes then through an ultra-thin specimen (less than 200 nm), interacting with the latter as it passes through it[117]. These electrons are scattered at different angles depending on the density of the atoms encountered. At the bottom of the microscope the unscattered electrons hit a fluorescent screen, which gives rise to a “shadow image” of the specimen with its different parts displayed in varied darkness according to their density[118]. The image can then be captured by a camera (Figure 6.4).

One of the most important advantages of TEM over other characterization techniques is that information can be obtained both from direct and indirect space. In direct space, two modes are typical, i.e. TEM and High Resolution TEM (HRTEM), which can discern the structure and morphology of a material thanks to the high magnification and high resolution allowed by this technique. In indirect space, diffraction yields information on the cristallinity of the specimen. Besides these possibilities, chemical information can also be acquired using the inelastic interaction of the incoming electrons with the atoms of the specimen. Here two techniques are typical, i.e. electron energy loss spectroscopy (EELS), and energy dispersive X-ray spectroscopy (EDS).

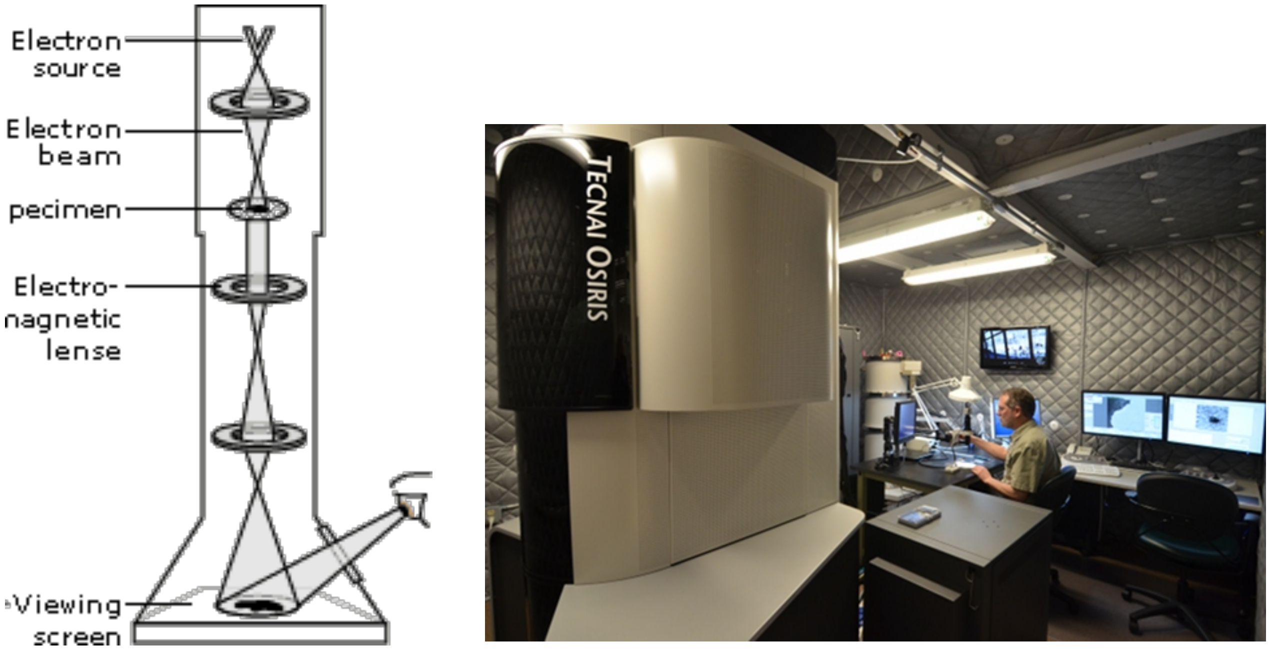

Figure 6.4: Schematization of the internal structure of a TEM and picture of the FEI Tecnai Osiris 200kV TEM in the YINQE, Yale University[116].

Figure 6.5 shows how TEM allows to observe particles on the wire only from the side.

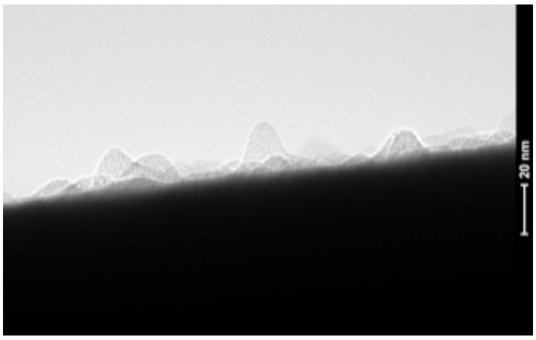

Figure 6.5: Side view of soot particles on sapphire wire.

6.3.3 Atomic Force Microscope[119]

Atomic force microscopes are devices that allow to measure surface structure with great resolution and accuracy; they operate differently from most microscopes, because they don't form an image by focusing light or electrons or a surface. Instead, they have a cantilever with a sharp tip that interacts physically with the sample, building up a map of the height of the sample's surface (Figure 6.6).

Piezoelectric materials, that convert electric potential into mechanical motion, are used to control the motion of the probe. In fact, when a potential is applied across two opposite sides of the piezoelectric device, it changes geometry. The force between the probe and the surface is measured with a force transducer. When the probe comes into contact with the surface, the voltage output from the transducer, that is usually a cantilever with integrated tip (the probe) and an optical lever, increases. Feedback control is used to maintain a given force between the probe and the sample, thus, if the force increases because the tip encounters a higher feature of the surface, the feedback control makes the piezoelectric move the probe away from the surface.

The topography of the surface can be reconstructed by measuring the movements of the probe, assuming that the tip-sample distance is fixed.

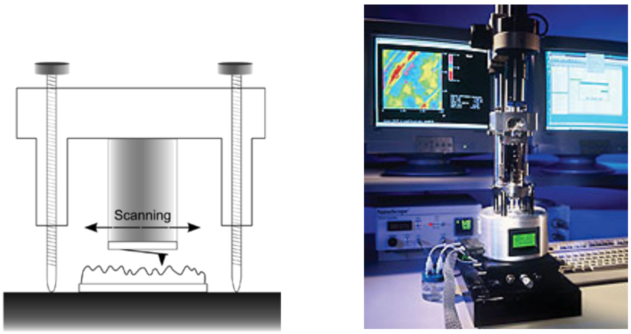

Figure 6.6: Schematization of an AFM scanning[119] and AFM equipment (Bruker, Digital Instruments, multimode AFM) in the YINQE, Yale University[116].

It can be perceived that usage of AFM is not intuitive, but it requires instead a deep knowledge of the functioning to set the parameters and obtain reliable information.

All AFM images are a convolution of the topography of the sample with the shape of the tip of the probe. Therefore, a deconvolution has to be made to see the "real" shape of the object. But the tip's shape and size are never precisely known; hence the mathematical formulas cannot represent the real situation. For example, a sphere on a substrate could look like a droplet splashed on the surface with the wrong deconvolution, or it might seem to have a bigger diameter. But this information is very important in the study of morphology and size of soot particles. To minimize the artifacts, the tip should be finer than the features being analyzed, and in this case a carbon nanotube-tip would be needed to fulfill this requirement, but this is advanced AFM technique that can only be done by an AFM expert.

The analysis on the samples was run with the tapping mode, in which the tip does not touch the surface, but vibrates over it and the topography of substrate can be determined by the electrostatic interactions. Depending on the settings chosen the results can change a lot and it is a non-trivial operation to choose these settings. For example, one of the parameters to be chosen is the spacing between one scanning line and the other: if it is too large, then the information collected makes no sense, because if a particle has a diameter of about 5nm, a scanning distance of 2 nm would not give a good reconstruction. However, a thicker scanning takes a very long time, and therefore it becomes impractical.

Some issues encountered during the sampling on sapphire with the AFM in YINQE (Yale Institute for Nanoscience and Quantum Engineering) are here presented.

During data processing the choice of interpolation between the data and most of the methods to flatten the background could bring to significant changes in the volume of the particles. Figure 6.7 presents the topography of a sample reconstructed with AFM before and after processing the data with Gwyddion[120], an Open Source software built for analysis of height fields.

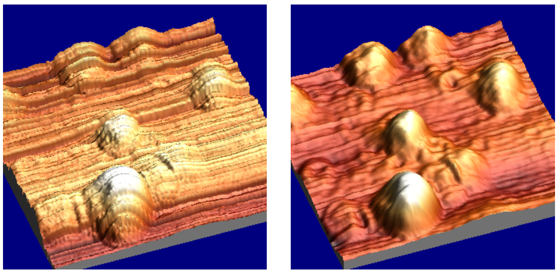

Figure 6.7: AFM image of soot particles on sapphire before (left) and after (right) processing the raw data. Scanning area 180nm x 180nm

Thermal drift is another possible artifact, observed also on the sapphire (Figure 6.8). The appearance of all the particles is distorted and if their shape is not known before, it is hard to detect the presence of thermal drift. After the machine is stabilized (about half an hour) this issue should disappear but this means adding time to a procedure that is already extremely long.

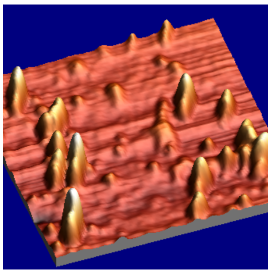

Figure 6.8: Effect of thermal drift on the sapphire sample. Particles' base area is elongated in one direction. Scanning area 500nm x 500nm.

6.3.4 Comparison of the microscopes

It is evident that AFM technique cannot be used as a fast, reliable and simple method, but it was used to check consistency in particles' morphology seen with the other techniques.

	AFM	**SEM**	**TEM**
Sample preparation	little or none	from little to a lot	from little to a lot
Resolution	0.1 nm	5 nm	0.1 nm
Relative cost	low	medium	high
Sample envinonment	any	vacuum(SEM) or gas (environmental SEM)	vacuum
Depth of field	poor	good	poor
Sample type	Conductive or insulating	conductive	conductive
Time for image	2–5 minutes	0.1–1 minute	0.1–1 minute
Maximum field of view	100 µm	1 mm	100 nm
Maximum sample size	unlimited	30 mm	2 mm
Measurements	3 dimensional	2 dimensional	2 dimensional

Table 6.2: Summary of the main features of AFM, SEM and TEM[119]. SEM Hitachi SU-70 in YINQE is actually one of the highest resolution SEMs available today providing 1nm resolution.

Considering the characteristics of the different microscopes (table 6.2), it was decided to measure the particles' equivalent diameter from the SEM picture, assuming particles as spherical. Actually, since particles are not spherical, the longest diameter of the ellipsoidal base was the measured one, hence keeping a consistency between the measurements.

Regardless of this rough assumption (non representative of the real morphology of the particles) that prevents from knowing the real size of the particles, the equivalent diameter still allows to detect relative shifts of the PSD because of internal consistency on how it was determined.

The size of the smaller nascent soot particles is below the capability of the SEM (pushing its resolution to the lower limit particles with a diameter around 5 nm are in fact visible, but it is possible to get a clear view only when the particle is around 10 nm or more), since in previous studies particles with a diameter as small as 1.4 nm have been detected[66,121,122].

Another limit of the SEM is that it is not possible to detect the true size of the particles, as previously stated.

Anyway SEM is still a very useful tool, because it is easy to use and it allows for a quick screen of the samples, for example when looking for the right conditions to use to have the proper coverage. It can also be used to detect the presence of artifacts, because when sampling under suitable conditions (height above the burner, residence time and in an incipient sooting flame, like the chosen reference one) it is still possible to detect relative shifts of the particle size distribution relatively easily and with a high confidence level in the measurements with respect to the AFM.

While SEM is very practical to look for possible artifacts, TEM is a powerful tool to study particle morphology.

In literature particles were collected on a membrane and then analyzed under TEM. Here, instead, using a round wire it is possible to look at the edge to have a lateral view of nascent soot particles, and this allows not only to gather information about their shape and hence to see if they are liquid-like, but also about their structure (amorphous vs. structured) from the atoms interference fringes.

Although it is possible to see even the smallest particles with the TEM (and it would be possible to calculate a volume assuming the base area as circular and the particle as an ellipsoid, knowing the base diameter and the height from the side view), it is not practical to use this tool to calculate a PSD. In fact, for every particle it is necessary to rotate the sample to find the position in which it is perfectly on the edge, so that the whole particle can be seen. This process is time consuming, and it would take too long to repeat it for a number of times sufficient to draw the PSD.

6.3.5 Characteristics of the substrates

The wire needs to be:

- Inert with respect to the soot growth process. For this reason it is better to avoid metals, because they could act like catalysts
- High-temperature resistant
- Carbon-free (or containing carbon in a stable form): to prevent artifacts due to reactions of the wire itself in the flame
- Conductive: or semi-conductive, so that it can be analyzed under the SEM
- Thin, to allow high spatial resolution even at high pressure

6.4 WIRE TEMPERATURE

Combining the heat transfer equations for a cylinder in cross-flow and the energy balance around the wire, it is possible to calculate the radiation correction, which is the difference in temperature between the flame and the wire due to radiative heat from the wire to the surroundings.

The energy balance for a wire in a gaseous stream can be expressed as:

$$m_W \, C_{P_W} \, \frac{dT_W}{dt} = h \, A \, (T_G - T_W) - \sigma \, A \, \varepsilon \left({T_W}^4 - {T_S}^4 \right)$$

Where m_w is the mass of the wire, C_{Pw} the specific heat of the wire [J/(kg K)], h the convective heat transfer coefficient [W/(m^2 K)], A the heat exchange surface, T_G and T_W the gas and wire temperature, respectively, and T_S is the surroundings temperature (room temperature).

The surroundings temperature is negligible when compared to the wire temperature elevated to the power of four.

The convective heat transfer coefficient can be expressed as:

$$h = \frac{Nu \, k}{D}$$

Where Nu is the Nusselt number, k the thermal conductivity of the material [W/(m K)] and D the wire diameter.

For a cylinder in cross-flow the convective heat transfer varies with the Reynolds (Re) and Prandtl (Pr) numbers, hence the Nusselt number is commonly expressed as:

$$Nu = (C_1 + D_1\, Re^{n_1})Pr^p$$

With all properties calculated at film temperature ($T_f = ½\ (T_w + T_G)$).

The Reynolds number is defined as:

$$Re = \frac{\rho\, u\, D}{\mu}$$

Where ρ is the gas density [kg/m^3], u the gas velocity [m/s] and µ the dynamic viscosity [Pa s]).

The Prandtl number is the ratio of momentum diffusivity (µ/ρ) and thermal diffusivity ($k/(\rho\ C_P)$):

$$Pr = \frac{C_P\, \mu}{k}$$

C_P is the specific heat of the wire [J/(kg K)] and C_1, D_1, n_1 and p are constants.

It has been seen experimentally that the exponent p is between 0.3 and 0.4 and the lower value is the most commonly used.

For air, Pr can be considered approximately constant and with the value 0.7[123], hence we obtain:

$$Nu = C_2 + D_2\, Re^{n_1}$$

The Nusselt number is here calculated according to L. V. King parameters derived by his experimental data[123,124]:

$C_2 = 0.40$

$D_2 = 0.48$

$n_1 = 0.5$

Since the nitrogen, inert with respect to the combustion reactions, is the most abundant species, the flow velocity in the flame can been calculated neglecting the change in the moles' number, taking into account only the temperature effect:

$$u = u_0 \frac{T_{flame}}{T_0}$$

u_0 and T_0 are the cold gas parameters.

Nitrogen is more than 72% of the gas in the flame, hence the gas is considered to be pure nitrogen and the flame temperature is taken as the maximum temperature in the flame (1682 K, as presented later).

6.5 FLAME TEMPERATURE PROFILE

The flame temperature profile is calculated with OpenSMOKE and the kinetic scheme HT1306s as the profile of a premixed flame taking into account the effects of gas and soot radiation.

The experimental profile is not well defined yet since measuring it in a sooty flame is a non-trivial issue. Anyway, the calculated profile well agrees with the currently available data.

The soot radiation does not play a fundamental role in temperature calculation under these flame conditions, because the flame is lightly sooty and the soot volume fraction is very low. The simulations run without the soot radiation, in fact, confirm that the two temperature profiles with or without soot radiation are identical.

The samples have always been collected further than 0.5 cm from the burner surface; figure 6.9 clearly shows that the temperature profile flattens after the initial steep increase; therefore it is an acceptable assumption to take the maximum flame temperature to calculate the wire temperature.

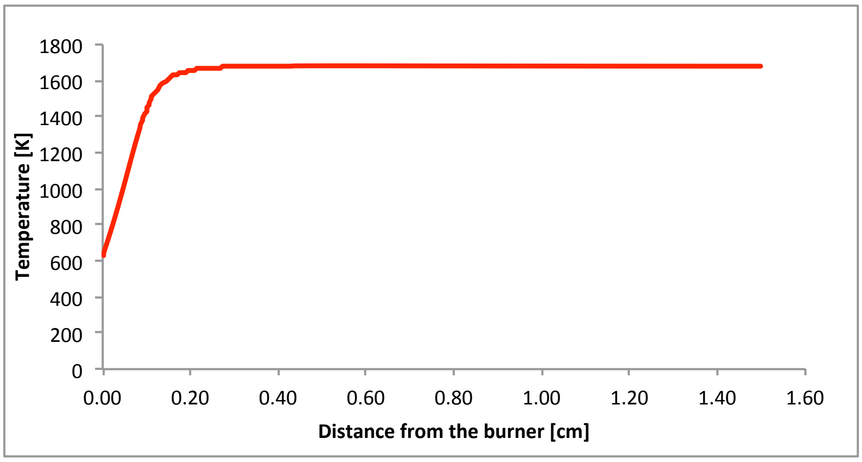

Figure 6.9: Calculated temperature profile of the flame used for sampling.

6.6 PARTICLE SIZE DISTRIBUTION ON SILICON CARBIDE

The substrate under analysis is a Silicon Carbide wire with a diameter of 13 µm. The calculated temperature dynamics for the substrate is shown in figure 6.10.

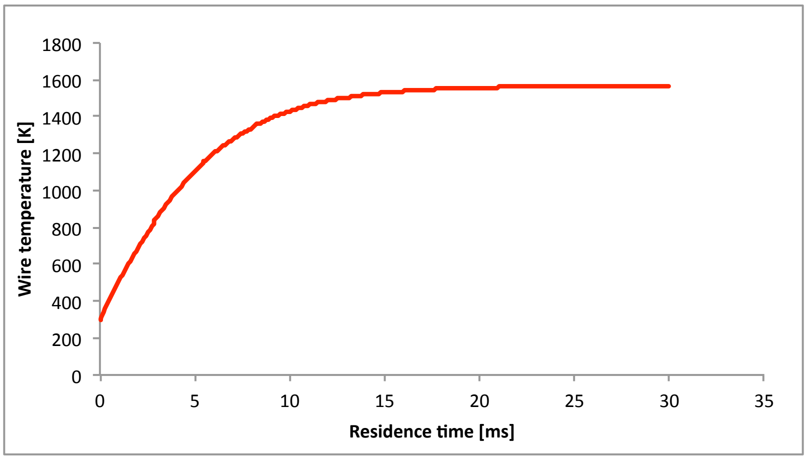

Figure 6.10: Temperature dynamics of the silicon carbide wire in the flame.

As already discussed, any possible growth should be chemical, because the temperature is too high to allow species to condensate.

The shorter residence time on the wire is such that enough particles are collected but the coverage of the wire is very sparse. In fact, if the residence time is too long particles deposit one on top of the other and they cannot be distinguished under the SEM. In this case, residence times range from 60 to 230 ms.

The samples are collected from the same flame at different residence times to observe possible chemical growth. The procedure is repeated at three different heights above the burner to check the consistency of the results along the flame axis. In table 6.3 the sampling distances from the burner are presented.

	Distance from the burner [mm]
Height 1	13.3
Height 2	11.3
Height 3	9.5

Table 6.3: Heights above the burner where the samples were taken.

The error associated to the diameter's measurement is ±1 nm. The error associated to the height above the burner is below 0.05 mm when considering the absolute position, but it is even smaller considering that within a sampling session at a given height the piston apparatus is not moved; therefore the only imprecision in positioning comes from the small vibrations of the wire.

6.6.1 Height 1: sampling results at 13.3 mm above the burner

The first results presented are from samples taken at 13.3 mm above the burner. This is a "threshold height", because aggregates start to form moving further away from the burner, preventing us from obtaining the desired information on nascent soot particles.

In table 6.4 the sampling results for each residence time are summarized, with the calculated mean diameter and the relative standard deviation. The mean diameter is calculated on the basis of a numeral average.

Residence time [ms]	Mean diameter [nm]	Standard deviation
64	11.4	3.0
81	11.4	2.9
107	13.0	2.7
122	13.6	3.6
155	13.9	4.6
194	15.6	3.9
224	16.9	4.1

Table 6.4: Summary of the sampling results at 13.3 mm above the burner

It is useful to plot the mean diameter against the residence time of the substrate in the flame (Figure 6.11), because it highlights the increase of the mean diameter. The cumulative size distribution and the PSDF (Figure 6.12 *a* and *b*, respectively) give the full information on how particles are distributed among the various diameters. In fact, not only the mode of the distribution shifts to higher diameters with increasing residence time, but also the number of small particles decreases and the maximum particle's size found at longer residence times is larger than the one found at shorter residence times.

This can be interpreted as a further confirmation of the growth, because it is consistent with a mechanism for which particles keep depositing on the wire during the whole sampling, but older particles continue to grow. In fact, the smaller particles found also at long residence times could be the younger ones deposited later. The maximum size increases because if the residence time is longer the first particles deposited have more time to grow.

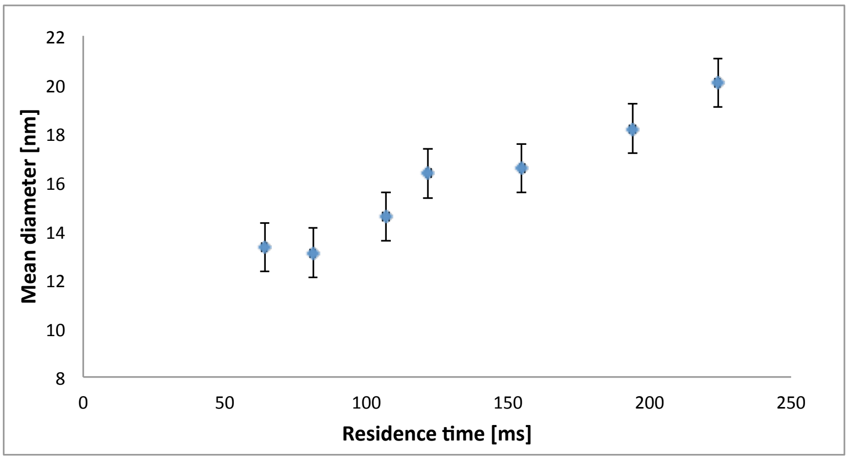

Figure 6.11: Change of the mean diameter with residence time at 13.3 mm above the burner

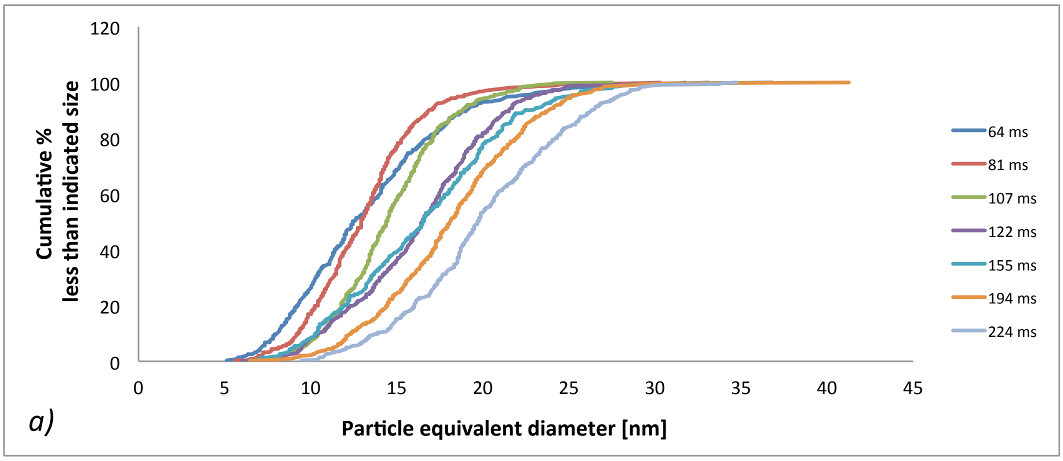

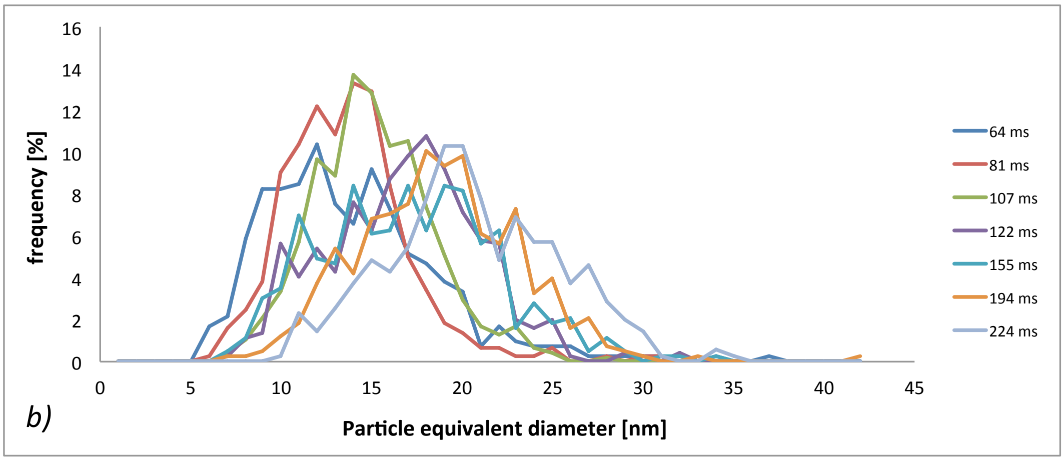

Figure 6.12: Cumulative particle size distribution (figure *a)* and PSDF (figure *b*) at 13.3 mm above the burner.

Some of the SEM images used to draw the particle size distributions are presented in figure 6.13: the change in the size distribution can be noticed also qualitatively.

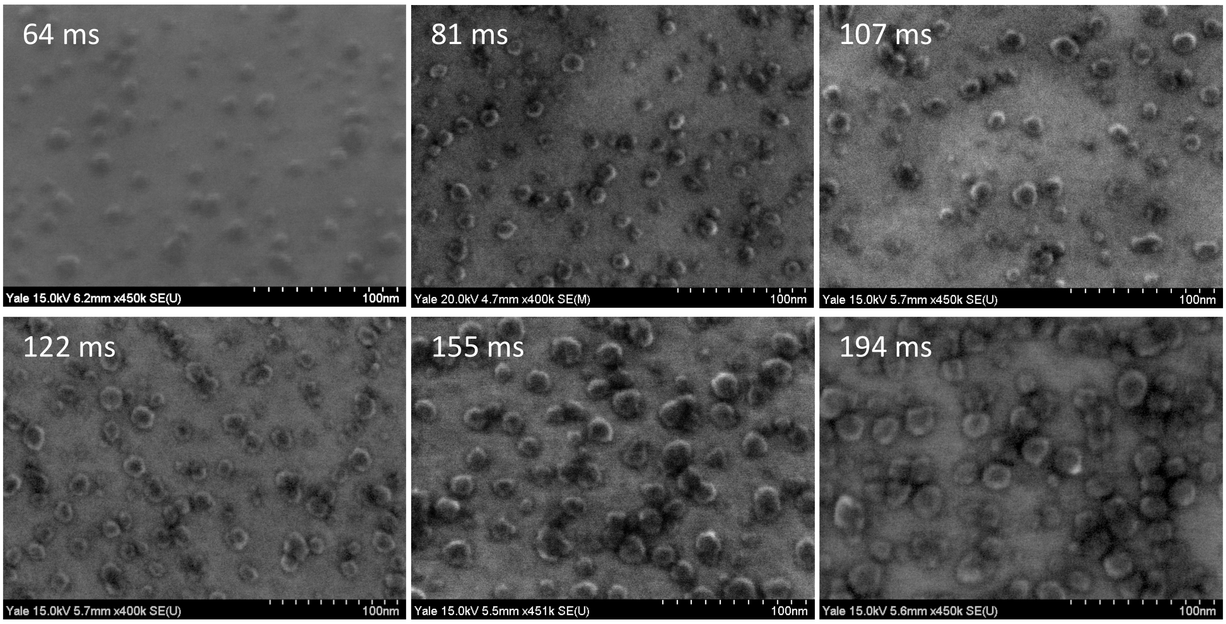

Figure 6.13: Some of the SEM images taken on the samples at different residence times. The growth can be noticed even at a first glance.

The two curves at 64 and 81 ms are very close and this could indicate that there is a lower limit to the particle size distribution, for example because of the temporal scales of the reactions on the wire surface, which are larger than a certain threshold residence time. If this were true the curves should all collapse in one below this time.

New samples were taken at 42, 24 and 11 ms residence time to verify this hypothesis.

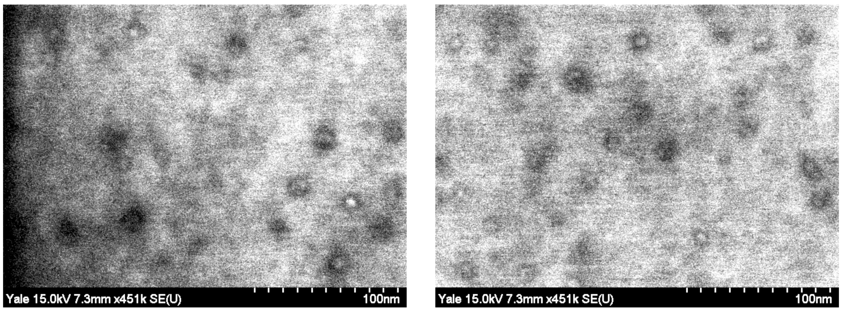

Figure 6.14: SEM image of particles on the sample at 42 ms residence time.

No particle size distribution could be precisely calculated, because the particles were too small, approaching the limits of the SEM.

In fact, as it can be seen from Figure 6.14, the maximum size is around 10 nm, whereas on the other samples particles up to 30 nm were found. Hence, it can be inferred that the PSD keeps shifting toward smaller diameters as the residence time is lowered.

No SEM analysis could be made on the samples at 24 and 11 ms residence time probably because the particles were too small and sparse to be observed.

Once ascertained that chemical growth was actually happening on the wire, a blue flame (Equivalence ratio 1.6, dilution 10.5) was stabilized to have a confirmation that the growth is only related to soot and not to the substrate reacting in the flame.

Sampling was made at 100 ms, 1 s and 3 s residence time and no particles were collected on any of the samples.

6.6.2 Height 2: sampling results at 11.3 mm above the burner

The results obtained in the first sampling are confirmed at lower height above the burner. The quantitative results are summarized in table 6.5. It is worth to notice that the standard deviation increases with the residence time, suggesting once again the broadening of the particles' size range and the mean diameter increases with the residence time beyond any experimental uncertainty (Figure 6.15).

Residence time [ms]	Mean diameter [nm]	Standard deviation
61	11.7	4.7
81	13.3	5.1
103	14.5	5.8
131	15.2	5.6
159	17.7	5.8
192	18.5	6.0

Table 6.5: Summary of the sampling results at 11.3 mm above the burner.

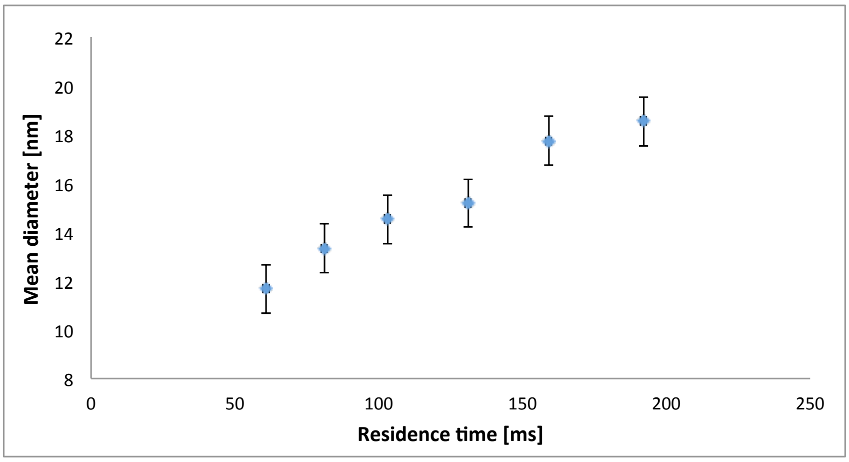

Figure 6.15: Change of the mean diameter with residence time at 11.3 mm above the burner.

Also the cumulative distribution and the PSD (Figure 6.16) present the same features as those inferred at 13.3 mm above the burner, like the increase in maximum size with increasing residence time and the shift of the mode toward higher diameters.

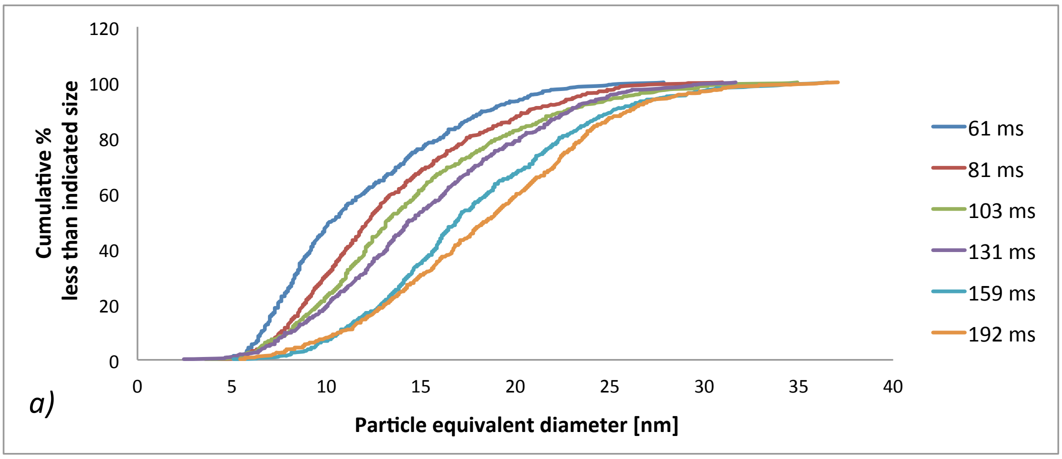

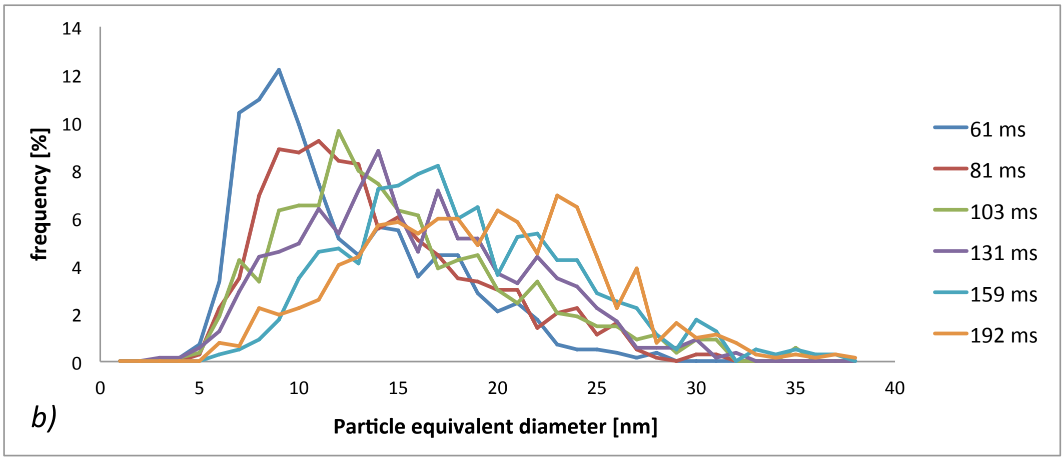

Figure 6.16: Cumulative particle size distribution (figure *a)* and PSDF (figure *b*) at 11.3 mm above the burner.

6.6.3 Height 3: sampling results at 9.5 mm above the burner

The results at 9.5 mm above the burner are totally consistent with the previous ones. All the characteristics discussed earlier are even more evident in this case. In fact, the standard deviation changes significantly from the sample at 60 ms and the one at 227 ms (Table 6.6) and the mean diameter increases in agreement with the samples at the other heights (Figure 6.17). The maximum size at the lowest residence time is far lower than that at the maximum residence time (around 18 nm against 34 nm, Figure 6.18) .

It would be rash to draw conclusions without additional measurements, but the simpler explanation could be that since particles are smaller, because we are in the flame region where the soot is forming, less mass has to be added to increase the diameter significantly.

Also, the flame composition changes with the distance from the burner, hence species with different reactivities might be present at the various heights; therefore the growth rate could change from one flame region to another.

Residence time [ms]	Mean diameter [nm]	Standard deviation
60	9.7	2.7
84	11.8	3.6
107	12.7	3.6
124	13.5	4.9
148	15.1	4.2
178	15.9	4.4
202	16.7	5.8
227	18.0	5.6

Table 6.6: Summary of the sampling results at 9.5 mm above the burner.

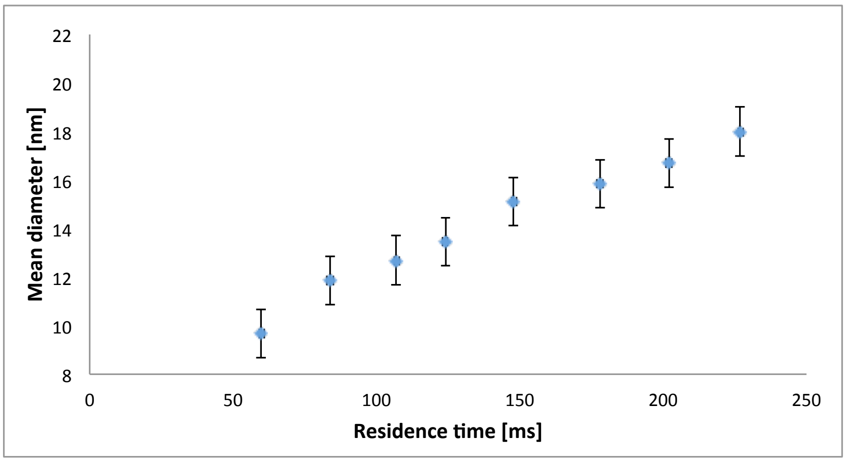

Figure 6.17: Change of the mean diameter with residence time at 9.5 mm above the burner.

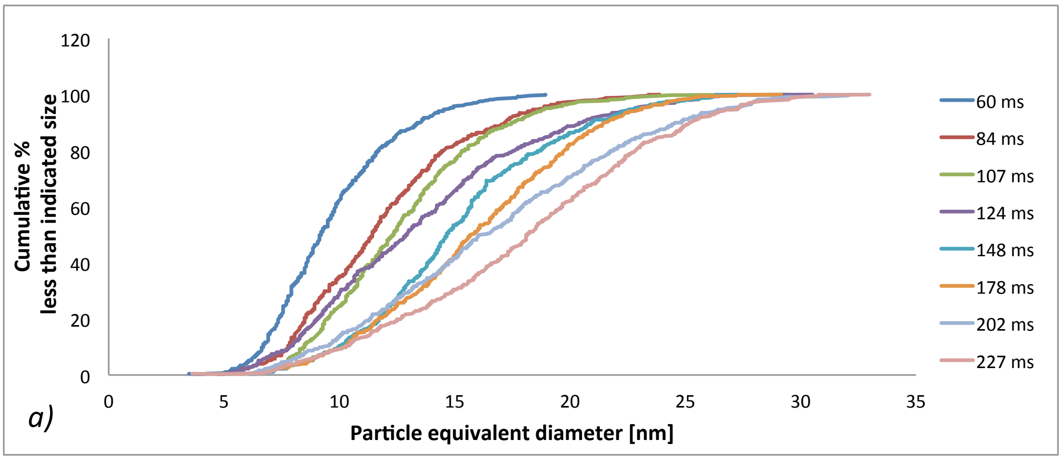

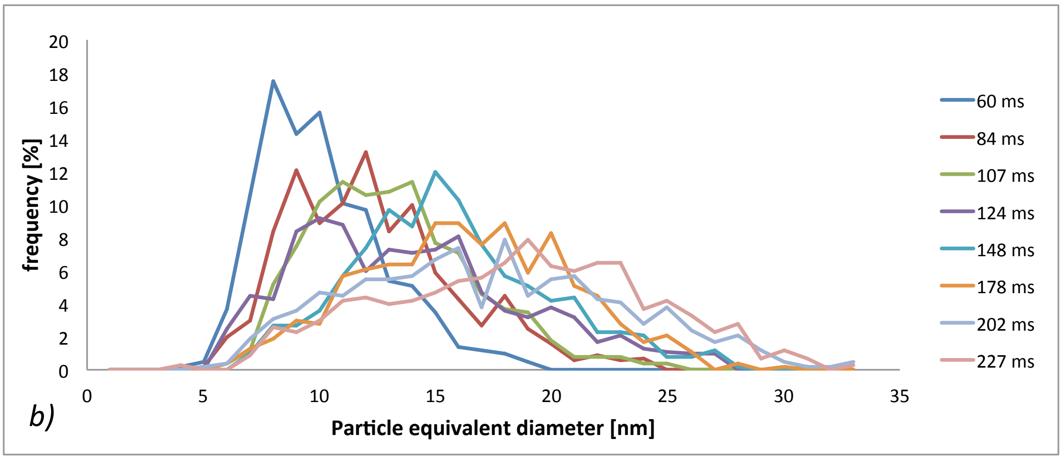

Figure 6.18: Cumulative particle size distribution (figure *a)* and PSDF (figure *b*) at 9.5 mm above the burner.

The shift is evident at all of the sampling positions, therefore it is not possible to sample thermophoretically on such a thin wire; a thicker one is needed instead to have a lower temperature and thus prevent the artifacts due to chemical growth.

6.7 DIFFERENT SUBSTRATES

Once determined that artifacts are present on a hot wire, the choice of thicker (and hence colder by higher radiative loss) substrates was made.

In this paragraph an overview of all the substrates considered for sampling is given, to explain the logic behind the search for a new material.

Even though information on the particle size distribution cannot be drawn, these substrates provide important information about the morphology of the particles, hence they can be used to check the consistency between particles collected on different substrates.

6.7.1 Silicon Carbide

Of course the natural choice was to move to a thicker SiC wire, to have a direct comparison between a hotter and a colder substrate, keeping constant all the other parameters and hence decoupling the effects of the temperature and the composition of the substrate used.

Unluckily, all of the commercial available wires have a carbon core with CVD deposited Silicon Carbide or a pyrolytic carbon coating that reacts in the flame and prevents any clear distinction between the particles collected from the flame and those coming from the coating (Figure 6.19). In fact, if the wire is thrust in a non-sooty blue flame, particles should not be present on its surface, but SEM images (Figure 6.19 *b*) show that they are. The only possible explanation is that they do not come from the flame, but from the surface itself that is reacting due to high temperature.

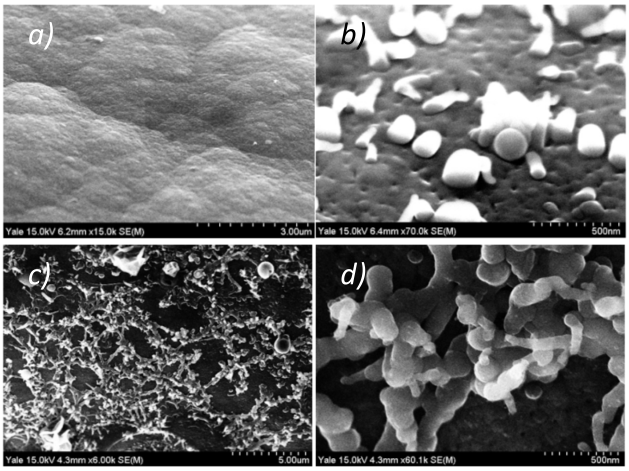

Figure 6.19: a) SiC surface before cleaning, b) particles on the surface after cleaning with a blue flame, c) and d) aggregates on the surface after sampling at 10 mm above the burner. Since with a blue flame no particles should be found, they could come from the surface.

The choice was then moved to wires not containing any carbon.

6.7.2 Sapphire wire and wafer

The wire has a 250 μm diameter. According to simulations the wire temperature, in the time lapse comparable to the residence time, is well below 600 K (Figure 5.20).

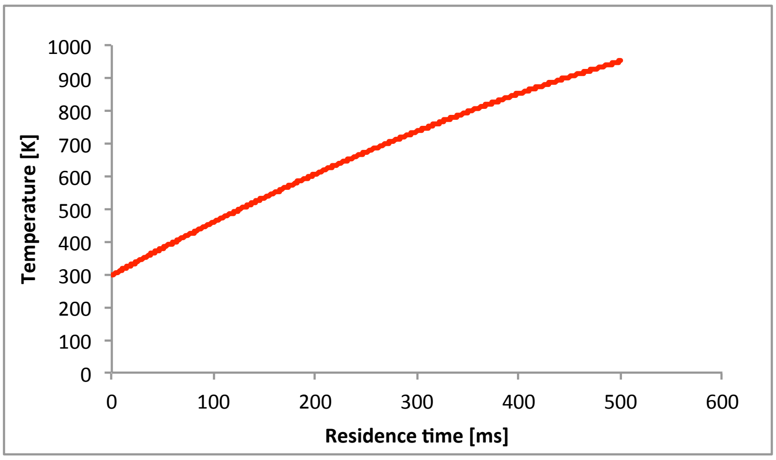

Figure 6.20: Temperature dynamics of the sapphire wire in the flame

This substrate is non conductive and thus no clear SEM pictures can be obtained to calculate a PSD distribution. Usually, when dealing with non-conductive substrates, a thin conductive coating is applied. In this case, coating the sample with chromium in order to make it conductive is not a viable solution, because the minimum coating thickness for the layer to be continuous is 5 nm, so it would hide most of the particles. With a carbon coating instead there is not enough contrast.

Despite these problems important information can be drawn about the morphology of the soot. In fact, from the pictures it appears clearly that the particles are liquid-like, they have a contact angle (Figure 6.21 *a* and *b*) and a graphitic core (from TEM images, Figure 6.21 *c*).

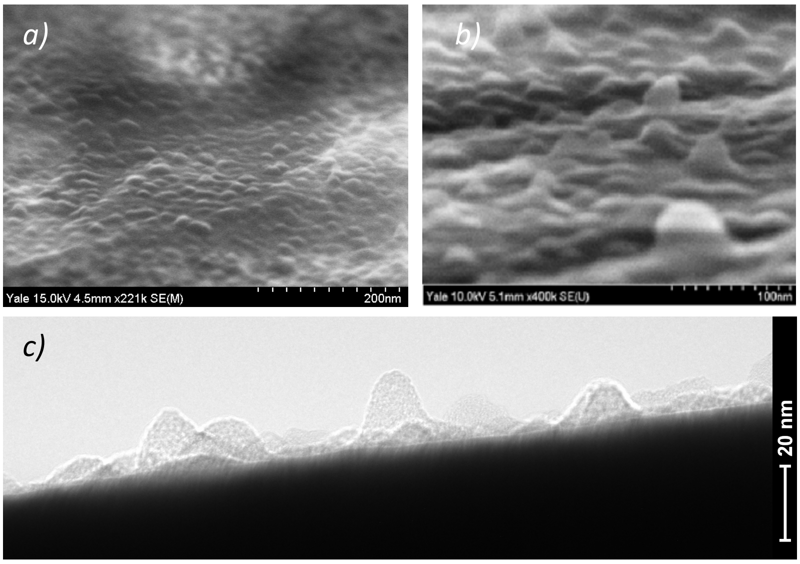

Figure 6.21: a), b): SEM images of liquid-like particles on sapphire at 13.3 mm above the burner, residence time 80 and 100 ms respectively; c) TEM image of particles on sapphire, 13.3 mm above the burner and 80 ms residence time.

The AFM is used to complete the information from SEM and TEM, but the requirements for the substrates are even stricter, because they need to be atomically flat, therefore a wire cannot be used and only few materials fulfill this requirement.

A sapphire wafer (200 µm thick) diced in small stripes (1.25 mm x 7 mm) with a dicing saw was cleaned following the instructions given in the paper by Dan Zhang et al.[125] (EtOH and Piranha solution) in the laboratory environment (no cleanroom) and then tested under AFM.

Even considering that sapphire wafers are not atomically flat, since they have a supplier's given roughness around 10Å, a lot of contamination from the environment could be seen on the sample, as shown in figure 6.22.

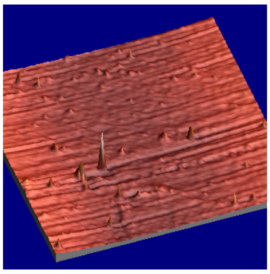

Figure 6.22: Sapphire surface before sampling, scanning area 5 µm x 5 µm. It can be seen that particles from the environment have relevant dimensions.

Anyway, an attempt is made on a sample with soot particles to see if a clear distinction can be made between soot and the particles of dirt.

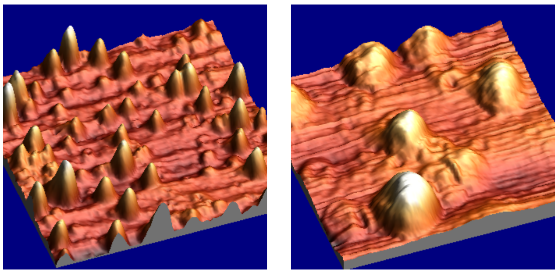

Figure 6.23: Soot particles on sapphire. Left image: scanning area 500 nm x 500 nm. Right image: scanning area 180 nm x 180 nm.

Apart from all the AFM issues, it is not possible to define a criterion to distinguish soot particles from dirt. Nevertheless, the morphology of the particles observed with this technique is consistent both with the results from TEM and SEM and with those published in other papers[66,67,111], showing that the particles seem to be liquid-like.

6.7.3 Silicon coated with SiO_2

Stripes around 4 x 7 mm are cut from a 200 µm thick silicon. According to the heat transfer calculation based on averaged formulas, the substrate temperature is below 500 K in the considered flame (1680 K) in the range of residence times we are interested in.

The SiO_2 coating lowers the conductivity too much, thus it is not possible to get images with good resolution under the SEM (Figure 6.24). However, qualitatively, the consistency of particles' morphology with that observed on the other substrates is confirmed.

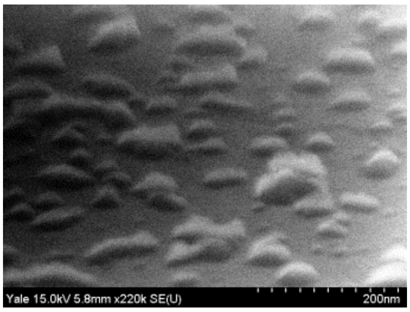

Figure 6.24: SEM image of soot particles on Silicon coated with SiO_2. Best resolution obtained under the SEM.

The surface roughness of the silicon wafer used is subnanometrical by supplier's standards, so it should not interfere with the analysis of soot particles.

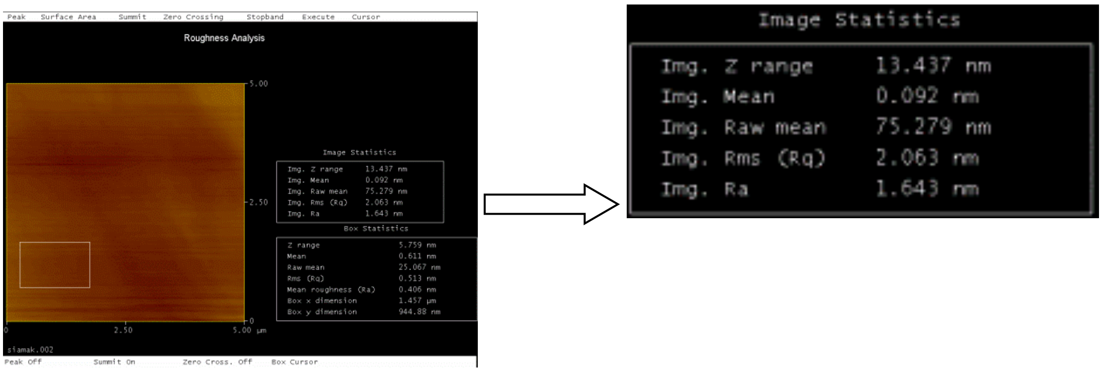

```
Image Statistics
Img. Z range      13.437 nm
Img. Mean          0.092 nm
Img. Raw mean     75.279 nm
Img. Rms (Rq)      2.063 nm
Img. Ra            1.643 nm
Box Statistics
Z range                  5.759 nm
Mean                     0.611 nm
Raw mean                25.067 nm
Rms (Rq)                 0.513 nm
Mean roughness (Ra)      0.406 nm
Box x dimension          1.457 µm
Box y dimension         944.88 nm
```

Image Statistics
Img. Z range 13.437 nm
Img. Mean 0.092 nm
Img. Raw mean 75.279 nm
Img. Rms (Rq) 2.063 nm
Img. Ra 1.643 nm

Figure 6.25: Characteristics of a "clean" Silicon substrate (before sampling).

It is possible to see from the image coming from the AFM analysis that the surface roughness is actually higher than 2nm. This means that the surface is full of particles that are several nanometers in height, because the sample is contaminated by particles present in the environment.

SEM images show that soot particles in the nucleation phase have diameters up to 20 nm, but they are usually “splashed” on the surface, hence they are only few nanometers tall.

This means that the background noise coming from the sample is of the same order of magnitude of the soot particles and hence it is not possible to distinguish the different kinds of particles present on the substrate.

6.8 PARTICLE SIZE DISTRIBUTION ON SILICON CARBIDE ON TOP OF SILICON

To overcome the conductivity problem, the Silicon carbide thin wire (13 µm) is glued with high temperature cement to the two edges on the long side of a silicon stripe (200 µm thick Silicon wafers coated with SiO2 were diced in stripes 200 µm wide and 2.54 cm long).

The cement does not affect the inertness of the substrate, since it is only put in drops at the far edges, and the wire is tense over the surface, even if not in intimate contact with it.

For consistency with the previous measurements, the flame chosen for sampling is the same used for the silicon carbide: **φ=2.1, dilution (N_2/C_2H_2) = 6.5, cold gas velocity = 6.5 m/s.**

According to the calculation, the temperature reached by the silicon stripe in these flame conditions and with residence times lower than 200 ms does not exceed 500 K (figure 6.26), therefore it is far lower than the temperature at which the kinetics of the surface chemical reactions becomes important.

With this arrangement also the silicon carbide is at a lower temperature because of the boundary layer generated by the presence of the silicon piece in the stream. Even though a precise calculation cannot be made, the proof that the silicon carbide is at low temperature is that it does not become incandescent in the flame.

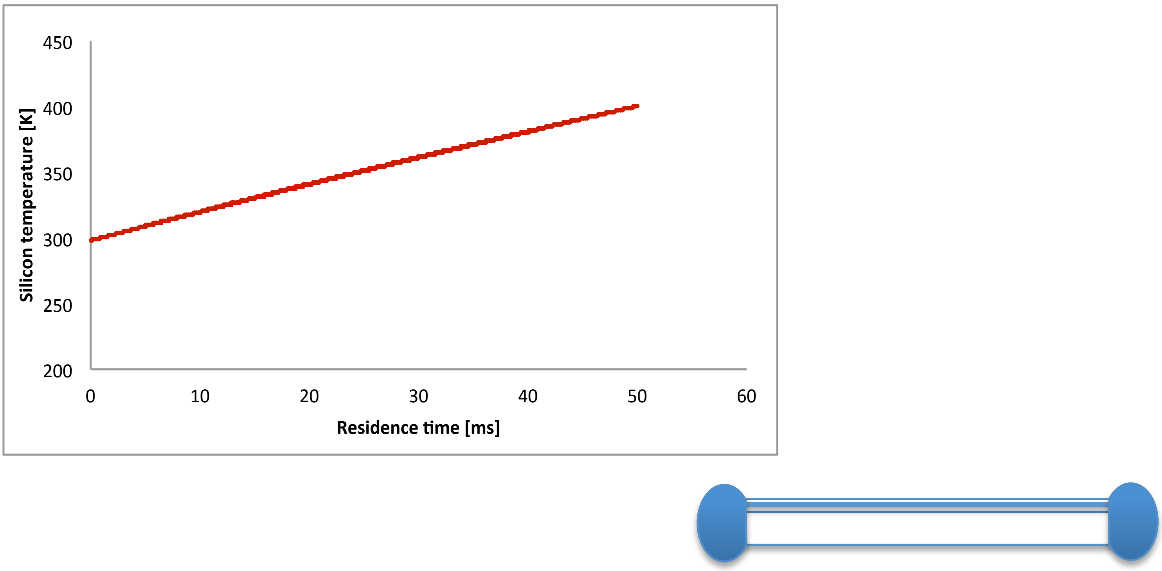

Figure 6.26: Temperature dynamics of the silicon substrate in the flame and schematization of the silicon carbide (blue wire) on silicon (white substrate). The blue semicircles at the edges represent the high-temperature cement.

The effect of the residence time on the particle size distribution was then studied on this substrate with SEM imaging, as previously done on the silicon carbide.

The sampling is carried out at two different heights above the burner to check the reproducibility of the results along the flame axis (Table 6.7).

	Distance from the burner [mm]
Height 1	13.3
Height 2	11.3

Table 6.7: Heights above the burner where the samples were taken.

The heights chosen are the same as those on the hotter substrate, in order to have the possibility of a direct comparison.

6.8.1 Height 1: sampling results at 13.3 mm above the burner

The results from two different sampling sessions at 13.3 mm above the burner are here presented (Table 6.8). The residence times are lower than those used for the thin Silicon carbide wire, because the thermophoretic force is stronger in this case and at higher residence times particles start to overlap. Thus it is not possible, under these flames conditions, to follow the evolution of the particle size distribution over a wide range of residence times.

	Residence time [ms]	Mean diameter [nm]	Standard deviation
First sampling	10	11.3	3.8
	14	12.7	4.1
	20	14	4.1
	32	14.7	4.5
Second sampling	9	11.3	3.8
	16	12.3	3.2
	21	12.9	3.8
	32	14.6	3.8

Table 6.8: Summary of the sampling results at 13.3 mm above the burner.

In both the sampling sessions the mean diameter increases with residence time (Figure 6.27). The hypothesis is that the growth is due to heavy species condensing on the substrate, since the kinetics of the reactions would be too slow at such temperature.

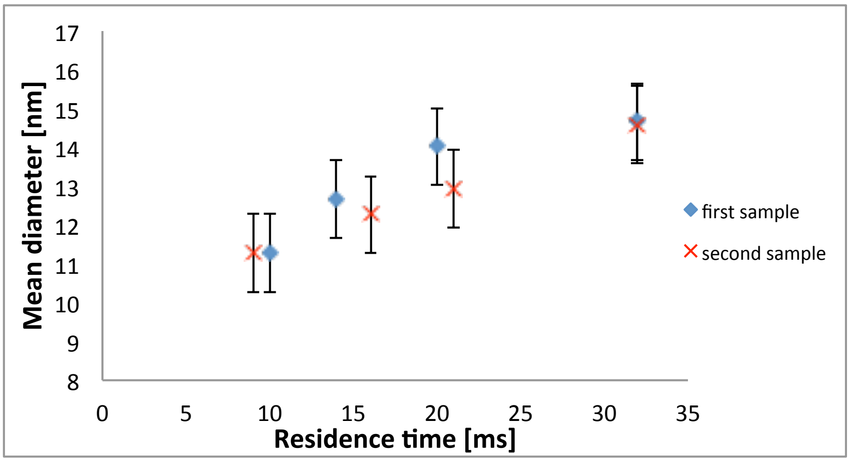

Figure 6.27: Change of the mean diameter with residence time at 13.3 mm above the burner.

The features of the particle size distribution are similar to those seen on the hot substrate (Figure 6.28). In fact, the mode shifts toward higher diameter with increasing residence time, the maximum size of the particles found increases too but smaller particles can still be seen. Even though the growth mechanism is completely different, it is still true that particles that deposit earlier are affected by interactions with the flame environment, whereas particles that deposit later have a lower growth. There is a good consistency between PSD drawn from sampling at similar residence times in the two sessions.

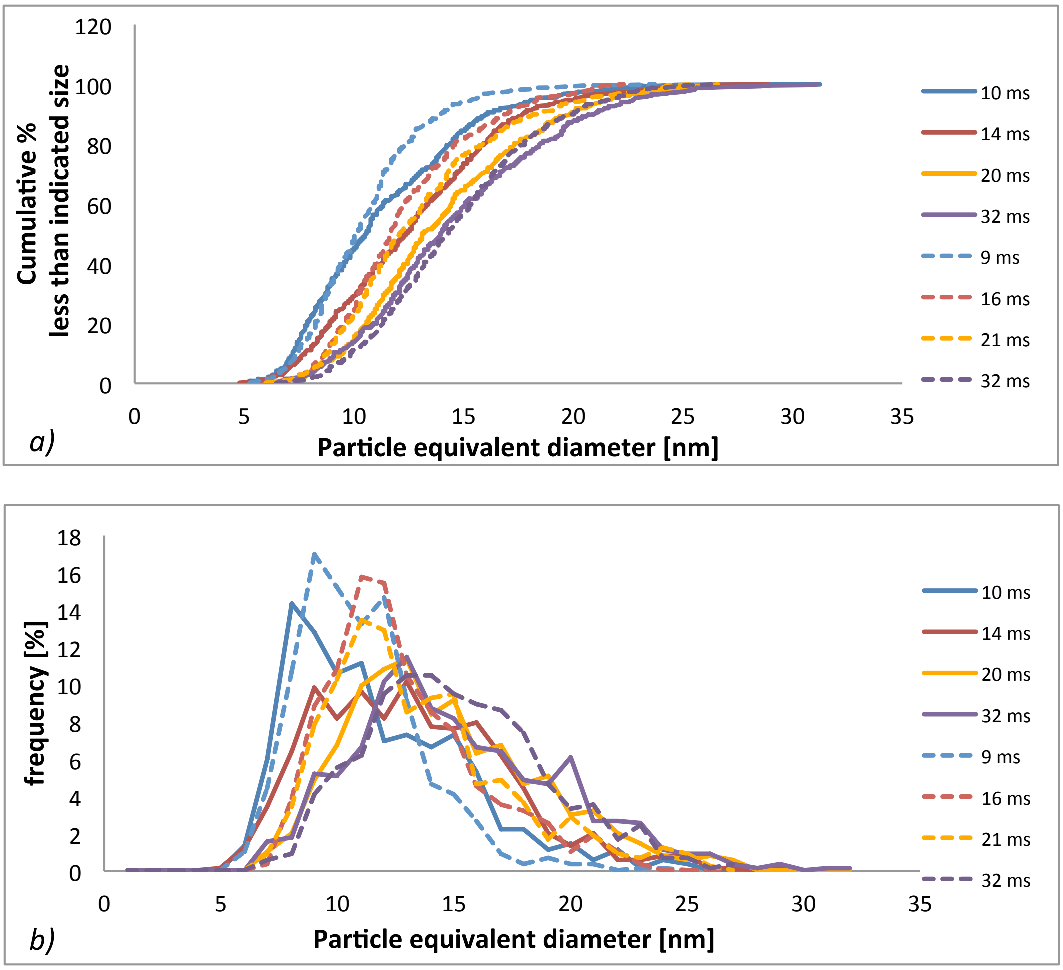

Figure 6.28: Cumulative particle size distribution (figure *a)* and PSDF (figure *b*) at 13.3 mm above the burner. Solid lines: first sample, dashed lines: second sample.

6.8.2 Height 2: sampling results at 11.3 mm above the burner

At lower height above the burner there is a total analogy with the results obtained at 13.3 mm from the burner surface. The diameter increases with increasing residence time (Figure 6.29) and the standard deviation increase too (Table 6.9). It is interesting to notice that at both distances the diameter increases more slowly at higher residence time. It would be premature to draw conclusions, because more data are needed and a less sooty flame should be set up to allow higher residence times without complete coverage of the substrate. Anyway, the most logical speculation to explain this fact is that, as seen before, more mass has to be added to bring the same change in the diameter if the particle is bigger and that the substrate gets hotter, therefore condensation is weaker.

Residence time [ms]	Mean diameter [nm]	Standard deviation
9	11.6	3.2
17	12.5	3.4
28	15.1	4.2
33	15.2	4.3

Table 6.9: Summary of the sampling results at 11.3 mm above the burner.

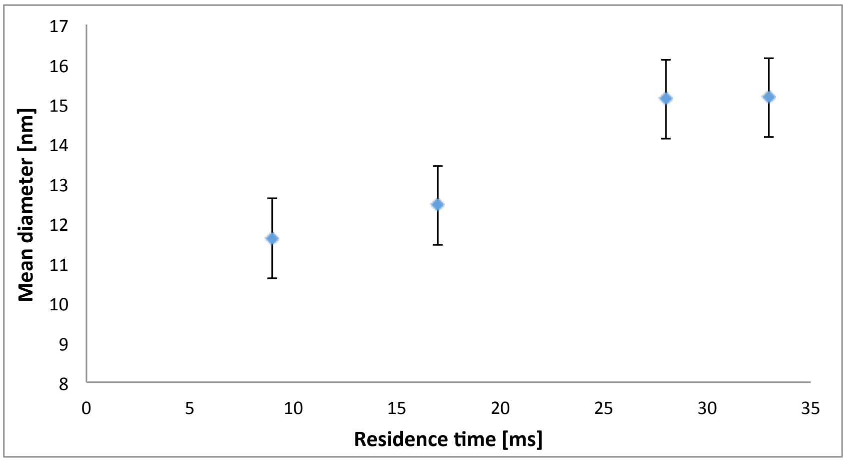

Figure 6.29: Change of the mean diameter with residence time at 11.3 mm above the burner.

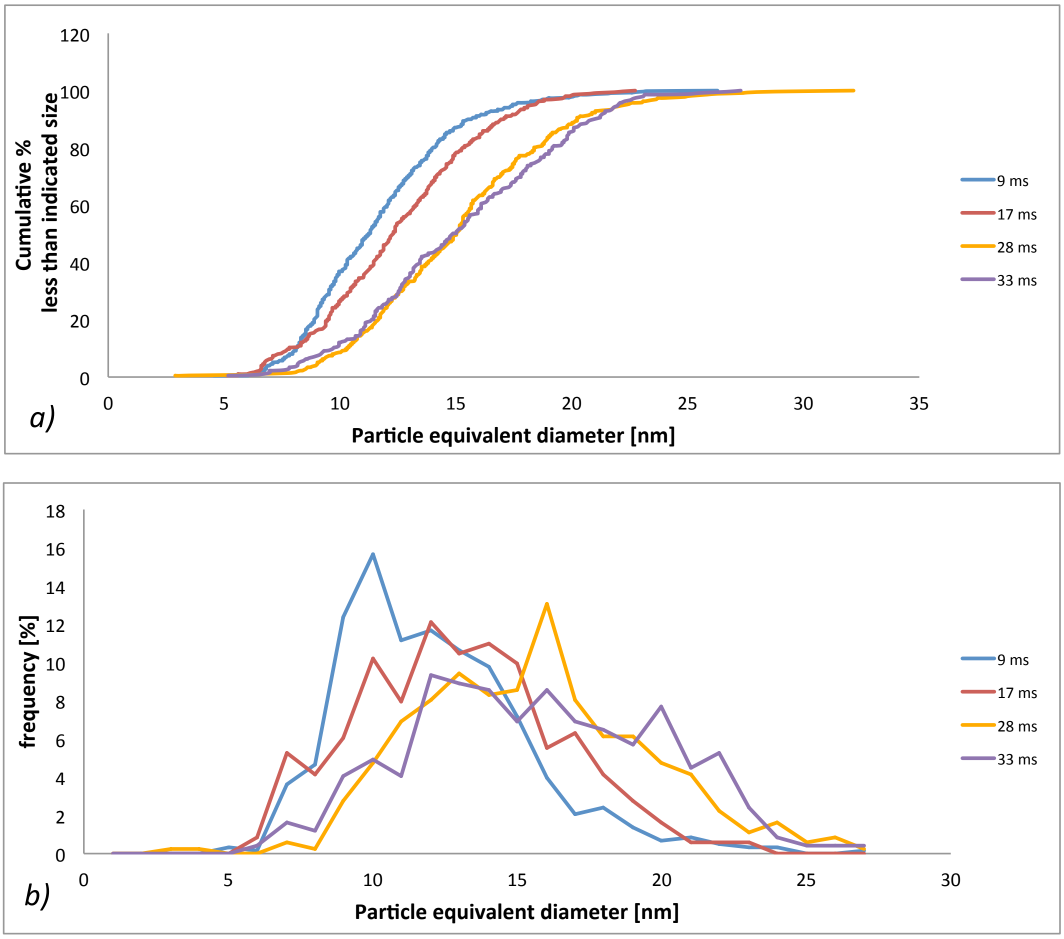

Figure 6.30: Cumulative particle size distribution (figure *a)* and PSDF (figure *b*) at 11.3 mm above the burner.

Even considering the experimental error, a shift in the particle size distribution toward bigger diameters at higher residence times is detected (figure 6.30).

Further investigation has to be done, to confirm with more data the growth by condensation and to study better the phenomenon.

If the shift were confirmed, one could try to sample on a substrate at an intermediate temperature: not high enough to have chemical growth, but enough to avoid condensation. This requires a very controlled situation, hard to reach in the experimental field and the drawback would be that in every different flame the temperature would change, hence this solution, even if it worked, could not be generalized.

6.9 MORPHOLOGY OF THE PARTICLES AND GROWTH

TEM and SEM images clearly show liquidity of the particles, on all the substrates.

The trend found by A.D. Abid et al.[66] and A.C. Barone et al.[111] is confirmed, the ratio height/base diameter increases with particle volume as shown in the pictures of figure 6.31 and 6.32.

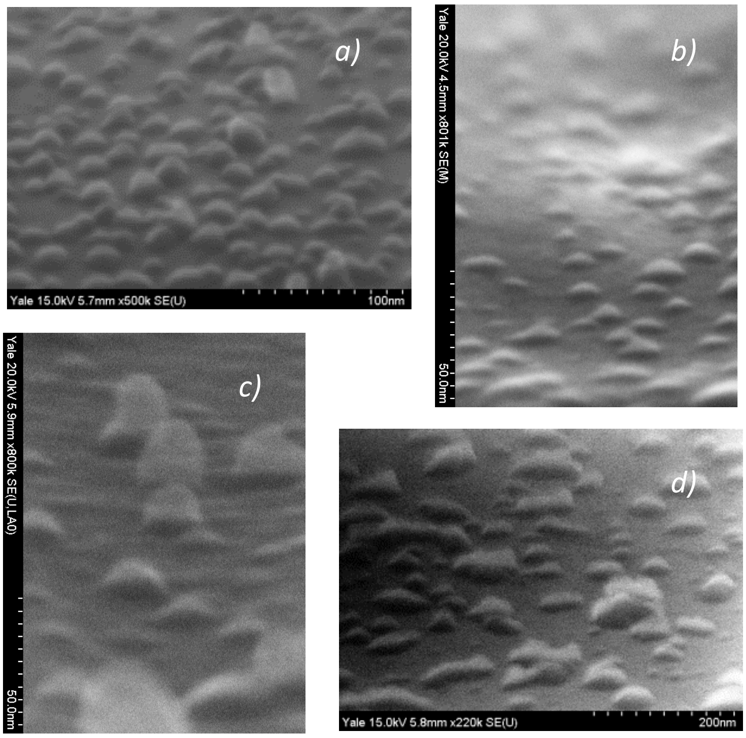

Figure 6.31: SEM image of particles seen from the side on silicon carbide (*a* and *b*), sapphire wire (*c*) and silicon coated with SiO_2 (*d*).

A quantification has to be done and since a systematic study has not been made, it is not possible to infer if the trend is the same at different residence times, also because the only information is on the 13 µm silicon carbide wire and the PSD shifts to higher particle volumes with increasing residence times.

Under the TEM on the sapphire wire it could clearly be seen that the onion-like structure described in several papers (see Chapter 1) in these flames conditions is already present in nascent soot.

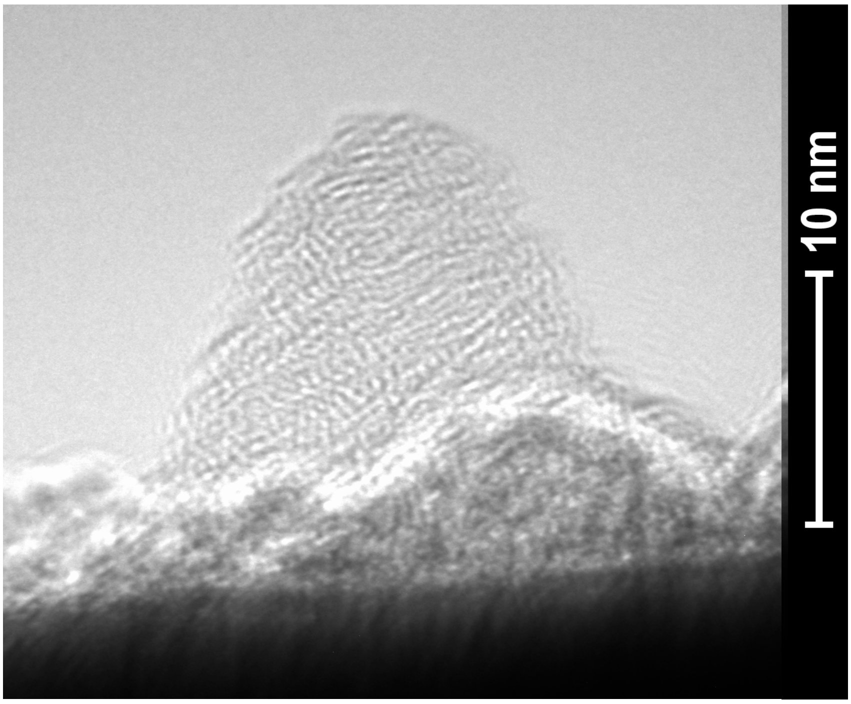

Figure 6.32: TEM image of a particle on sapphire wire, 108 ms residence time.

Since the liquidity is found on all the wires, it could be deduced that it is a real feature of the soot particles in the flame and it is not just due to growth on the wire.

Also, if the liquidity were only due to artifacts, the height over base diameter trend would probably not be respected, because the bigger particles, produced by chemical growth or condensation, would be the most liquid-like.

6.10 SIMULATION OF THE FLAME

The flame was simulated with the kinetic scheme HT1306s. Even though the experimental information cannot be compared directly with the simulation results, it is useful to give an overview of the expected structure of the system, since the work on this topic is going to be continued and more data will be available.

The model could also be an appropriate tool to study how the growth happens, which species are the "culprits" for chemical growth or which ones could condensate on the particles collected on the substrate based for example on their concentration and their vapor pressure.

Figure 6.33 shows the profiles of the major light gaseous species. The flame structure is the typical one for a rich environment, with the oxygen consumed at the beginning of the reaction zone, the carbon monoxide concentration decreasing slowly and the acetylene and the acetylene for the pyrolytic pathway.

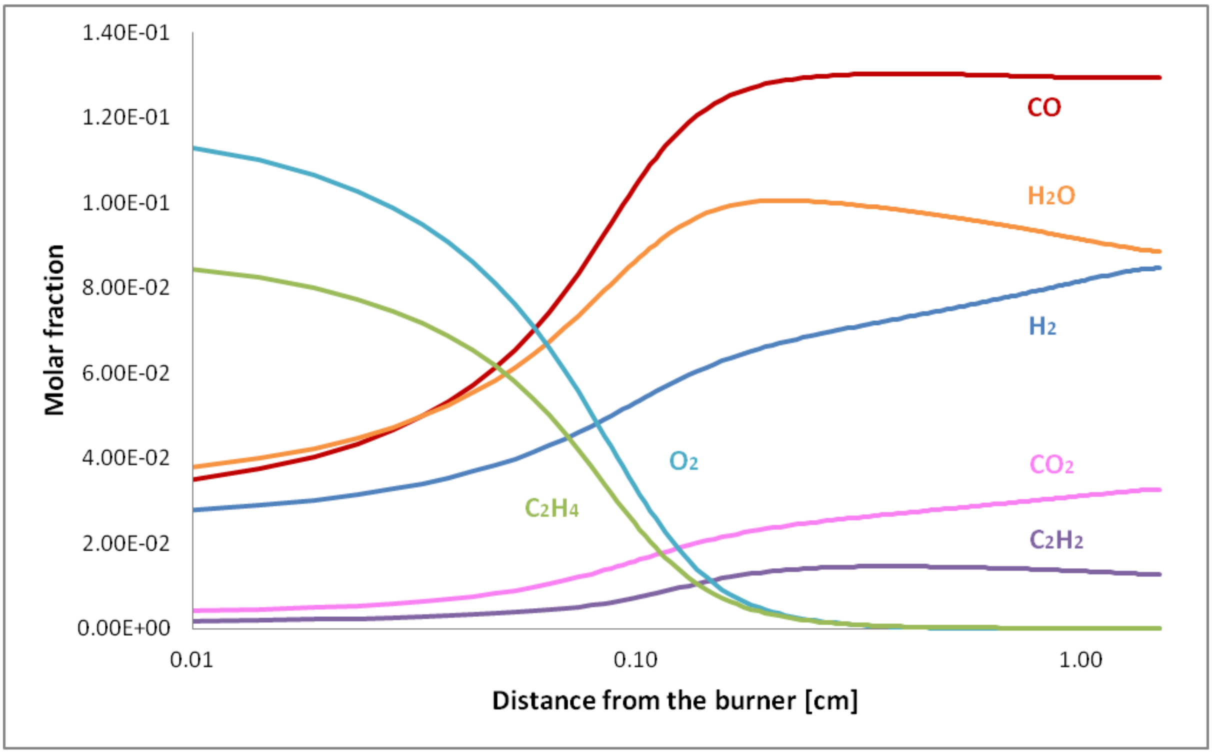

Figure 6.33: Computed profiles of the major light gaseous species

Profiles of benzene (C_6H_6), phenylacetylene (C_8H_6) and naphthalene ($C_{10}H_8$) are shown in figure 6.34. Their formation is sequential, because the three species are related through the HACA mechanism. In fact, acetylene addition can explain the passage from a 6 carbon atoms molecule to a 8 and then 10 carbon atoms molecule.

These hydrocarbons form in the region where the oxygen has already been consumed and the pyrolytic mechanism is active. In particular, phenylacetylene and naphthalene form in the region where acetylene concentration is maximal.

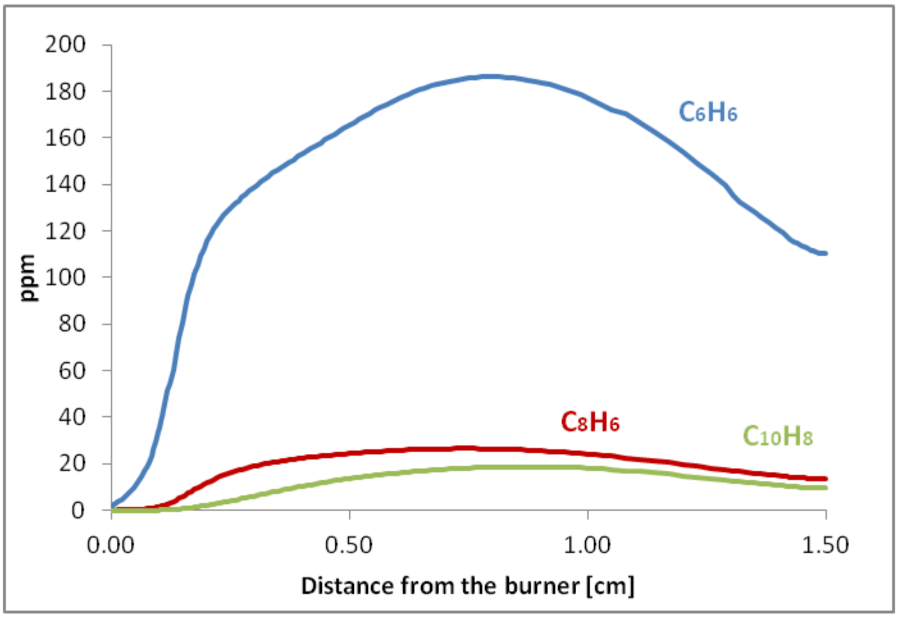

Figure 6.34: Computed profiles of benzene (C_6H_6), phenylacetylene (C_8H_6) and naphthalene ($C_{10}H_8$).

As for the soot, it is confirmed by the simulation that the flame is only lightly sooty and that, at the considered heights above the burner, the particle size distribution functions are dominated by small particles, while aggregates are not present or are in very low concentration (Figure 6.35). However, the shape of the PSDFs changes along the flame axis, showing a more pronounced bimodality as the distance from the burner surface increases, due to the persistence of nucleation phenomena simultaneously to particles growth and coagulation.

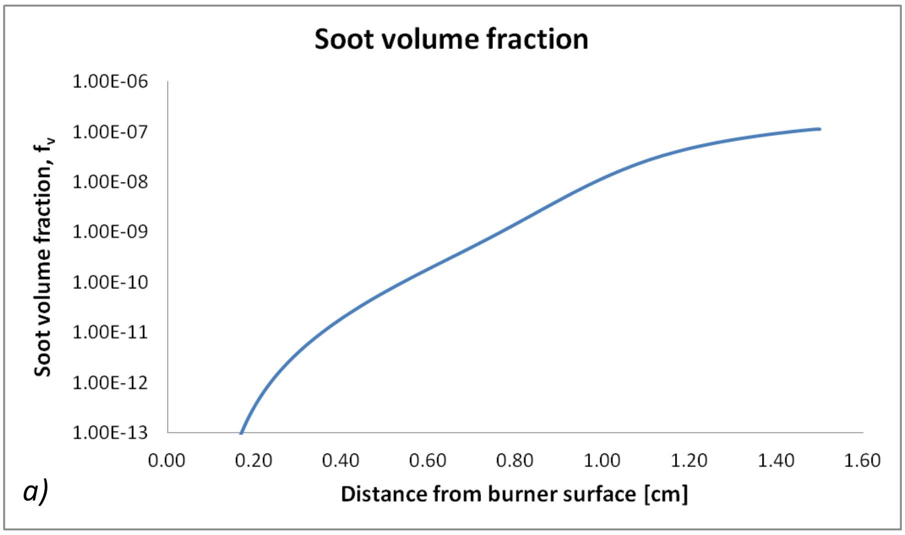

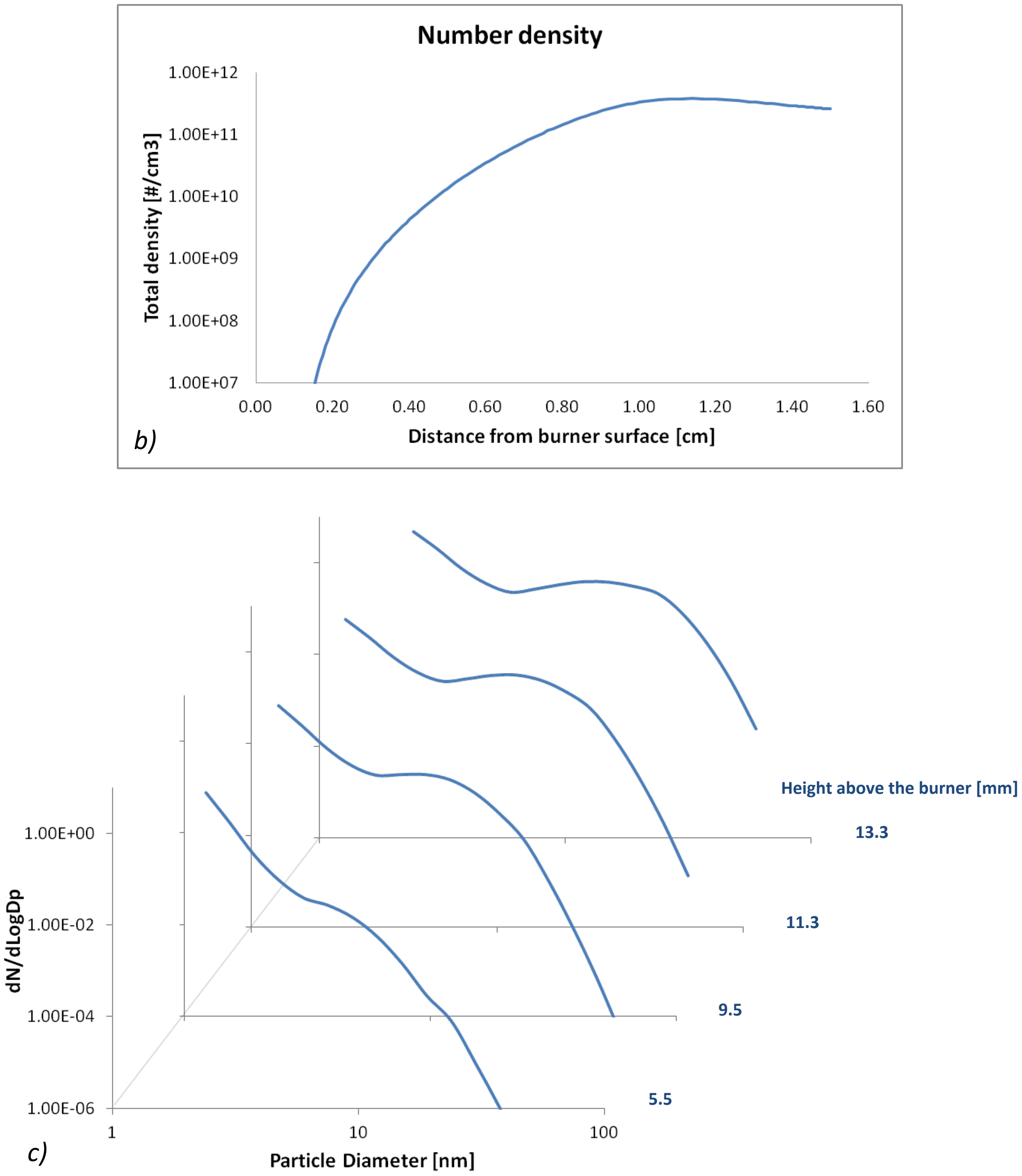

Figure 6.35: Soot volume fraction (figure *a*), number density (figure *b*) and particle size distribution functions (figure *c*) at different distances from the burner.

7 Conclusions and outlooks

Soot formation is a persistent problem in all of the processes involving combustion, from transportation to power generation and waste incineration. It has detrimental effects on environment, health and energy efficiency of the devices, therefore it is necessary to improve the understanding of the processes involved in its formation in order to correlate the operating conditions with emission characteristics. This thesis work originates from this need, and through modeling and experimental activity some steps forward in the comprehension of some phenomena have been moved, although further studies have to be done to improve the model and to describe quantitatively the findings on the thermophoretic sampling.

7.1 1D VS 2D APPROACH TO BSSF SIMULATION

The burner-stabilized stagnation flame from Wang and coworkers is simulated as a one-dimensional counterflow flame with zero velocity on the oxidizer side, thus the stagnation surface coincides with the physical surface of the oxidizer nozzle. Normally the nominal flux at the nozzles is equal to the sum of the convective and diffusive fluxes, while for particles the total flux at the oxidizer boundary is not zero, because soot, due to the thermophoretic force, deposits on the stagnation wall, creating a thermophoretic mass flux of particles if this aspect is not taken into account the model cannot describe properly soot distribution along the axis.

LaminarSMOKE is used for a two-dimensional simulation of a non-reactive flow in the stagnation-plane configuration. The comparison with the one-dimensional simulation shows that the results in the two cases are almost identical, apart from a small deviation of the soot mass fraction next to the stagnation plane. This means that the 1D model is fully capable of describing the BSSF configuration, without altering the flow field.

The next step will be to compare the one- and two-dimensional models on a reactive case, notably Wang's BSSF.

7.2 COMPUTATIONAL MODELING RESULTS

The scheme capability to reproduce the expected trends with respect to temperature, pressure and equivalence ratio is tested on an ethylene PFR, and the results are in good agreement with the theoretical knowledge, meaning that the soot produced increases with pressure and with the amount of fuel and aggregates appear earlier along the reactor axis.

The comparison with experimental data, very important for the tuning process, provides useful information for the model.

In fact, when the model is compared to laminar premixed ethylene flames at different composition and pressure it can be observed that the trends are well matched, even though the soot volume fraction is underpredicted at temperatures below 1700 K (Ciajolo et al.) and slightly overpredicted at higher equivalence ratios (Faeth and coworkers). At higher pressures (Tsurikov) the model manages to predict quite well the increase of soot concentration.

Depending on the fuel different kinetic pathways are involved in soot formation. The mechanisms considered in the model developed at Politecnico di Milano are shown in case of ethylene, propylene or toluene flames (Tsurikov).

In case of ethylene the model behaves quite well, whereas in propylene and toluene flames the underprediction is remarkable.

The comparison with the experimental data from the BSSF flame (Wang) show that the model is able to predict the temperature within the experimental error, and also the soot volume fraction is in agreement with the measured data. It can also reproduce the bimodal distribution found experimentally, which is important to characterize the formation of the smallest particles, particularly dangerous for human health. The number density is slightly overpredicted, due to an overestimation of the particles involved in the nucleation step.

Overall, the model has a good capability to predict results in agreement with experimental results, but further improvements might be done by means of a wider validation process that involves different fuels, configurations and operating conditions.

7.3 EXPERIMENTAL ACTIVITY

Thermophoretic sampling of soot particles in an ethylene premixed laminar flame at atmospheric pressure was carried out on different substrates to find a suitable technique for high-pressure sampling. The collected particles are analyzed under various microscopes and images from scanning electron microscopy are used to measure particles' size and study if, by changing the residence time of the wire in the flame, the observed PSDF changes too due to interactions of the deposited particles with the flame environment.

The silicon carbide wire with a 13 µm diameter has a maximum temperature in the flame of about 1570 K, therefore there might be chemical reactions with the species from the flame. The results obtained at 9.5, 11.3 and 13.3 mm above the burner show that the mode of the distribution shifts to higher diameters with increasing residence time and that the number of small particles decreases and the maximum particle's size found at longer residence times is larger than the one found at shorter residence times. This can be interpreted as a further confirmation of the growth, because it is consistent with a mechanism for which particles keep depositing on the wire during the whole sampling, but older particles continue to grow.

The same silicon carbide wire glued to a thicker piece of silicon has a maximum temperature in the flame well below 1400 K, hence kinetics would be too slow to sensibly affect the particle size distribution observed by chemical growth. Instead, it is possible that growth happens because of heavy condensable species condensing on the substrate.

The features of the observed particle size distributions at 13.3 and 11.3 mm above the burner are similar to those seen on the hot substrate. Even considering the experimental error, a shift in the particle size distribution toward bigger diameters at higher residence times is detected.

Further investigation has to be done, to confirm with more data the growth by condensation and to study better the phenomenon.

References

1 North Central Texas Council of Governments. Health Concerns Associated with Excessive Idling. http://www.nctcog.org/trans/air/vehicles/health.asp. March 2014.

2 Baumbach, G. *Air Quality Control*. (Springer, 1998).

3 Harvard-Smithsonian center for astrophysics. The Habitable Planet: online textbook. http://www.learner.org/courses/envsci/index.html. January 2014.

4 NASA. Atmospheric Aerosols: What Are They, and Why Are They So Important? http://www.nasa.gov/centers/langley/news/factsheets/Aerosols.html. January 2014.

5 Voiland, A. NASA Earth Observatory. http://earthobservatory.nasa.gov/Features/Aerosols/page2.php. January 2014.

6 Harrison, R. M. *et al.* SCOPE 50 - Radioecology after Chernobyl, Chapter3, Atmospheric Pathways. http://www.scopenvironment.org/downloadpubs/scope50/chapter03.html. January 2014.

7 World Health Organization. Hazard Prevention and Control in the Work Environment: Airborne Dust. http://www.who.int/occupational_health/publications/en/. January 2014.

8 HUSS Group. http://hussgroup.com/cdc/en/infocenter/PM.php. December 2013.

9 Alfè, M. *et al.* Structure–property relationship in nanostructures of young and mature soot in premixed flames. *Proceedings of the Combustion Institute* **32**, 697-704, (2009).

10 Vander Wal, R. L. & Tomasek, A. J. Soot nanostructure: dependence upon synthesis conditions. *Combustion and Flame* **136**, 129-140, (2004).

11 Spencer, W. G. Soot in cells of chimney-sweep's cancer. *Medico-Chirurgical Transactions* **xii**, 59-67, (1890).

12 Janssen, N. A. H. *et al.* Health effects of black carbon. (2012).

13 Bond, T. C. *et al.* Bounding the role of black carbon in the climate system: A scientific assessment. *Journal of Geophysical Research: Atmospheres* **118**, 5380-5552, (2013).

14 Ranzi, E., Dente, M., Faravelli, T. & Pennati, G. Prediction of Kinetic Parameters for Hydrogen Abstraction Reactions. *combustion science and technology* **95**, 1-50, (1994).

15 Tham, M. Overview of mechanistic modeling techniques - Department of Chemical and Process Engineering, University of Newcastle upon Tyne. http://lorien.ncl.ac.uk/ming/dynamics/modelling.pdf. January 2014.

16 Thakur, A. K. in *New Trends in Pharmacokinetics* (eds Aldo Rescigno & Ajit K. Thakur) 41-51 (Springer US, 1991).

17 Lindemann, F. A. Discussion on "the radiation theory of chemical action". *Transactions of the Faraday Society* **17**, 598-606, (1922).

18 Stewart, P. H., Larson, C. W. & Golden, D. M. Pressure and Temperature Dependence of Reactions Proceeding Via. *Combustion and Flame* **75**, 25-31, (1989).

19 Benson, S. W. *Thermochemical kinetics: methods for the estimation of thermochemical data and rate parameters*. 2 edn, (Wiley, 1976).

20 Ranzi, E., Faravelli, T., Gaffuri, P. & Sogaro, A. Low-temperature combustion: Automatic generation of primary oxidation reactions and lumping procedures. *Combustion and Flame* **102**, 179-192, (1995).

21 Ranzi, E. *et al.* A wide-range modeling study of iso-octane oxidation. *Combustion and Flame* **108**, 24-42, (1997).

22 Cuoci, A., Frassoldati, A., Faravelli, T. & Ranzi, E. OpenSMOKE : numerical modeling of reacting systems with detailed kinetic mechanisms. in *XXXIV Meeting of the Italian Section of the Combustion Institute.* 1-6.

23 Kee, R. J., Rupley, F. M. & Miller, J. A. *Chemkin-II: A Fortran chemical kinetics package for the analysis of gas-phase chemical kinetics*. (Sandia National Labs., 1989).

24 Stull, D. R. & Prophet, H. JANAF thermochemical tables. (National Standard Reference Data System, 1971).

25 Burcat, A. in *Thermochemical data for combustion calculations* (ed William C. Gardiner, Jr.) 455-473 (Springer US, 1984).

26 Abid, A. D., Camacho, J., Sheen, D. a. & Wang, H. Quantitative measurement of soot particle size distribution in premixed flames – The burner-stabilized stagnation flame approach. *Combustion and Flame* **156**, 1862-1870, (2009).

27 Lamont-Doherty Earth Observatory/Columbia University. Conservation Equations. http://www.ldeo.columbia.edu/~mspieg/mmm/Conserveq.pdf. February 2014.

28 Bird, R. B., Stewart, W. E. & Lightfoot, E. N. *Transport Phenomena*. 2nd edn, (2002).

29 Poinsot, T. & Veynante, D. *Theoretical and Numerical Combustion*. 3rd edn, (2001).

30 Waldmann, L. & Schmitt, K. H. *Aerosol Science*. (1966).

31 Talbot, L., Cheng, R. K., Schefer, R. W. & Willis, D. R. Thermophoresis of particles in a heated boundary layer. *Journal of Fluid Mechanics* **101**, 737-758, (1980).

32 Hall, R. J. The radiative source term for plane-parallel layers of reacting combustion gases. *Journal of Quantitative Spectroscopy & Radiative Transfer* **49**, 517-523, (1993).

33 Cuoci, A., Frassoldati, A., Faravelli, T. & Ranzi, E. A computational tool for the detailed kinetic modeling of laminar flames: Application to C2H4/CH4 coflow flames. *Combustion and Flame* **160**, 870-886, (2013).

34 Sazhin, S. S. An Approximation for the Absorption Coefficient of Soot in a Radiating Gas. (Fluent Europe, Ltd., 1994).

35 Taylor, P. B. & Foster, P. J. Some Gray Weighting Coefficients for CO2 –H2O-Soot Mixtures. *International Journal of Heat and Mass Transfer* **18**, 1331-1332, (1974).

36 Smith, T. F., Shen, Z. F. & Friedman, J. N. Evaluation of Coefficients for the Weighted Sum of Gray Gases Model. *Journal of Heat Transfer* **104**, 602-608, (1982).

37 Wang, H. & Frenklach, M. A detailed kinetic modeling study of aromatics formation in laminar premixed acetylene and ethylene flames. *Combustion and Flame* **110**, 173-221, (1997).

38 Wang, H. Formation of nascent soot and other condensed-phase materials in flames. *Proceedings of the Combustion Institute* **33**, 41-67, (2011).

39 Frenklach, M. Reaction mechanism of soot formation in flames. *Physical Chemistry Chemical Physics* **4**, 2028-2037, (2002).

40 Frenklach, M., Clary, D. W., Yuan, T., Gardiner Jr, W. C. & Stein, S. E. Mechanism of Soot Formation in Acetylene-Oxygen Mixtures. *combustion science and technology* **50**, 79-115, (1986).

41 Frenklach, M., Clary, D. W., Gardiner Jr, W. C. & Stein, S. E. Detailed kinetic modeling of soot formation in shock-tube pyrolysis of acetylene. *Symposium (International) on Combustion* **20**, 887-901, (1985).

42 Frenklach, M. & Warnatz, J. W. Detailed Modeling of PAH Profiles in a Sooting Low-Pressure Acetylene Flame. *combustion science and technology* **51**, 265-283, (1987).

43 Frenklach, M. & Wang, H. Detailed modeling of soot particle nucleation and growth. *Symposium (International) on Combustion* **23**, 1559-1566, (1990).

44 Cole, J. A., Bittner, J. D., Longwell, J. P. & Howard, J. B. Formation mechanisms of aromatic compounds in aliphatic flames. *Combustion and Flame* **56**, 51-70, (1984).

45 Colket, M. B. The pyrolysis of acetylene and vinylacetylene in a single-pulse shock tube. *Symposium (International) on Combustion* **21**, 851-864, (1986).

46 Richter, H. & Howard, J. B. Formation of polycyclic aromatic hydrocarbons and their growth to soot-a review of chemical reaction pathways. *Progress in Energy and Combustion Science* **26**, 565-608, (2000).

47 Miller, J. A. & Melius, C. F. Kinetic and thermodynamic issues in the formation of aromatic compounds in flames of aliphatic fuels. *Combustion and Flame* **91**, 21-39, (1992).

48 Fahr, A. & Stein, S. E. Reactions of vinyl and phenyl radicals with ethyne, ethene and benzene. *Symposium (International) on Combustion* **22**, 1023-1029, (1988).

49 Marinov, N. M., Pitz, W. J., Westbrook, C. K., Castaldi, M. J. & Senkan, S. M. Modeling of aromatic and polycyclic aromatic hydrocarbon formation in premixed methane and ethane flames. *combustion science and technology* **116**, 117-211, (1996).

50 D'Anna, A. & Violi, A. A kinetic model for the formation of aromatic hydrocarbons in premixed laminar flames. *Symposium (International) on Combustion* **27**, 425-433, (1998).

51 D’Anna, A., Sirignano, M. & Kent, J. A model of particle nucleation in premixed ethylene flames. *Combustion and Flame* **157**, 2106-2115, (2010).

52 Bockhorn, H. *Soot Formation in Combustion (Mechanisms and Models)*. (Springer Series in Chemical Physics, 1994).

53 Zhang, Q. L. *et al.* Reactivity of Large Carbon Clusters: Spheroidal Carbon Shells and Their Possible Relevance to the Formation and Morphology of Soot. *The Journal of Physical Chemistry* **90**, 525-528, (1986).

54 Miller, J. H. The kinetics of polynuclear aromatic hydrocarbon agglomeration in flames. *Symposium (International) on Combustion* **23**, 91-98, (1990).

55 Herdman, J. D. & Miller, J. H. Intermolecular potential calculations for polynuclear aromatic hydrocarbon clusters. *The journal of physical chemistry A* **112**, 6249-6256, (2008).

56 Richter, H., Benish, T. G., Mazyar, O. a., Green, W. H. & Howard, J. B. Formation of polycyclic aromatic hydrocarbons and their radicals in a nearly sooting premixed benzene flame. *Proceedings of the Combustion Institute* **28**, 2609-2618, (2000).

57 Ciajolo, A. *et al.* The Relation Between Ultraviolet-Excited Fluorescence Spectroscopy and Aromatic Species Formed in Rich Laminar Ethylene Flames. *Combustion and Flame* **125**, 1225-1229, (2001).

58 Allouis, C. *et al.* Monitoring of fuel consumption and aromatics formation in a kerosene spray flame as characterized by fluorescence spectroscopy. *Chemosphere* **51**, 1097-1102, (2003).

59 Violi, A. *et al.* A fully integrated kinetic monte carlo/molecular dynamics approach for the simulation of soot precursor growth. *Proceedings of the Combustion Institute* **29**, 2343-2349, (2002).

60 De Filippo, a., Sgro, L. a., Lanzuolo, G. & D’Alessio, a. Probe measurements and numerical model predictions of evolving size distributions in premixed flames. *Combustion and Flame* **156**, 1744-1754, (2009).

61 Echavarria, C. a., Sarofim, A. F., Lighty, J. S. & D'Anna, A. Modeling and measurements of size distributions in premixed ethylene and benzene flames. *Proceedings of the Combustion Institute* **32**, 705-711, (2009).

62 Manzello, S. L. *et al.* Soot particle size distributions in a well-stirred reactor/plug flow reactor. *Proceedings of the Combustion Institute* **31**, 675-683, (2007).

63 Maricq, M. M., Harris, S. J. & Szente, J. J. Soot size distributions in rich premixed ethylene flames. *Combustion and Flame* **132**, 328-342, (2003).

64 Maricq, M. M. Size and charge of soot particles in rich premixed ethylene flames. *Combustion and Flame* **137**, 340-350, (2004).

65 Öktem, B., Tolocka, M. P., Zhao, B., Wang, H. & Johnston, M. V. Chemical species associated with the early stage of soot growth in a laminar premixed ethylene–oxygen–argon flame. *Combustion and Flame* **142**, 364-373, (2005).

66 Abid, A. D. *et al.* Size distribution and morphology of nascent soot in premixed ethylene flames with and without benzene doping. *Proceedings of the Combustion Institute* **32**, 681-688, (2009).

67 Abid, A. D. *et al.* On evolution of particle size distribution functions of incipient soot in premixed ethylene–oxygen–argon flames. *Combustion and Flame* **154**, 775-788, (2008).

68 Zhao, B. *et al.* Measurement and numerical simulation of soot particle size distribution functions in a laminar premixed ethylene-oxygen-argon flame. *Combustion and Flame* **133**, 173-188, (2003).

69 Schuetz, C. a. & Frenklach, M. Nucleation of soot: Molecular dynamics simulations of pyrene dimerization. *Proceedings of the Combustion Institute* **29**, 2307-2314, (2002).

70 Richter, H., Granata, S., Green, W. H. & Howard, J. B. Detailed modeling of PAH and soot formation in a laminar premixed benzene/oxygen/argon low-pressure flame. *Proceedings of the Combustion Institute* **30**, 1397-1405, (2005).

71 Kazakov, A. & Frenklach, M. Dynamic Modeling of Soot Particle Coagulation and Aggregation: Implementation With the Method of Moments and Application to High-Pressure Laminar Premixed Flames. *Combustion and Flame* **114**, 484-501, (1998).

72 Retcofsky, H. L., Stark, J. M. & Friedel, R. a. Electron spin resonance in American coals. *Analytical Chemistry* **40**, 1699-1704, (1968).

73 Yan, S., Eddings, E. G., Palotas, A. B., Pugmire, R. J. & Sarofim, A. F. Prediction of Sooting Tendency for Hydrocarbon Liquids in Diffusion Flames. *Energy & Fuels* **19**, 2408-2415, (2005).

74 Ishiguro, T., Takatori, Y. & Akihama, K. Microstructure of diesel soot particles probed by electron microscopy: first observation of inner core and outer shell. *Combustion and Flame* **108**, 231-234, (1997).

75 Smoluchowski, M. V. Versuch einer mathematischen Theorie der Koagulationskinetik kolloider Losungen. *Zeitschrift fuer physikalische Chemie* **1210**, 129-168, (1914).

76 Homann, K. H. Carbon formation in premixed flames. *Combustion and Flame* **11**, 265-287, (1967).

77 Howard, J. B., Wersborg, B. L. & Williams, G. C. Coagulation of Carbon Particles in Premixed Flames. *Faraday Symposia of the Chemical Society* **7**, 109-119, (1973).

78 Balthasar, M. & Frenklach, M. Monte-Carlo simulation of soot particle coagulation and aggregation: the effect of a realistic size distribution. *Proceedings of the Combustion Institute* **30**, 1467-1475, (2005).

79 Mueller, M. E., Blanquart, G. & Pitsch, H. Modeling the oxidation-induced fragmentation of soot aggregates in laminar flames. *Proceedings of the Combustion Institute* **33**, 667-674, (2011).

80 Echavarria, C. a., Jaramillo, I. C., Sarofim, A. F. & Lighty, J. S. Studies of soot oxidation and fragmentation in a two-stage burner under fuel-lean and fuel-rich conditions. *Proceedings of the Combustion Institute* **33**, 659-666, (2011).

81 Sirignano, M., Kent, J. & D'Anna, A. Modeling Formation and Oxidation of Soot in Nonpremixed Flames. *Energy & Fuels* **27**, 2303-2315, (2013).

82 Vierbaum, R. & Roth, P. High-temperature oxidation of dispersed soot particles by O atoms. *Proceedings of the Combustion Institute* **29**, 2423-2429, (2002).

83 Frenklach, M. Method of moments with interpolative closure. *Chemical Engineering Science* **57**, 2229-2239, (2002).

84 Wen, J. Z., Thomson, M. J., Park, S. H., Rogak, S. N. & Lightstone, M. F. Study of soot growth in a plug flow reactor using a moving sectional model. *Proceedings of the Combustion Institute* **30**, 1477-1484, (2005).

85 Appel, J., Bockhorn, H. & Wulkow, M. A detailed numerical study of the evolution of soot particle size distributions in laminar premixed flames. *Chemosphere* **42**, 635-645, (2001).

86 Balthasar, M. & Kraft, M. A stochastic approach to calculate the particle size distribution function of soot particles in laminar premixed flames. *Combustion and Flame* **133**, 289-298, (2003).

87 McGraw, R. Description of Aerosol Dynamics by the Quadrature Method of Moments. *Aerosol Science and Technology* **27**, 255-265, (1997).

88 Wulkow, M. The simulation of molecular weight distributions in polyreaction kinetics by discrete Galerkin methods. *Macromolecular Theory and Simulations* **5**, 393-416, (1996).

89 Warnatz, J., Maas, U. & Dibble, R. W. *Combustion: physical and chemical fundamentals, modeling and simulation, experiments, pollutant formation*. (Springer, 2006).

90 Maricq, M. M. & Xu, N. The effective density and fractal dimension of soot particles from premixed flames and motor vehicle exhaust. *Journal of Aerosol Science* **35**, 1251-1274, (2004).

91 Lafleur, A. L., Taghizadeh, K., Howard, J. B., Anacleto, J. F. & Quilliam, M. A. Characterization of Flame-Generated C10 to C160 polycyclic aromatic hydrocarbons by atmospheric-pressure chemical ionization mass spectrometry with liquid introduction via heated nebulizer interface. *Journal of the American Society for Mass Spectrometry* **7**, 276-286, (1996).

92 Sgro, L. a. *et al.* Measurement of nanoparticles of organic carbon in non-sooting flame conditions. *Proceedings of the Combustion Institute* **32**, 689-696, (2009).

93 Sgro, L. a., De Filippo, a., Lanzuolo, G. & D'Alessio, a. Characterization of nanoparticles of organic carbon (NOC) produced in rich premixed flames by differential mobility analysis. *Proceedings of the Combustion Institute* **31**, 631-638, (2007).

94 Wagner, H. G. G. Soot formation in combustion. *Symposium (International) on Combustion* **17**, 3-19, (1979).

95 D'Anna, A. in *Combustion Generated Fine Carbonaceous Particles* (eds Henning Bockhorn, Andrea D'Anna, Adel F. Sarofim, & Ha Wang) Ch. 19, 289- (KIT scientific publishing, 2009).

96 Granata, S., Cambianica, F., Zinesi, S., Faravelli, T. & Ranzi, E. Detailed Kinetics of PAH and Soot Formation in Combustion Processes: Analogies and Similarities in reaction Classes. in *Proceedings of the European Combustion Meeting.*

97 Violi, A., Truong, T. N. & Sarofim, A. F. Kinetics of hydrogen abstraction reactions from polycyclic aromatic hydrocarbons by H atoms. *Journal of Physical Chemistry A* **108**, 4846-4852, (2004).

98 Colket, M. B. & Seery, D. J. Reaction mechanisms for toluene pyrolysis. *Symposium (International) on Combustion* **25**, 883-891, (1994).

99 Goel, A. & Howard, J. B. Reaction rate coefficient of fullerene (C60) consumption by soot. *Carbon* **41**, 1949-1954, (2003).

100 D'Alessio, a., Barone, a. C., Cau, R., D'Anna, a. & Minutolo, P. Surface deposition and coagulation efficiency of combustion generated nanoparticles in the size range from 1 to 10nm. *Proceedings of the Combustion Institute* **30**, 2595-2603, (2005).

101 D'Anna, A. & Kent, J. H. Modeling of particulate carbon and species formation in coflowing diffusion flames of ethylene. *Combustion and Flame* **144**, 249-260, (2006).

102 Marinov, N. M. *et al.* Aromatic and Polycyclic Aromatic Hydrocarbon Formation in a Laminar Premixed n-Butane Flame. *Combustion and Flame* **114**, 192-213, (1998).

103 Smith, G. P. *et al.* <http://www.me.berkeley.edu/gri_mech/> (

104 Ciajolo, A. *et al.* The effect of temperature on soot inception in premixed ethylene flames. *Twenty-Sixth Symposium (international) on Combustion/The Combustion Institute*, 2327-2333, (1996).

105 Xu, F., Sunderland, P. B. & Faeth, G. M. Soot formation in laminar premixed ethylene/air flames at atmospheric pressure. *Combustion and Flame* **108**, 471-493, (1997).

106 Tsurikov, M. S. *et al.* Laser-based investigation of soot formation in laminar premixed flames at atmospheric and elevated pressures. *Combustion Science and Technology* **177**, 1835-1862, (2005).

107 Böhm, H. *et al.* The influence of pressure and temperature on soot formation in premixed flames. *Symposium (International) on Combustion* **22**, 403-411, (1989).

108 Figura, L. & Gomez, A. Laminar counterflow steady diffusion flames under high pressure (P ⩽ 3 MPa) conditions. *Combustion and Flame* **159**, 142-150, (2012).

109 Eisner, A. D. & Rosner, D. E. Experimental studies of soot particle thermophoresis in nonisothermal combustion gases using thermocouple response techniques. *Combustion and Flame* **61**, 153-166, (1985).

110 Sgro, L. a. *et al.* Detection of combustion formed nanoparticles. *Chemosphere* **51**, 1079-1090, (2003).

111 Barone, A. C., D'Alessio, A. & D'Anna, A. Morphological characterization of the early process of soot formation by atomic force microscopy. *Combustion and Flame* **132**, 181-187, (2003).

112 Wikipedia. Stokes number. http://en.wikipedia.org/wiki/Stokes_number. January 2014.

113 Koylu, O., McEnally, C. S., Rosner, D. E. & Pfefferle, L. D. Simultaneous Measurements of Soot Volume Fraction and Particle Size / Microstructure in Flames Using a Thermophoretic Sampling Technique. **2180**, 494-507, (1997).

114 Gomez, A. & Rosner, D. E. Thermophoretic Effects on Particles in Counterflow Laminar Diffusion Flames Thermophoretic Effects on Particles in Counterflow Laminar Diffusion Flames. *combustion science and technology* **89**, 335-362, (1993).

115 Amelinckx, S., Van Dyck, D., Van Landuyt, J. & Van Tendeloo, G. *Electron Microscopy: Principles and Fundamentals*. (John Wiley & Sons, Ltd, 1997).

116 YINQE (Yale Institute for Nanoscience and Quantum Engineering) equipment. http://www.yinqe.yale.edu/equipment.htm. November 2013.

117 Goodhew, P. TEM Basics. http://www.matter.org.uk/tem/. February 2014.

118 The Transmission Electron Microscope. http://www.nobelprize.org/educational/physics/microscopes/tem/. February 2014.

119 Eaton, P. & West, P. *Atomic Force Microscopy*. (2010).

120 Gwyddion software. http://gwyddion.net. March 2014.

121 Echavarria, C. a., Sarofim, A. F., Lighty, J. S. & D’Anna, A. Evolution of soot size distribution in premixed ethylene/air and ethylene/benzene/air flames: Experimental and modeling study. *Combustion and Flame* **158**, 98-104, (2011).

122 D’Anna, A., Rolando, A., Allouis, C., Minutolo, P. & D'Alessio, A. Nano-organic carbon and soot particle measurements in a laminar ethylene diffusion flame. *Proceedings of the Combustion Institute* **30**, 1449-1456, (2005).

123 Thomas F. Irvine, Jr. & Hartnett, J. P. *Advances in heat transfer*. Vol. 32 (The Combustion Institute, 1975).

124 Louis Vessot King, B. A. On the convection of heat from small cylinders in a stream of fluid: determination of the convection constants of small platinum wires with applications to hot-wire anemometry. *Philosophical transactions of the royal society of London* **Ser. A 214**, 373-433, (1914).

125 Zhang, D., Wang, Y. & Gan, Y. Characterization of critically cleaned sapphire single-crystal substrates by atomic force microscopy, XPS and contact angle measurements. *Applied Surface Science* **274**, 405-417, (2013).